

INTERIM  
IN-46-CR

THE UNIVERSITY OF ALABAMA IN HUNTSVILLE  
UAH RESEARCH PROPOSAL 94-430

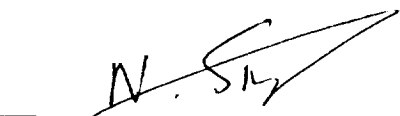
8628

P-96

# STUDIES ON EQUATORIAL SHOCK FORMATION DURING PLASMASPHERIC REFILLING

Third year funding request  
and  
annual report  
for  
**NAGW-2128**

Prepared by

  
\_\_\_\_\_  
N. Singh, Ph.D.

Principal Investigator  
Department of Electrical and Computer Engineering  
The University of Alabama in Huntsville  
Huntsville, AL 35899  
205-895-6678

Submitted by

The University of Alabama in Huntsville

  
\_\_\_\_\_  
Sue B. Weir

Research Administrator

May 1994

(NASA-CR-195864) STUDIES ON  
EQUATORIAL SHOCK FORMATION DURING  
PLASMASPHERIC REFILLING Annual  
Progress Report No. 3, 1993 - 1994  
(Alabama Univ.) 96 p

N94-34669

Unclass

G3/46 0008628



# **Studies on Equatorial Shock Formation During Plasmaspheric Refilling**

Grant # NAGW-2128

P.I.: Dr. N. Singh

## **Brief Summary of Work Performed Since August 1, 1993:**

We have systematically investigated the microprocesses occurring when a magnetic flux tube refills with a cold plasma. The study was performed using simulations based on a small-scale PIC code. The results of this study are summarized in two companion papers which are submitted for publication in the Journal of Geophysical Research [Singh and Leung, 1994a, b]. In Paper 1 [Singh and Leung, 1994a] we have studied the role of ion-beam driven instabilities in filling a magnetic flux tube. Large-scale models of plasmaspheric refilling have revealed that during the early stage of the refilling counterstreaming ion beams are a common feature. However, the instability of such ion beams and its effect on refilling remain unexplored. The difficulty with investigating the effect of ion-beam driven instability on refilling is that the instability and the associated processes are so small-scale that they cannot be resolved in large-scale models; typically the instabilities have scale lengths of a few tens of plasma Debye length, which is a few meters at the most, and the spatial resolution in large-scale models is at least several tens of kilometers. Correspondingly, the temporal scale of the instability is by several orders of magnitude smaller than the temporal resolution afforded by the models. In order to learn the basic effects of ion beam instabilities on refilling, we have performed numerical simulations of the refilling of an artificial magnetic flux tube. The shape and size of the tube are assumed so that the essential features of the refilling problem are kept in the simulation and at the same time the small-scale processes driven by the ion beams are sufficiently resolved. Two types of simulations have been performed; in one type we treat ion kinetically and electrons are assumed to obey the Boltzmann law. In the other type both electrons and ions are treated kinetically. A comparison between the results from such simulations reveal that in the latter type of simulations electron-ion (e-i) and ion-ion (i-i) instabilities occur and significantly modify the evolution of the plasma density distributions in the flux tube along with the total plasma content. When the electron dynamics is simplified by the assumption of the Boltzmann law, both the electron-ion and ion-ion instabilities are inhibited, and only in very late stage of the filling there is a weak scattering of ions due to an enhanced plasma fluctuation level. On the other hand, when electrons are treated kinetically, the e-i instability occurs at an early stage when ion beams are too fast to excite the i-i



instability. The former instability heats the electrons so that conditions for the latter instability are eventually met. The i-i instability and its non-linear evolution creates potential structures including several electrostatic shock pairs which significantly modify the filling process. The electrostatic potential structures are highly dynamic, and at times they appear as moving double layers greatly affecting the state of the plasma inside the central region of the flux tube.

In Paper 2 [Singh and Leung, 1994b] we have studied the effects of equatorially trapped hot plasma on refilling. Equatorially trapped hot plasmas are a common feature of the outer plasmasphere, where flux tube refilling with cold ionospheric plasma occurs after magnetic storms. The role of the hot plasma consisting of hot anisotropic ions and isotropic warm electrons in the refilling process is examined by means of numerical simulations using a one-dimensional particle-in-cell code. Simulations are performed on the filling of an artificial flux tube having a minimum magnetic field at its center. We have performed two types of simulations; in one type, called here Run-A, we allowed cold plasmas to flow into a centrally trapped hot plasma consisting of warm isotropic electrons and hot anisotropic ions with perpendicular temperature  $T_{\perp} > T_{\parallel}$ , the parallel temperature. Run-A reveals a variety of plasma processes relevant to the plasmaspheric refilling affected by the presence of a hot plasma, including formation of propagating electrostatic shocks, intrinsically unstable plasma distribution functions produced by the mixing of hot and cold plasmas, weak downward electric fields supported by an extended potential distribution in the relatively late stage of the evolution of plasma in the flux tube, and an enhanced flux tube filling. In the other type of simulation first a cold plasma flow was allowed to set up in the flow, then a hot plasma consisting of the isotropic electrons and anisotropic ions ( $T_{\perp} > T_{\parallel}$ ) was suddenly injected into the central region of the flux tube. In this case the main distinguishing feature was the formation of relatively stable shocks near the mirror points of the centrally trapped hot plasma. The shocks were found to be standing, unlike in the previous type of simulation. Since the standing shocks form near the effective mirror points of the centrally trapped hot ions, they are called mirror shocks to contrast them from the moving electrostatic shocks seen in Run-A. The stability of the standing shocks was found to increase with the decreasing temperature of the warm electrons injected with the hot plasma. Wherever possible, similarities between the results from the simulations and those from observational data are pointed.

### **Tasks for the Grant Period Beginning August 1, 1994:**

After the investigations based on small-scale simulations reported in Papers 1 and 2, we propose to include the processes seen in these simulations in large-scale hydrodynamic and semikinetic models for the plasmaspheric refilling. We will first attempt to include the effects of



electron-ion instability in terms of electron heating. For this purpose we must develop an algorithm for the electron heating rate as the ion beams evolve during the refilling. After this phase of the work, we will attempt to include the effects of ion-ion instability on the plasma. Since the ion-ion instability leads to the formation of vortices and electrostatic shocks, it is not clear at this time how to include its effect in the large-scale models. We propose to investigate this issue.

One of the interesting results from the small-scale simulations is that the mixing of cold plasma with the equatorially trapped hot plasma produces low energy ring distributions in the perpendicular velocity. Such a distribution function is known to excite the lower hybrid and ion-Bernstein waves. We propose to investigate the stability of the distribution functions seen in the one-dimensional model by performing 2-dimensional PIC simulations, which will allow us to study transverse heating of the cold ions. Our main goal here will be to critically examine the conditions under which the ion heating produces the trapped ion population merged with a cold core as observed from DE-1 [Olsen et al, 1987].

### **Recent Publications Under Grant # NAGW-2128**

1. Singh, N., G. R. Wilson, and J. L. Horwitz, Comparison of hydrodynamic and semikineti models for plasma flow along closed field lines, *J. Geophys. Res.*, June (in press), 1994.
2. Singh, N., Interaction of field-aligned cold plasma flows with an equatorially-trapped hot plasma: Electrostatic shock formation, *Geophys. Res. Lett.*, 20, 799, 1993.
3. Singh, N., and L. C. Leung, Numerical simulation of filling a magnetic flux tube with a cold plasma: (1) Role of ion beam-driven instabilities, *J. Geophys. Res.*, submitted, 1994.
4. Singh, N., and L. C. Leung, Numerical simulation of filling a magnetic flux tube with a cold plasma: (2) Effects of magnetically trapped plasma, *J. Geophys. Res.*, submitted, 1994.
5. Leung, L. C., and N. Singh, Standing mirror shocks in the equatorial plasmasphere (Abstract), *EOS*, 74, 504, 1993.
6. Nadar, P., and N. Singh, Effects of equatorially trapped hot plasma on flux tube refilling (Abstract), *EOS*, 74, 510, 1993.





THE UNIVERSITY OF ALABAMA IN HUNTSVILLE  
 UAH RESEARCH PROPOSAL 94-430  
 COST ESTIMATE FOR A ONE-YEAR PERIOD  
 (August 1, 1994 - July 31, 1995)

Third year funding for NAGW-2128

		FY'94	FY'95	
		8/1/94-9/30/94	10/1/94-7/31/95	TOTAL
<b>A. SALARIES AND WAGES</b>				
1. Dr. N. Singh, Principal Investigator *				
25% x 3 weeks x \$1,589.74/wk.		1,192		
25% x 6 weeks x \$1,675.68/wk.		2,514		
25% x 31 weeks x \$1,742.70/wk.			13,506	
25% x 11 weeks x \$1,742.70/wk.			4,792	22,004
2. Secretary				
5% x 3/12 yr. x \$18,889		236		
5% x 9/12 yr. x \$19,645			737	973
3. Undergraduate Research Assistant				
15 hr. wk. @ \$5.20/hr.		1,014	2,964	3,978
<b>TOTAL SALARIES AND WAGES</b>		<b>4,956</b>	<b>21,999</b>	<b>26,955</b>
<b>B. FRINGE BENEFITS (21% A.1. &amp; A.2.)</b>		<b>828</b>	<b>3,997</b>	<b>4,825</b>
<b>C. OPERATING COSTS</b>				
1. Supplies, reproduction		125	320	445
2. Page charges		0	1,600	1,600
<b>TOTAL OPERATING COSTS</b>		<b>125</b>	<b>1,920</b>	<b>2,045</b>
<b>D. TRAVEL</b>				
1. See below		0	1,280	1,280
<b>TOTAL DIRECT COST</b>		<b>5,909</b>	<b>29,196</b>	<b>35,105</b>
<b>E. INDIRECT</b>				
1. 42.0% MTDC		2,482	0	2,482
2. 42.5% MTDC		0	12,408	12,408
<b>TOTAL INDIRECT</b>		<b>2,482</b>	<b>12,408</b>	<b>14,890</b>
<b>TOTAL ESTIMATED COST</b>		<b>8,390</b>	<b>41,605</b>	<b>\$49,995</b>

\* UAH changes from a quarter to semester academic year beginning 8/19/94. This change affects the way an academic appointment's time is computed. UAH's annual merit increase occurs on October 1. The four components of Dr. Singh's salary listed above are:

3 weeks of summer 1994 (7/1/94-8/18/94) figured on the weekly rate of an FY'94 academic year (39 weeks) base of \$62,000 (\$62,000/39)

6 weeks of academic year 1995 (8/19/94-9/30/95) figured on the weekly rate of the new semester academic year (37 weeks) from the \$62,000 base. (\$62,000/37)

31 weeks of the remainder of the 1995 academic year figured on the new base of \$64,480 (4% increase) (\$64,480/37)

11 weeks of summer 1995 (May 15-June 30) at same weekly rate as academic year 1995

D.1. Travel to professional meeting to present paper/Washington, DC used for estimation purposes = \$1,280  
 air fare = \$623 (travel agent quote), per diem = \$144 x 3 days (GSA rate), registration = \$125, misc. = \$50

/1/ See paragraph 2.a. of financial data sheet

/2/ See paragraph 2.b. of financial data sheet

/3/ See paragraph 2.c. of financial data sheet

/4/ See paragraph 2.d. of financial data sheet



## FINANCIAL DATA SHEET

### 1. Price Summary

The cost estimate presents applicable pricing information in the standard format adopted by the University.

### 2. Cost Substantiation

#### a. Salaries:

Proposed salaries are quoted as actuals and are increased by 4.0 percent each fiscal year to cover anticipated raises. These increases are MERIT, not cost-of-living, raises. Percentage of time is estimated. Salaries are verifiable through the established payroll system and after-the-fact certification of effort.

#### b. Fringe benefits:

Paid absences such as vacation, sick leave, and holidays are included in salaries and are charged as a direct expense as negotiated in the indirect rate.

Fringe benefits are charged as a direct expense. They include State Teachers' Retirement, Teachers' Insurance and Annuity Association--The College Retirement Equities Fund, social security, disability insurance, and life insurance where applicable. Graduate Research Assistants receive tuition assistance as a fringe benefit in lieu of salary.

#### c. Travel:

Reimbursement of travel will be in accordance with The University of Alabama travel regulations. Expenses for out-of-state travel will be paid on the basis of actual, reasonable, and necessary expenses. Expenses for in-state travel will be paid on a per diem basis. Transportation costs will be reimbursed on the basis of actual costs for common carrier and at the approved rate per mile for automobiles.

#### d. Indirect Rate:

The University negotiates its pre-determined indirect rate with the Department of Health and Human Services. The provisional (in negotiation) indirect rates are as follows:

	FY'94	FY'95	FY'96	FY'97		FY'94	FY'95	FY'96	FY'97
On-campus Research	42.0%	42.5%	43.0%	43.0%	Off-campus Research	26.0%	26.0%	26.0%	26.0%
On-campus Instruction	62.6%				Off-campus Instruc.	25.9%			
On-campus Public Service	39.4%				Off-campus Pub. Ser.	26.0%			

These rates are based on Modified Total Direct Costs (MTDC). Indirect is not charged on capital expenditures such as equipment, alterations, and renovations. Only the first \$25,000 of each subcontract is subject to indirect rates and participant support costs to not incur indirect.

#### e. Approved Procurement System:

The UAH procurement system has been approved by the Department of the Navy, Office of Naval Research, through September 30, 1994.

### 3. Government Agency Contacts:

Administrative Contracting Officer :  
Office of Naval Research Resident Representative  
Atlanta Area Office  
101 Marietta Tower  
Suite 2805  
Atlanta, GA 30303  
ATTN: Charles K. Hayes (NASA awards)  
404-730-9255  
ATTN: Kathy L. Raible (All other awards)  
407-730-9262

Audit Functions:  
DHHS/OIG  
Office of Audit  
Federal Building  
P.O. Box 1704  
Atlanta, GA 30301  
ATTN: Michael D. Geiger, Audit Mgr.  
404-331-2446

### 4. Awards:

Resulting contracts or grants should be forwarded to:

Research Administration  
The University of Alabama in Huntsville  
Research Institute/Room E-39  
Huntsville, AL 35899  
205-895-6000; 205-895-6677 (fax)



**CERTIFICATION REGARDING DRUG-FREE REQUIREMENTS**  
**(Grants/Cooperative Agreements)**

A. The grantee certifies that it will provide a drug-free workplace by:

1. Publishing a statement notifying employees that the unlawful manufacture, distribution, dispensing, possession or use of a controlled substance is prohibited in the grantee's workplace and specifying the actions that will be taken against employees for violations of such prohibition:

2. Establishing a drug-free awareness program to inform employees about:

- (a.) The dangers of drug abuse in the workplace;
- (b.) The grantee's policy of maintaining a drug-free workplace;
- (c.) Any available drug counseling, rehabilitation, and employee assistance programs;
- (d.) The penalties that may be imposed upon employees for drug abuse violations occurring in the workplace.

3. Making it a requirement that each employee to be engaged in the performance of the grant be given a copy of the statement required by paragraph 1.

4. Notifying the employee in the statement required by paragraph 1 that, as a condition of employment under the grant, the employee will:

- (a.) Abide by the terms of the statement, and
- (b.) Notify the employer of any criminal drug statute conviction for a violation occurring in the workplace no later than five days after such conviction.

5. Notifying the agency within ten days after receiving notice under subparagraph 4(b), with respect to any employee who is so convicted.

6. Taking one of the following actions, within 30 days of receiving notice under subparagraph 4(b), with respect to any employee who is so convicted:

- (a.) Taking appropriate personnel action against such an employee, up to and including termination, or
- (b.) Requiring such employee to participate satisfactorily in a drug abuse or rehabilitation program approved for such purposes by a Federal, State or local health, law enforcement, or other appropriate agency.

7. Making a good faith effort to continue to maintain a drug-free workplace through implementation of paragraphs 1, 2, 3, 4, 5, and 6.

B. The grantee shall insert in the space provided below the site(s) for the performance of the work done in connection with specific grant:

Place of Performance: The University of Alabama in Huntsville, Huntsville, Madison Co., AL

Responsible University Official: Sue B. Weir 5-4-94  
Sue B. Weir, Research Administrator Date

Title/Identification of Applicable Research Proposal: UAH Proposal 94-430



**CERTIFICATION REGARDING DEBARMENT, SUSPENSION, AND  
OTHER RESPONSIBILITY MATTERS --  
PRIMARY COVERED TRANSACTIONS**

(1.) The prospective primary participant certifies that, to the best of its knowledge and belief, it and its principals:

(a.) Are not presently debarred, suspended, proposed for debarment, declared ineligible, or voluntarily excluded from covered transactions by any Federal department or agency.

(b.) Have not within a three-year period preceding this proposal been convicted or had a civil judgment rendered against them for commission of fraud performing a public (Federal, State or local) transaction or contract under a public transaction; violation, theft, forgery, bribery, falsification or destruction of records, making false statements, or receiving stolen property.

(c.) Are not presently indicted or otherwise criminally or civilly charged by a government entity (Federal, State, or local) with commission of any of the offenses enumerated in paragraph (1.) (b.) of this certification; and

(d.) Have not within a three-year period preceding this application/proposal had one or more public transactions (Federal, State, or local) terminated for cause or default.

(2.) Where the prospective primary participant is unable to certify to any of the statements in this certification, such prospective participant shall attach an explanation to this proposal

Proposal identification: 94-430

Signature: Sue B. Weir Date: 5-4-94

Name & Title: Sue B. Weir, Research Administrator

Institution: The University of Alabama in Huntsville





**CERTIFICATION REGARDING LOBBYING  
CONTRACTS, GRANTS, LOANS & COOPERATIVE  
AGREEMENTS**

The undersigned certifies, to the best of his/her knowledge, that:

1. No Federal appropriated funds have been paid or will be paid, by or on behalf of the undersigned, to any person for influencing or attempting to influence an officer or employee of any agency, a Member of Congress, an officer or employee of Congress, or an employee of a Member of Congress in connection with the awarding of any Federal contract, the making of any Federal grant, the making of any Federal loan, the entering into of any cooperative agreement, and the extension, continuation, renewal, amendment, or modification on any Federal contract, grant, loan or cooperative agreement.

2. If any funds other than Federal appropriated funds have been paid or will be paid to any person for influencing or attempting to influence an officer or employee of any agency, a Member of Congress, an officer or employee of Congress, or any employee of a Member of Congress in connection with this Federal contract, grant, loan or cooperative agreement, the undersigned shall complete and submit Standard Form-LLL, "Disclosure Form to Report Lobbying," in accordance with its instructions.

3. The undersigned shall require that the language of this certification be included in the award documents for all subawards at all tiers (including subcontracts, subgrants, and contracts under grants, loans, and cooperative agreements) and that all subrecipients shall certify and disclose accordingly.

This certification is a material representation of fact upon which reliance was placed when this transaction was made or entered into. Submission of this certification is prerequisite for making or entering into imposed by Section 1352, title 31 US. Code Any person who fails to file the required certification shall be subject to a civil penalty of not less than \$10,000 and not more than \$100,000 for each such failure.

The University of Alabama in Huntsville  
Organization Name

UAH Proposal 94-430  
Award Number

Sue B. Weir, Research Administrator  
Name and Title of Authorized Person

Sue B. Weir                      5-4-94  
Signature                                      Date



INTERACTION OF FIELD-ALIGNED COLD PLASMA FLOWS WITH AN EQUATORIALLY-TRAPPED HOT PLASMA: ELECTROSTATIC SHOCK FORMATION

Nagendra Singh

Department of Electrical and Computer Engineering, University of Alabama in Huntsville

93A 38084

**Abstract.** Effects of equatorially trapped hot plasma on the highly supersonic cold-plasma flow occurring during early stage plasmaspheric refilling are studied by means of numerical simulations. It is shown that the equatorially trapped hot ions set up a potential barrier for the cold ion beams and facilitate formation of electrostatic shocks by reflecting them from the equatorial region. Simulations with and without the hot plasma show different flow properties; the formation of electrostatic shocks occur only in the former case. The simulation with the hot plasma also reveals that the magnetic trapping in conjunction with the evolution of the electrostatic potential barrier produces ion velocity distribution functions consisting of a cold core and a hot ring in the perpendicular velocity. Such a distribution function provides a source of free energy for equatorial waves. The corresponding electron population is warm and field aligned.

# Introduction

So far most theoretical studies on plasmaspheric refilling have been primarily concerned with the outflow of cold ionospheric plasma and its trapping in the flux tube. In such theoretical studies an important observational fact, which has been ignored, is that the flux tubes undergoing refilling contain a hot plasma population trapped in the equatorial region. Such plasmas originate from the ring current or the plasma sheet and are characterized by  $T_{\perp}^H > T_{\parallel}^H$ , where  $T_{\perp}^H$  and  $T_{\parallel}^H$  are the perpendicular and parallel temperatures of the hot ions, respectively. Specific observations of such hot ions having relatively large pitch angle anisotropies ( $A_i = T_{\perp}^H/T_{\parallel}^H > 2$ ) come from GEOS-1 and -2, which observed the hot ions in the energy range  $> 10$  keV in the noon sector. Such hot ions are known to excite electromagnetic ion cyclotron waves [Roux et al., 1982].

Another set of observations, where the role of hot plasma has been invoked, deals with thermal ions transversely heated to energies up to a few hundred eV and trapped in the equatorial region [Olsen et al., 1987]. Here again hot ions are suggested to be the source of free energy for exciting the broadband waves observed from DE-1. Theories suggest that the broadband waves are driven by a combined effect of temperature anisotropy and ring type of distributions of energetic protons [Perraut et al., 1982]. The effect of heating of the thermal ions on re-

filling has been studied [Singh and Chan, 1992], but the direct effect of the hot ions on the refilling has not been studied so far.

The purpose of this letter is to show that the hot anisotropic ions, which are commonly present in the equatorial region of flux tubes undergoing refilling and drive the equatorial processes discussed above [Olsen et al., 1987; Roux et al., 1982], facilitate the process of electrostatic shock formation since they provide an effective potential barrier for the upflowing ion beams of cold ionospheric plasma. The shock formation occurs even for highly supersonic ion beams which are expected to occur during early stage refilling [Banks et al., 1971; Singh et al., 1986; Rasmussen and Schunk, 1988; Singh, 1990; Wilson et al., 1992]. If the hot plasma consists of isotropic electrons and anisotropic bi-Maxwellian ions with anisotropy  $A_i = T_{\perp}^H/T_{\parallel}^H > 1$ , the potential difference between the equator, where the minimum magnetic field strength is  $B_m$ , and an ionospheric point where the magnetic field is  $B$ , is given by  $\Phi = kT_{\parallel}^H/e[1 + T_{\parallel}^H/T_e]^{-1} \ln(\Gamma)$ , where  $\Gamma = A_i(1 - B_m/B) + B_m/B$  [Whipple, 1977].

Since  $B_m/B \ll 1$ , the equatorial potential with respect to the ionosphere for  $T_e \ll T_{\parallel}^H$  is  $\Phi \simeq (kT_e/e) \ln(A_i)$ . For  $A_i = 2$  and  $kT_e/e = 10$  V, the typical values for these parameters used in wave analysis [Roux et al., 1982],  $\Phi \simeq 7$  V. However, this potential difference is true when no ionospheric cold plasma is present; in the presence of a cold plasma, it is not certain how large the potential difference is and how it is distributed along the field line. In the following discussion, we present results from numerical simulations elucidating the interactions between cold and hot plasmas when the former plasma flows into the latter one trapped in a magnetic mirror. The simulation presented here is small scale, in contrast to the large-scale problem in space. Therefore, the results presented here only serve the purpose of elucidating the processes involved in hot-cold plasma interactions.

# Numerical Model

We perform a one-dimensional particle-in-cell simulation of plasma flow along an artificial flux tube (Figure 1a). The magnetic field  $B(X) = B_0(1 - \alpha \exp[-(X - d/2)^2/\sigma^2])$  where  $B_0$  is a constant field outside the minimum-field region,  $d$  is the size of the simulation system and the choice of  $\alpha$  and  $\sigma$  determines the desired field distribution. The hot plasma is created by injecting a large number of electrons and ions in the minimum-B field region. Such plasma particles are chosen from Maxwellian or bi-Maxwellian velocity distributions depending upon the requirement of a simulation run. The cold plasma flows into the flux tube from the two plasma reservoirs at

Copyright 1993 by the American Geophysical Union.

Paper number 93GL00492  
0094-8534/93/93GL-00492\$03.00

the ends of the simulation system at  $X = 0$  and  $X = d$  (Figure 1a). The simulation technique is described in Singh and Chan [1992]. We solve for the motions of charged particles in self-consistent electric fields, determined by solving Poisson's equation. As the particles move in the flux tube, their magnetic moments are assumed to be conserved.

In the cold-plasma reservoirs electron and ion temperatures are  $T_0$ . The reservoirs supply a continuous flux of charged particles into the flux tube through the process of plasma expansion. In the simulations reported here, we have used  $m_i/m_e = 400$ , which adequately separates the electron and ion time scales and, at the same time, allows computationally feasible runs. The hot plasma is injected into the central region of the simulation system at time  $t=0$  (Figure 1a). The properties of the hot plasma are described later. Numerical parameters of the simulations are as follows: system size  $d = 5 \times 10^3 \lambda_d$ ,  $B$  field parameters  $\alpha = 0.9$ ,  $\sigma = 750 \lambda_d$ , cell size  $\Delta x = 20 \lambda_d$ , and time step  $\Delta t = 0.1 \omega_{pe0}^{-1}$ , where  $\lambda_d$  and  $\omega_{pe0}$  are the Debye length and electron-plasma frequency in the cold plasma reservoirs. In the following discussion we have used normalized quantities defined as follows: time  $\bar{t} = t \omega_{pi0}$ , distance  $\bar{X} = X/\lambda_d$ , velocity  $\bar{V} = V/V_{te}$  and electric potential  $\bar{\Phi} = e\Phi/kT_0$ , where  $V_{te} = (kT_0/m_e)^{1/2}$  and  $\omega_{pi0} = (m_e/m_i)^{1/2} \omega_{pe0}$ .

### Numerical Results

First we present results from a simulation in which "equatorial" hot plasma is not included. This simulation serves as a reference against which the hot plasma effects on the cold plasma flow are compared. Figures 1b to 1f show the temporal evolution of the flow of cold ions into the flux tube from the reservoirs shown in Figure 1a. These panels show the phase-space plots in the  $X - V_{||}$  plane. Each dot in the figure represents an ion, giving its parallel velocity and position. The simulation begins at  $t = 0$ , when plasmas from the reservoirs begin to flow

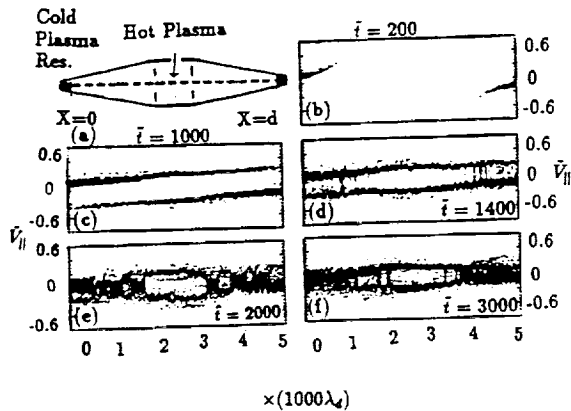


Fig. 1. (a) Artificial flux tube in which plasma expands from the cold plasma reservoirs at  $X=0$  and  $X=d$ . The hot plasma is injected in the central region. (b) to (f) ion phase-space plots in  $X - V_{||}$  plane at selected times as shown. The plots show evolution of the cold plasma flow in absence of a hot plasma.

in the flux tube. The corresponding flow of electrons is not shown here. Figure 1b shows expanding ion beams into the simulation region at  $\bar{t} = 200$ . The plot for  $\bar{t} = 1,000$  (Figure 1c) shows that the ion beams have expanded from one end to the other end of the simulation region, setting up counterstreaming. Equatorial shock formation has not occurred. At this time, ion beams are too fast to couple through the ion-ion instability; the relative flow velocity between the beams is  $V_{rel} = 0.4V_{te} \approx 8c_s$ , where  $c_s$  is the local ion-acoustic speed at the equator,  $X = d/2$ , and is about  $0.05V_{te}$ . However, at later times the beams become progressively slower as the plasma accumulates in the flux tube, and when they become sufficiently slow in the regions near the ends of the flux tube they excite ion-ion instability as seen for  $\bar{t} \geq 1,400$  (Figures 1d to 1f); the instability creates vortex-like structures in the phase space.

The instability is seen to thermalize the ion beams (Figure 1e). However, in the middle of the simulation region, where the magnetic field is minimum, counterstreaming of ion beams is seen to persist.

Simulation with a hot plasma in the region of minimum magnetic field reveals a quite different behavior of the flow. We performed several simulations by varying the temperatures of the hot plasma but kept ion anisotropy  $A_i > 1$  and electron anisotropy  $A_e = 1$  and  $T_e \ll T_{i||}^H$ . Such properties of hot plasma have been measured [Rouz et al., 1982]. Relative densities of the cold ( $n_C$ ) and hot ( $n_H$ ) ions in their respective source regions were also varied. The results from such a parametric study will be reported elsewhere. We present results here for  $T_{i||}^H = T_{i\perp}^H/2 = 900T_0$ ,  $T_e = 10T_0$ , and  $n_C \approx 100 n_H$ .

The hot plasma is injected in the central region  $2300 \leq x/\lambda_d < 2700$  at  $t = 0$ , when cold plasma flows begin from the reservoirs. Figure 2 shows the evolution of the cold plasma flow along with the potential and density profiles in the flux tube. The panels a to d show the ion phase space plot in  $X - V_{||}$  plane. The phase-space plot of ions in  $X - V_{\perp}$  plane is shown in panels e to h. The evolution of the potential profiles in the flux tube is shown in panels i to l, and the corresponding plasma density is shown in panels m to p. The evolution of the electron phase-space ( $X - V_{||}$ ) is shown in panels q to t. As shown on the top of the figure, the columns from left to right show the properties of the flow at  $\bar{t} = 100, 500, 700$ , and  $1000$ , respectively. At an early time ( $\bar{t} = 100$ ), the flow can be characterized by the following features: (1) expanding cold ion beams (panel a), (2) equatorially trapped ions originating from the hot plasma (panel e), (3) a potential maximum at the mid-point of the simulation region (panel i), and (4) a density maximum coinciding with the potential maximum (panel m). The density maximum at this time entirely represents the trapped hot ions, and there is no contribution from the cold plasma flow.

At  $\bar{t} = 500$ , the cold plasma flow comes into contact with the hot plasma; the cold ion beams have somewhat penetrated into the region of the hot plasma (panels b and f). Already the cold beams show the sign of retardation by the potential barrier. The slowing down of the ion beams enhances the potential barrier further; panel j shows that at  $\bar{t} = 500$  the equatorial potential maximum has grown to  $15kT_0/e$ , in contrast to  $3kT_0/e$  at  $\bar{t} = 100$ .

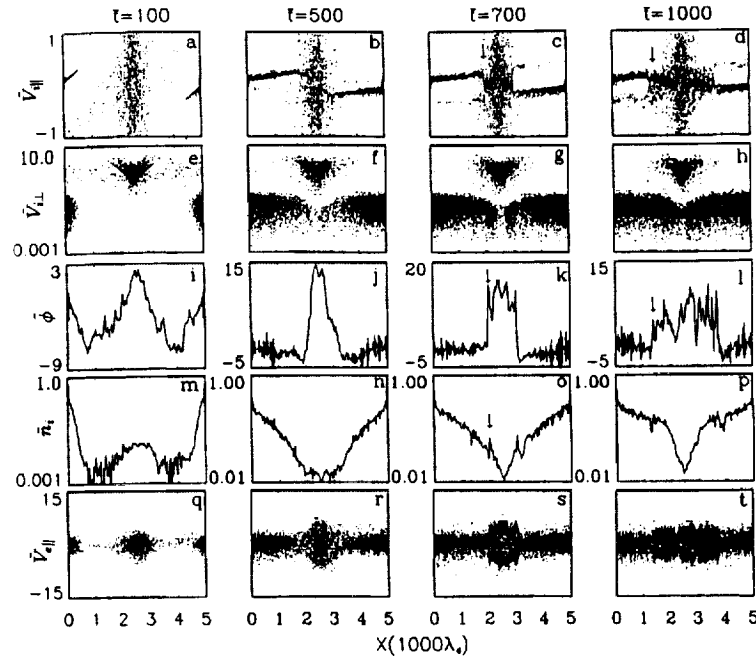


Fig. 2. Evolution of the cold plasma flow in the presence of equatorially trapped hot ions. Each column shows the state of the plasma at times shown at the top. (a) to (d)  $X - V_{\parallel}$  phase-space plots for ions, (e) to (h)  $X - V_{\perp}$  phase space plots for ion, (i) to (l) Potential distributions, (m) to (p) Ion density distributions, and (q) to (t) Electron phase-space plots in  $X - V_{\parallel}$  plane.

Note the change in the vertical scale between panels i and j. The filling of the flux-tube with the cold plasma changes the density profile by creating a density minimum at the equator (panel n).

The plots at  $\bar{t} = 700$  show that the contact between the hot and cold plasma has evolved into a pair of electrostatic shocks, one on each side of the hot ions trapped in the minimum-B field region. The shocks are indicated by arrows where flow velocities of the cold ion beams suddenly decrease (panel c). Near the shocks, the potential profile shows sharp jumps (panel k) and the density profile shows spikes (panel o).

The shocks propagate away from the “equatorially” trapped hot plasma towards the end of the flux tube, thermalizing the cold plasma just behind the shocks. The

propagation of shocks can be seen by comparing the panels in columns for  $\bar{t} = 700$  and 1000. The shocks propagate with a speed  $V_{sh} \approx 0.09V_{te} \approx C_{so}$ , where  $C_{so}$  is the ion-acoustic speed in the cold plasma reservoirs. As the shocks propagate away from the hot plasma, the thermalized cold plasma behind the shocks punches through the region of hot plasma where the potential barrier existed earlier. This penetration of the cold plasma is clearly seen from the  $X - V_{\perp}$  plots shown in Figure 2e to 2h. As the cold ions penetrate into the minimum-B field region, where hot ions are trapped, they cool adiabatically as clearly seen from these plots. The penetration of cold plasma is accompanied with a reduction in the potential barrier, caused by the cold electrons being accelerated into the high potential region (panels r and s); these electrons tend to neutralize the effect of the hot ions stably trapped in the minimum-B field region.

A noteworthy feature of the plasma after the spatial mixing of hot and cold plasmas is the nature of the resulting ion distribution functions in the equatorial region, as shown in Figures 3a and 3b. The parallel velocity distribution (Figure 3a) shows a core of cold ions superimposed on a warm ion population. The perpendicular velocity distribution function (Figure 3b) also shows the cold ions, but the hot ions appear as a beam. Since the ions in the beam are nearly uniformly distributed in their phase, the beam is actually a ring in the perpendicular velocity space. The ring distribution function is the result of the trapping of the hot ions in the magnetic mirror in combination with the evolution of the electrostatic potential distribution. Some of the ions from the hot population having relatively small perpendicular velocities are lost from the mirror due to the parallel electric fields. In the absence of the electrostatic potential, one expects a

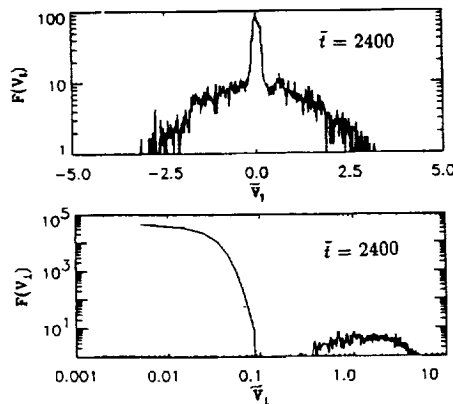


Fig. 3. Ion velocity distribution functions in the equatorial region (a) Parallel velocity distribution, (b) Perpendicular velocity distribution.

loss-cone distribution. The loss of ions with relatively low  $V_{\perp}$ , yields the ring distribution. The cold core originates from the cold ions penetrating in the minimum-B field region. The importance of these findings lies in the fact that ring types of distribution functions along with a core of cold ions can be a source of free energy for exciting equatorial waves [Lee and Birdsall, 1979], which can heat the latter ions. We point out that the low energy end of the ring distribution found here occurs at an energy of a few tens of eV, unlike the relatively energetic ring distribution with energy  $> 5$  keV observed from GEOS [Perraut et al., 1982].

### Conclusion and Discussion

The main conclusions of the study in this paper are the following: (1) The presence of the hot anisotropic ions trapped in the equatorial region can drastically affect the flow of the cold plasma. (2) The potential barrier associated with such a hot ion population facilitates formation of electrostatic shocks even when the cold ion beams coming from the ionosphere are highly supersonic. (3) The eventual mixing of the hot and cold plasmas produces a potentially unstable velocity distribution function for the ions. They develop a ring distribution in the perpendicular velocity. The ring distribution with  $\partial f(V_{\perp})/\partial V_{\perp}$  begins at a relatively low energy corresponding to the energy of an ion falling down the potential barrier of the order of 10 V. The ring distribution discussed here is different from the observed high energy rings ( $> 5$  keV) produced by hot plasma injection and its subsequent convection [Perraut et al., 1982].

Recent satellite observations have shown that equatorially trapped warm ions are generated by equatorial perpendicular heating of the thermal ions; the heating is caused by waves generated by an energetic hot ion population, having the temperature anisotropy  $T_{i\perp}^H > T_{i\parallel}^H$  and/or ring type of velocity distribution [Olsen et al., 1987; Perraut et al., 1982]. Olsen et al. [1987] also report the reflection of cold ion beams. However, it is believed that the reflection is caused by the potential barrier set up by the thermal ions which have undergone the transverse heating. From our simulations, it appears that the hot ion population, which drives the waves by virtue of its anisotropy or ring, may reflect the fast ion beams at an earlier stage before the waves grow and consequent ion heating produces a warm anisotropic ion population.

Furthermore, before thermal ions are heated they must enter the hot plasma region. This entry is retarded by the potential barrier set up by the hot ions. Even if the hot plasma injection occurs at a stage when field-aligned flows have set up at the equator, the potential barrier is likely to expel the cold plasma from the equatorial region. The presence of thermal ions is essential in the wave generation processes. Therefore, it is suggested that the reflection of ion beams observed from DE-1 may not be necessarily caused by the equatorial perpendicular heating of thermal ions; it appears that the reflection of ion beams and heating of thermal ions are all driven by the hot ions, but

heating should phenomenologically follow the reflection of upflowing ion beams.

**Acknowledgments.** This work was supported by NASA grant NAGW-2128 to the University of Alabama in Huntsville.

### References

- Banks, P. M., A. F. Nagy, and W. I. Axford, Dynamical behavior of thermal protons in the mid-latitude ionosphere and magnetosphere, *Planet. Space Sci.*, **19**, 1053, 1971.
- Lee, J. K. and C. K. Birdsall, Velocity space ring-plasma instability, magnetized, Part 1: Theory, *Phys. Fluids*, **22**, 1306, 1979.
- Olsen, R. C., C. R. Chappell, D. L. Gallagher, J. L. Green, C. R. Chappell, and R. R. Anderson, Plasma observations at the magnetic equator, *J. Geophys. Res.*, **92**, 2385, 1987.
- Perraut, S., A. Roux, P. Robert, and R. Gendrin, A systematic study of VLF wave above  $F_H^+$  from GEOS-1 and -2 measurements and near relationship with proton ring distributions, *J. Geophys. Res.*, **87**, 6219, 1982.
- Rasmussen, C. E., and R. W. Schunk, Multistream hydrodynamic modeling of interhemispheric plasma flow, *J. Geophys. Res.*, **93**, 14, 557, 1988.
- Roux, A., S. Perraut, J. L. Ranch, C. D. Villedary, C. Kremser, A. Rorths and D. T. Young, Wave particle interactions near  $\Omega He^+$  observed on board GEOS-1 and -2, 2. Generation of ion cyclotron waves and heating of  $He^+$  ions, *J. Geophys. Res.*, **87**, 8174, 1982.
- Singh, N., Comment on "Multistream hydrodynamic modelling of interhemispheric plasma flow", by C. E. Rasmussen and R. W. Schunk, *J. Geophys. Res.*, **95**, 17, 272, 1990.
- Singh, N. and C. B. Chan, Effects of equatorially trapped ions on refilling of the outer plasmasphere, *J. Geophys. Res.*, **97**, 1167, 1992.
- Singh, N., R. W. Schunk and H. Thiemann, Temporal features of the refilling of a plasmaspheric flux tube, *J. Geophys. Res.*, **91**, 1986.
- Whipple, E. C., The signature of parallel electric fields in a collisionless plasma, *J. Geophys. Res.*, **82**, 1525, 1977.
- Wilson, G. R., J. Lin, and J. L. Horwitz, A semi-kinetic model for early stage plasmasphere refilling, 1: Effects of coulomb collisions, *J. Geophys. Res.*, **97**, 1189, 1992.

N. Singh, Department of Electrical and Computer Engineering, University of Alabama in Huntsville, AL 35899.

(Received November 16, 1992;  
accepted January 25, 1993.)

# Comparison of hydrodynamic and semikinetic treatments for a plasma flow along closed field lines

Nagendra Singh

Department of Electrical and Computer Engineering and Center for the Study of Plasma and Aeronomic Research,  
University of Alabama, Huntsville

G. R. Wilson and J. L. Horwitz

Department of Physics and Center for the Study of Plasma and Aeronomic Research, University of Alabama,  
Huntsville

**Abstract.** Hydrodynamic and semikinetic treatments of plasma flow along closed geomagnetic field lines are compared. The hydrodynamic treatment is based on a simplified 16-moment set of transport equations as the equations for the heat flows are not solved; the heat flows are treated heuristically. The semikinetic treatment is based on a particle code. The comparison deals with the distributions of the plasma density, flow velocity, and parallel and perpendicular temperatures as obtained from the two treatments during the various stages of the flow subject to certain assumed boundary conditions. In the kinetic treatment, the appropriate boundary condition is the prescription of the velocity distribution functions for the particles entering the flux tubes at the ionospheric boundaries; those particles leaving the system are determined by the processes occurring in the flux tube. The prescribed distributions are half-Maxwellian with temperature  $T_o$  and density  $n_o$ . In the hydrodynamic model, the prescribed boundary conditions are placed on density ( $n_o$ ), flow velocity ( $V_o$ ), and temperature ( $T_o$ ). We found that results from the hydrodynamic treatment critically depend on  $V_o$ ; for early stages of the flow this treatment yields results in good agreement with those from the kinetic treatment, when  $V_o = (kT_o / 2\pi m)^{1/2}$ , which is the average velocity of particles moving in a given direction for a Maxwellian distribution. During this early stage, the flows developing from the conjugate ionospheres show some distinct transitions. For the first hour or so, the flows are highly supersonic and penetrate deep into the opposite hemispheres, and both hydrodynamics and kinetic treatments yield almost similar features. It is found that during this period heat flow effects are negligibly small. When a flow penetrates deep into the opposite hemisphere, the kinetic treatment predicts reflection and setting up of counterstreaming. In contrast, the hydrodynamic treatment yields a shock in the flow. The reasons for this difference in the two treatments is discussed, showing that in view of the relatively warm ions, the coupling of ion beams and the consequent shock formation in the off-equatorial region are not likely due to the enhancements in the beam temperatures. The counterstreaming in the kinetic treatment and the shock in the hydrodynamic treatment first advance upward to the equator and then downward to the ionospheric boundary from where the flow originated. The transit time for this advancement is found to be about 1 hour for the perspective models. After 2 hours or so, both models predict that the flows from the ionospheric boundaries are generally subsonic with respect to the local ion-sound speed. At late stages of the flow, when a substantial fraction of ions entering the flux tube begin to return back in the kinetic treatment, the hydrodynamic treatment with the boundary condition  $V_o = (kT_o / 2\pi m)^{1/2}$  yields an overrefilling, and the choice of  $V_o$  becomes uncertain.

## 1. Introduction

In connection with the problem of plasmaspheric refilling, in recent years several models for plasma flow along closed magnetic field lines have been developed [Khazanov *et al.*, 1984; Singh *et al.*, 1986; Singh *et al.*, 1988; Rasmussen and

Schunk, 1988; Singh *et al.*, 1991; Guiter and Gombosi, 1990; Wilson *et al.*, 1992]. These models differ in complexity in terms of describing the plasma and in including the ionosphere as a source of plasma for the refilling. In terms of describing the plasma and the most contrasting feature of the existing models deals with the hydrodynamic and kinetic treatments for the flows, based on plasma fluid equations and a particle-in-cell code, respectively. For the purpose of including the ionosphere as a source of plasma for the refilling, in most studies the topside ionosphere is replaced by a set of boundary conditions on the plasma flow, except by Guiter and Gombosi [1990], who have included the generation and loss of plasma through chemical reactions in a hydrodynamic model. In this paper, we are mainly concerned with the treatments of the plasma with simple sets of boundary conditions on the plasma flow; we compare the properties of the plasma along closed field lines as given by hydrodynamic [Singh *et al.*, 1992] and semikinetic [Wilson *et al.*, 1992] treatments.

The success of a hydrodynamic treatment depends on the problem being solved and on the ingenuity of the user in choosing the hierarchy of moment equations on which fluid equations are based. In recent years, researchers in space physics have used fluid descriptions based on 13-moment [Schunk, 1977; Mitchell and Palmadesso, 1983], and 16-moment [Barakat and Schunk, 1982; Ganguli and Palmadesso, 1987; Gombosi and Rasmussen, 1991; Korosmerzey *et al.*, 1992, 1993] set of transport equations. In developing the moment equations, the ingenuity lies in a series expansion of the plasma distribution function using a biMaxwellian distribution function as a base. Therefore hydrodynamic treatment based on moment equations are good as long as the distribution function is close to a biMaxwellian. When the distribution function severely departs from a biMaxwellian and involves multistreaming of plasma particles, the moment equations are seriously handicapped, despite the sophistication of the higher-order moment equations used.

As mentioned above, recent models for plasmaspheric refilling are based on both a kinetic treatment using particle-in-cell (PIC) code and a hydrodynamic treatment with varying degrees of sophistication in choosing the hierarchy of the moment equations. In some early models, only continuity and momentum equations were solved for the ions, and the electrons were assumed to remain isothermal [Singh *et al.*, 1986; Rasmussen and Schunk, 1988; Singh, 1988]. Studies that included temperature equations assumed that either the heat flow is given by the collision-dominated thermal conductivity [Khazanov *et al.*, 1984; Guiter and Gombosi, 1990] or ignored the heat flow completely [Singh, 1992; Singh and Chan, 1992]. Neither of these assumptions correctly describe the heat transport in the refilling problem [Singh and Horwitz, 1992]. In the collisionless limit of plasma flow during refilling, the usual description of heat flow in terms of Spitzer thermal conductivity breaks down, and such a treatment overestimates the heat flow. When the heat flow becomes large, the validity of such equations ceases, and numerical instabilities result in computational work. Since, a priori it is not known when a large heat flow develops in a model treating plasma flow in a flux tube extending to altitudes of several Earth radii, ad hoc



damping mechanisms are included to damp the heat flow whether it is physically warranted or not [Palmadesso *et al.*, 1988; also C. E. Rasmussen, private communications, 1993]. In modeling of plasma flow at relatively low altitudes, where collisional effects are important, the above problem with the heat flow does not appear to be of a major concern [Koraszewsky *et al.*, 1992].

Despite the above difficulties with the hydrodynamic treatment, it has been used for practical reasons because it provides simplicity and considerable economy in computational work, and depending on the plasma conditions it can work successfully. Therefore it is advisable to keep in mind the assumptions made in using this treatment and, if possible, it is even better to check the validity of this treatment by comparing its prediction against that from a kinetic treatment. Such a comparison may reveal when and how a fluid model succeeds.

The purpose of this paper is to carry out a comparison between models of the plasma flows along closed field lines based on kinetic and hydrodynamic treatments. The former treatment uses a PIC code for ions [Wilson *et al.*, 1992]. The latter one uses transport equations for the flow of mass, momentum, and parallel and perpendicular temperatures of ions [Singh, 1992], but the heat flow is treated heuristically [Metzler *et al.*, 1979]. In both the treatments, electrons are assumed to obey the Boltzmann law. In the present paper the ionospheric outflows is included by imposing a set of boundary conditions on the flow of ions at an altitude of 2000 km. The choice of this altitude is primarily due to the existing models [Wilson *et al.*, 1992; Singh, 1992] in which ionospheric loss and generation processes for the plasma are not yet included.

The closed field lines provide the possibility of a variety of flow conditions ranging from highly supersonic to subsonic flows as an empty flux tube refills. Furthermore, the flows along closed field lines develop counterstreaming due to interhemispheric plasma flows. Since hydrodynamic treatments are most suspect under counterstreaming situations [Manheimer *et al.*, 1976], the comparison carried out here provides a useful guide for assessing the validity and usefulness of a hydrodynamic treatment.

We have found that for the conditions of highly supersonic flows, the two-stream hydrodynamic treatment yields flow properties in good agreement with that from the semikinetic treatment. Demars and Schunk [1991] reported a similar agreement based on 16-moment set of equations including heat flows. We find that the bulk parameters such as the density, flow velocity, and temperatures are in good agreement even for the simpler hydrodynamic model when heat flow is included heuristically; the reason being simply that when the flow is highly supersonic, the dominant transport of heat is through the bulk flow velocity and the transport due to the thermal effects is negligibly small.

When reflection of flows causes counterstreaming, the hydrodynamic treatment gives rise to shock formation, which is not seen from the kinetic treatment. An examination of the shock formation through ion-ion instability shows that off-equatorial shock formation is inhibited by an unfavorable temperature conditions on electron to ion temperature ratio. The issue of the equatorial shock formation remains unsettled here

due to the coarseness of the spatial and temporal resolutions in both the kinetic and hydrodynamic models. When the counterstreaming flows become subsonic, the hydrodynamic and semikinetic treatment again produce flow properties in reasonable agreement.

In order to study plasma flow in space, the plasma treatment must be supplemented by a set of boundary conditions on the flow equation. For the closed field lines, the boundary conditions are determined by the topside ionosphere. The boundary conditions along with the demand for plasma at high altitudes produce the flow. The ionospheric boundary conditions involves generation and loss of ionospheric plasma particle species. Since here our primary goal is in identifying the kinetic and fluidlike behaviors of plasma flow and not the supply of plasma from the ionosphere and the refilling rate, we have simulated the outflow of ionospheric plasma by imposing a set of boundary conditions at an altitude of 2000 km in both the hemispheres. In the semikinetic model, the imposed boundary condition is on the velocity distribution function of the ions entering the flux tube. It is assumed to be half-Maxwellian. The returning particles are self-consistently determined. In the hydrodynamic model the boundary conditions are the moments of such a distribution. Since the kinetic effect dealing with the returning particles are lost in the hydrodynamic model, the hydrodynamic model does not agree with the kinetic model when returning ion flux becomes sufficiently large. Can this disagreement be resolved by a more sophisticated treatment of the heat flow by using a complete set of 16-moment equations? In order to answer this question, further comparative studies are suggested.

The rest of the paper is organized as follows. The theoretical models are described in section 2. The comparison between the results from the two models is carried out in section 3. The main conclusions of the paper and their discussion are given in section 4.

## 2. Theoretical Models

The semikinetic model, which is based on a particle-in-cell code, has been previously described for both open [Wilson *et al.*, 1990] and closed [Wilson *et al.*, 1992] flux tubes. Coulomb collisions are included in the model, the collisions are implemented by pairing simulation ions according to an algorithm which conserves energy and momentum [Takizuka and Abe, 1977]. The algorithm yields good approximation for the collisions when the collisional relaxation time is shorter than the time step in advancing the ion motion. In the hydrodynamic model, we solve the plasma transport equations based on 16-moment approximation [e.g., Ganguli and Palmadesso, 1987, and Barakat and Schunk, 1982]:

$$\frac{\partial n}{\partial t} + \frac{\partial}{\partial s}(nV) = -nV \frac{1}{A} \frac{\partial A}{\partial s} \quad (1)$$

$$\frac{\partial V}{\partial t} + \frac{\partial}{\partial s} \left[ \frac{1}{2} V^2 \right] = \frac{e}{m} E - (k/m) \frac{\partial T_{\parallel}}{\partial s} - (k/m) T_{\parallel} \frac{1}{n} \frac{\partial n}{\partial s}$$

$$-g_{\parallel}(r) - (k/m)(T_{\parallel} - T_{\perp}) \frac{1}{A} \frac{\partial A}{\partial s} + \left[ \frac{\partial \mathcal{N}}{\partial t} \right]_c \quad (2)$$

$$\frac{\partial T_{\parallel}}{\partial t} + \frac{\partial}{\partial s} [V T_{\parallel}] = -T_{\parallel} \frac{\partial \mathcal{N}}{\partial s} - \frac{1}{n} \frac{1}{A} \frac{\partial}{\partial s} (q_{\parallel} A) + \frac{2}{n} q_{\perp} \frac{1}{A} \frac{\partial A}{\partial s} + \left[ \frac{\partial T_{\parallel}}{\partial t} \right]_c \quad (3)$$

$$\frac{\partial T_{\perp}}{\partial t} + \frac{\partial}{\partial s} [V T_{\perp}] = T_{\perp} \frac{\partial \mathcal{N}}{\partial s} - T_{\perp} V \frac{1}{A} \frac{\partial A}{\partial s} + \frac{1}{n} q_{\perp} \frac{1}{A} \frac{\partial A}{\partial s} - \frac{1}{n} \frac{1}{A} \frac{\partial}{\partial s} (q_{\perp} A) + \left[ \frac{\partial T_{\perp}}{\partial t} \right]_c \quad (4)$$

where  $t$  is time,  $r$  is the geocentric distance along the flux tube,  $s$  is the distance along the tube from the northern ionospheric boundary at  $\lambda = +\lambda_o$  (see Figure 1);  $n$ ,  $V$ ,  $T_{\parallel}$ , and  $T_{\perp}$  are the number density, flow velocity, and parallel and perpendicular temperatures of ions in the plasma flow, respectively;  $q_{\parallel}$  and  $q_{\perp}$  are the heat fluxes along the magnetic field line associated with  $T_{\parallel}$  and  $T_{\perp}$ , respectively;  $E$  is the parallel electric field;  $g_{\parallel}$  is the component of the gravitational force parallel to the magnetic field, and  $m$  and  $e$  are the ion mass and charge, respectively. The collision terms denoted by  $[\ ]_c$  are calculated using Burger's Formulae [Burger, 1969], which are modified to include flow velocity corrections [Mitchell and Palmadesso, 1983; Ganguli and Palmadesso, 1987] and the correction for temperature anisotropy [Ichimaru et al., 1973; Singh, 1991].

We do not solve the heat flow equations, which have proven to be quite troublesome to solve numerically [Palmadesso et al., 1988]. The difficulty arises for a relatively large heat flow, for which the moment equations themselves become invalid. Since it is unpredictable in a model when the heat flow may be large, ad hoc procedures are employed to attenuate the heat flow for the numerical stability of the models. This has been found to be true irrespective of the numerical techniques used for solving the equations [Palmadesso et al., 1988; Korosmezey et al., 1992, 1993; also C. E. Rasmussen, private communication, 1993].

In this paper, instead we have included the effects of heat flow heuristically by closely following the treatments in solar wind studies [e.g., Metzler et al., 1979]. In a collisionless plasma the usual picture of heat flow, given by  $q_s = -K_s \nabla T_s$  with  $K_s$  as the thermal conductivity, may not be valid because  $L$ , the mean free path, is  $\gg L_T = (T^{-1} \partial T / \partial s)^{-1}$ , the scale length in the temperature variation. In such a collisionless situation, the heat flux can be calculated on physical ground as follows. The unidirectional heat fluxes  $q_{\parallel}^u$  and  $q_{\perp}^u$  across a surface in a plasma described by a biMaxwellian distribution function with parallel and perpendicular temperatures  $T_{\parallel}$  and  $T_{\perp}$ , respectively, say along the magnetic field vector, are given by

$$q_{\parallel}^u = n k T_{\parallel} (k T_{\parallel} / 2 \pi m)^{1/2} \quad (5)$$

$$q_{\perp}^u = n k T_{\perp} (k T_{\perp} / 2 \pi m)^{1/2} \quad (6)$$

In a uniform plasma for which the distribution function is independent of the parallel coordinate, the heat flow at any point is zero because heat flux in a given direction is cancelled by the heat flux in the opposite direction. In the presence of a spatial inhomogeneity, the cancellation is not complete, and the heat fluxes  $q_{\parallel}$  and  $q_{\perp}$  appearing in equations (3) and (4) can be heuristically written as [Metzler *et al.*, 1979]

$$q_{\alpha} = \epsilon \eta n k T_{\alpha} V_{\alpha} \quad (7)$$

where the subscript  $\alpha$  stands for  $\perp$  or  $\parallel$ ,  $\epsilon = -1$  if  $\partial T_{\alpha} / \partial s > 0$ , and  $\epsilon = 1$  if  $\partial T_{\alpha} / \partial s < 0$ . Thus in the heat flow model adopted here, only the sign of the heat flux depends on the temperature gradient and not its magnitude. The factor  $\eta$  determines the reduction in the heat flow below the unidirectional fluxes in (5) and (6). Later on in this paper we show that  $\eta$  in the range say 0.1 - 0.3 yields results in a reasonable agreement with the kinetic model, in which heat fluxes appear self-consistently. A similar model for heat flow was used by Singh [1992] for plasma flow along open field lines. In both the hydrodynamic and kinetic models adopted here, electric field  $E$  is calculated by assuming that the electrons obey the Boltzmann law and the condition of quasi-neutrality prevails.

The plasma flow along a closed field line is studied by solving an initial-boundary value problem. In the hydrodynamic model, the plasma flows originating from the conjugate ionospheres are treated as separate fluids; this treatment is termed as a two-stream model [Singh, 1988; Rasmussen and Schunk, 1988; Singh, 1990]. In both the models, it is assumed that at the initial time ( $t = 0$ ) the flux tube is highly depleted. The depletion is given by  $n_i = n_o (\sin \lambda / \sin \lambda_o)^6$ , with the minimum density limited to  $10^{-4} n_o$ , where  $n_o$  is the density at the ionospheric base  $\lambda = \pm \lambda_o$  (Figure 1). Initial flow velocity  $V(\lambda, t = 0) = 0$  and temperature  $T_{\perp}(\lambda, t = 0) = T_{\parallel}(\lambda, t = 0) = T_o = 0.3 \text{ eV}$ . In the hydrodynamic model, the boundary condition for the fluids originating from the northern hemisphere are  $n_i(\lambda = \lambda_o, t) = n_o$ ,  $V_n(\lambda = \lambda_o, t) = V_o$ ,  $T_{in}(\lambda_o, t) = T_{\perp}(\lambda_o, t) = T_o$ ; at the boundary  $\lambda = -\lambda_o$  floating boundary conditions are applied. A set of similar boundary conditions is used for the fluid originating from the southern hemisphere, but with the roles of  $\lambda = \pm \lambda_o$  interchanged. In the kinetic model the boundary conditions on ion distribution function  $f(\lambda, V)$  are that  $f(\lambda = \lambda_o, V \geq 0)$  and  $f(\lambda = -\lambda_o, V \leq 0)$  are half-Maxwellians, with a temperature  $T_o$ . These boundary conditions prescribe only the ions entering the flux tubes. The ions leaving the flux tubes are determined by the processes occurring inside it. A half-Maxwellian, and not a displaced Maxwellian, is chosen because of the following reasons. There is no clear observational evidence of supersonic flows along closed field lines at an altitude of 2000 km. Furthermore, our calculations show that in about 2 hours the flow in the flux tube becomes subsonic nearly all along the flux tube; only for an initial stage of about 2 hours, supersonic flows are seen. In view of such uncertainties on the flow velocity at 2000 km, a half-Maxwellian serves the purpose of the comparative study.

### 3. Numerical results

We compare here the properties of the flow in a flux tube with  $L=4$  as seen from the semikinetic and hydrodynamic models. Since the boundary value of the flow velocity ( $V_o$ ) and the heat flow factor  $\eta$  in the hydrodynamic model are free parameters, comparison is performed by varying them over physically reasonable ranges. The comparison also deals with the accumulation of plasma in the flux tube and the equatorial plasma density.

#### 3.1 Initial Supersonic Flow

We recall that the hydrodynamic model is based on two-stream flow in which flows originating from the two hemispheres are treated as separate fluids, and the temporal evolution of the two streams is separately studied. Likewise, even in the semikinetic model, the separate identity of the ions originating from the two hemispheres is maintained. Figure 2 shows the evolution of the flow originating from the northern hemisphere as seen from the semikinetic model. This figure gives the phase-space density plots in  $\lambda - V_{\parallel}$  plane, where  $\lambda$  is the geomagnetic latitude and  $V_{\parallel}$  is the flow velocity along the magnetic field line. The positive and negative values of  $\lambda$  correspond to the northern and southern hemispheres, respectively. The darkest region in the grey-scale plots represents the highest density as indicated by the scale on the right-hand side. At time  $t = 0.003$  hour, the plasma in the tube is essentially the initial plasma with a density profile given by  $n = n_o [\sin \lambda / \sin \lambda_o]^6$ . At later times this plasma expands into the flux tube and it is seen to cross the equator at  $t = 0.25$  hour. Along with the expansion, new plasma enters the flux tube at the boundary  $\lambda = \lambda_o$ . It is seen that by the time  $t = 0.75$  hour, the flow has penetrated all the way to the opposite boundary at  $\lambda = -\lambda_o$ . It is found that the plasma reaching this boundary is not totally lost, but it is partially reflected back, setting up a counterstreaming flow as seen from the plots for  $t \geq 1$  hour. The reflected flow is seen to reach the boundary at  $\lambda = \lambda_o$  by the time  $t = 2$  hours. The plasma flow originating from the southern hemisphere shows a similar behavior as shown in Figure 2, with the role of boundaries at  $\lambda = \pm \lambda_o$  interchanged. It is worth pointing out that after reflections, ions merge with the ion stream moving in the opposite direction, and they do not appear as a separate ion beam.

The possible consequences of the counterstreaming flow will be discussed later on. We now compare the above features of the flow seen from the kinetic model with those seen from the hydrodynamic model. Figures 3a to 3d show the comparison for  $t = 0.5$  hour, these figures show the distributions of (a) density, (b) flow velocity, (c) parallel temperature, and (d) perpendicular temperature. In each panel the curve from the kinetic model is labeled, and the curves from the hydrodynamic model for three values of the heat flow reduction factor  $\eta = 0$ ,  $\eta = 0.05$ , and  $\eta = 0.3$  are indicated by the legend. It is seen from these figures that for most of the flux tube all four curves are quite close together, irrespective of the heat flow factor  $\eta$ . However, near the opposite boundary  $\lambda = -\lambda_o$ , the curves from the hydrodynamic model tend to diverge from the kinetic model, depending on the value of  $\eta$ . This difference between the two

models is attributable to the fact when the flow begins to slow down due to a relative increase in the plasma density, the hydrodynamic model predicts an increase in the parallel temperature as clearly is seen for  $\lambda < -36^\circ$  in Figure 3c. The increase in  $T_{\parallel}$  enhances the pressure and further slows the flow and enhances the density. In the semikinetic model, the temperature enhancement does not occur. Instead, a counterstreaming develops. This contrast between the two models becomes much clearer at later times, for example, at  $t = 1$  hour for which the comparison is shown in Figures 4a to 4d.

Figure 2 shows that at  $t = 1$  hour the reflected ions set up counterstreaming throughout the southern hemisphere ( $\lambda < 0$ ). Since the hydrodynamic model cannot handle the counterstreaming, the reflection process creates a shock, which is clearly seen in the density, velocity, and temperature plots in Figures 4a to 4c, respectively; across the shock indicated by the arrows, density suddenly increases, flow velocity decreases and the parallel temperature also increases. We note that the hydrodynamic curves for different values of  $\eta$  begin to show some difference among themselves, with the curve for  $\eta = 0.3$  being closest to that from the kinetic model. It is worth pointing out that the flow velocity in the kinetic model is the average over the counterstreaming ions. The average velocity is lower than that from the hydrodynamic model over the region of the counterstreaming, but where the counterstreaming has not yet occurred ( $\lambda > 30^\circ$ ) the flow velocities from the two models are generally in good agreement.

The shock first propagates upward to the equator and then downward and reaches the ionospheric boundary at  $\lambda = \lambda_o$  at  $t \approx 2$  hours. The propagation of the shock in the density profile is shown by the arrows in Figure 5. The transit time of about 2 hours for the shock is in agreement with the development of the counterstreaming starting in the southern hemisphere and spreading to the northern ionospheric boundary by  $t = 2$  hours. (see Figure 2). We find that the heat flow plays only a minor role in the motion of the shock; the shock speed is slightly enhanced with increased heat flow  $\eta$ ; for  $\eta = 0.3$  and  $0.05$  the shock is already absorbed near the boundary  $\lambda \approx \lambda_o$ , while for  $\eta = 0$ , the shock can be still seen in the flux tube at  $t = 2$  hours.

After the shock reaches the boundary at  $\lambda = \lambda_o$ , the flow in the flux tube becomes generally subsonic with respect to the ionacoustic speed, which is about  $10 \text{ km/s}$  with electron and ion temperatures  $T_o = 0.3 \text{ eV}$  at  $\lambda = \pm \lambda_o$ . We will discuss the subsonic stage after we examine the reason why a shock did not form during the early stage ( $\sim 1$  hour) of the counterstreaming (Figure 2) in the semikinetic model.

### 3.2. Electrostatic Shock

We have just seen that a shock automatically forms in the hydrodynamic model as soon as the flow begins to reflect near the opposite boundary. On the other hand, the kinetic model does not show the shock formation. Instead, a counterstreaming flow develops. We examine this issue in terms of the conditions for shock formation and ion velocity distribution function.

According to the original suggestion of Banks *et al.*, [1971], a shock should form when supersonic flow from the conjugate hemispheres collide at the equator. The flows collide as early as

$t = 0.25$  hour, the flows from the northern hemisphere can be seen from Figure 2, and the corresponding flow from the southern hemisphere is the mirror image of this flow with respect to the equator. When the flow begins to overlap, the shock should form through the ion-ion instability. The conditions for such an instability in a colliding situation are given

$$1.3v_{ii} \leq V_b \leq MC_s, \quad T_e > 3T_i \quad (8)$$

where  $v_{ii}$  is the ion thermal velocity,  $V_b$  is the ion beam velocity,  $C_s$  is the ion-acoustic speed and  $M$  is the mach number, which could be as large as 4 [Forstlund and Shonk, 1970; Montgomery and Joyce, 1969]. However, it must be mentioned here that high critical Mach number  $M \cong 4$  is determined by the nonlinear evolution of the electron dynamics, including trapping and heating of electrons [e.g., Singh, 1988]. For isothermal electrons, as it is assumed in the semikinetic model,  $M = 1.6$  [Tidman and Krall, 1971]. It is worth pointing out that for large beam velocities, oblique ion waves propagating at an angle from the magnetic field are likely to be excited. However, the role of such highly oblique waves, which are likely to occur for highly supersonic beams, in momentum exchange between interpenetrating beams and shock formation is not well understood.

We examine here the likelihood of the instability occurring from the flow parameters given by the semikinetic model. First, we do this exercise for  $t = 30$  min. when the flow has crossed the equator. Figure 6 shows the average flow velocity  $V_b$ , the temperature ratio  $T_e/T_i$ , and the ion-acoustic speed  $C_s$  as a function of geomagnetic latitude for the flow at  $t = 30$  min., shown in Figure 2. Note that the temperature ratio is plotted after multiplying it by 10, so that all the line plots in Figure 6 can utilize the same vertical scale.  $C_s$  is calculated from  $C_s = [k(T_e + 3T_i)/m]^{1/2}$ . The critical temperature ratio  $T_e/T_i = 0.33$  for the instability is shown by the segment of the thick horizontal line in Figure 6. It is seen that the ions have sufficiently cooled down to meet the instability condition on the ion temperature over an extended equatorial region ( $|\lambda| \leq 20^\circ$ ). The flow coming from the opposite hemisphere shows a similar feature. The ionacoustic speed in the equatorial region is about  $8 \text{ km/s}$ . It is seen that over the latitudinal region ( $|\lambda| \leq 20^\circ$ ), the ion beam velocity is about  $V_b \cong 2C_s$ . In the semikinetic and hydrodynamic models discussed here the electrons are assumed to obey the Boltzmann law. Therefore ion beams with such velocities are too fast to excite the ion-ion instability and thereby to form shocks in the model. Furthermore, it is important to point out that the processes which lead to shock formation, including the ion-ion instability, are microprocesses, which are suppressed in the large-scale models [Singh and Cham, 1993]. If electrons dynamics were rigorously included in the model and the associated microprocesses properly resolved, it is likely that the ion-ion interaction would have occurred forming shocks.

Figure 7 shows the drift velocity  $V_b$ ,  $C_s$ , and  $T_e/T_i$  at  $t = 1$  hour for the flow originating from the northern hemisphere. It is seen that as the ion beam penetrates into the opposite hemisphere ( $\lambda < 0$ ), it gets progressively warmer and the temperature condition  $T_e/T_i \leq 0.3$  is not met beyond  $|\lambda| = 10^\circ$ . Thus ion instability and shock formation are not

expected. This indicates that the shock formation in the hydrodynamic model (Figures 4 and 5) is an artifact of the model.

In view of the above discussion in connection with Figures 6 and 7, it emerges that on the basis of temperature condition alone, it can be argued that if shocks form, they should be during the early stage when the ion beams begin to interpenetrate in the equatorial region. During later stages, when the beams penetrate into the opposite hemispheres, the shock formation is not likely unless somehow electrons are heated, enhancing the temperature ratio  $T_e/T_i$ . However, as mentioned earlier the shock formation in the equatorial region requires a rigorous treatment of electron dynamics. In view of the simplified treatment of electrons in the models described here, and relatively coarse spatial and temporal resolutions afforded by them the issue of equatorial shock formation cannot be settled in this paper.

### 3.3. Subsonic Flow

After the initial stage of supersonic flows from the conjugate ionospheres, the flows become generally subsonic. This is predicted from both the models. Figure 8 shows the status of the flow at  $t = 4$  hours, from both the hydrodynamic and semikinetic models. As before, there are three curves from the hydrodynamic model which are compared against the curve from the semikinetic model. Figure 8b shows that the flow velocities obtained for different values of  $\eta$  from the hydrodynamic model agree with the flow velocity given by the kinetic model. The maximum flow velocity of about  $5 \text{ km/s}$  seen near the boundary  $\lambda = \lambda_0$  is subsonic with respect to the ion-acoustic speed  $C_s = 10 \text{ km/s}$ . We note that the average flow velocity peaks slightly above the boundary in both hydrodynamic and kinetic models. The peaking is a consequence of the boundary conditions at  $\lambda = \lambda_0$  and the acceleration of ions by the pressure and electric field distributions in close vicinity of the northern boundary of the flux tube.

Figures 8a, 8c, and 8d show that for the subsonic flow the density and temperature structures critically depend on the heat flow factor  $\eta$ . For  $\eta = 0.3$ , the hydrodynamic model yields results in good agreement with those from the kinetic model. When  $\eta$  becomes too small ( $\eta = 0.05$ ), the structures in the density and temperature profiles markedly differ from the kinetic model; the density structure shows an extended density cavity in the equatorial region, where parallel temperature is relatively high [Singh, 1991]. Furthermore, for low values of  $\eta$  there is density enhancement and correspondingly a low parallel temperature in the southern hemisphere. When heat flow factor is sufficiently large ( $\eta > 0.15$ ), such structures in  $n(\lambda)$  and  $T_{\parallel}(\lambda)$  are washed away. In a recent paper, Ho *et al.* [1993] made a similar observation regarding evolution of density perturbations in the polar wind by comparing semikinetic and hydrodynamic models for an open flux tube.

The comparison between the hydrodynamic and kinetic results at  $t = 12$  hours is shown in Figures 9a to 9d. The density and temperature structures at this stage are qualitatively similar to that at  $t = 4$  hours as shown in Figures 8a to 8d. However it is seen that at  $t = 12$  hours, the density and temperature profiles even for  $\eta = 0.05$  have begun to compare well with that for  $\eta = 0.3$ , for which the density distribution agrees well with that



given by the semikinetic treatment. The discrepancy between the densities predicted by the kinetic treatment and the hydrodynamic one for  $\eta = 0.3$  is bounded by 15%, for most part of the flux tube, except near the southern boundary  $\lambda = -\lambda_0$ .

The runs for the comparison between the hydrodynamic and kinetic models were carried on until  $t = 48$  hours. For time  $t > 12$  hours, it was found that the hydrodynamic model systematically yields densities higher than that given by the semikinetic model. Figure 10 shows the comparison between the equatorial densities as obtained from the two models. This figure shows the temporal evolution of the equatorial densities found from the kinetic (solid line) and the hydrodynamic (dashed line curves) models. For the latter model, the densities are plotted for different values of the flow velocity  $V_0$  at the boundaries  $\lambda = \pm\lambda_0$ . We remind ourselves that the results from the hydrodynamic model shown in Figures 3, 4, 5, and 8 are for a flow velocity  $V_0 = (kT_0 / 2\pi m)^{1/2} = 0.39V_i$ . We notice from Figure 10 that for this boundary value of the flow velocity, the kinetic and hydrodynamic curves are remarkably close for  $t = 12$  hours. This implies that this boundary value of the flow velocity closely corresponds to the input flux determined by a half-Maxwellian distribution function, which is imposed as a boundary condition in the kinetic model. For  $t > 12$  hours, the boundary value of  $V_0 = 0.39V_i$  yields an overfilling compared to the kinetic model. This simply implies that the net influx of ion into the flux tube at the ionospheric boundaries steadily decreases in the kinetic model, primarily due to the ions flowing out of the flux tube. On the other hand, in the hydrodynamic model, the influx is primarily determined by the imposed flow velocity, and it remains constant. This is demonstrated by comparing the temporal evolution of the total plasma content in the flux tube as seen from the two models.

Figure 11 shows the total content as a function of time. As in Figure 10, for the hydrodynamic model the curves are for different values of the imposed velocity at the boundary. It is seen that for  $V_0 = 0.39V_i$ , the hydrodynamic model yields nearly the same total plasma content as the kinetic model with nearly the same rate of increase in it for  $t = 12$  hours. At later times, the content from the kinetic model shows a tendency toward saturation because the rate of increase in the content continuously decreases. Even in the hydrodynamic model there is a tendency toward the decreasing rate, but the decrease is much slower. This difference in the influx of the ions from the two models has a simple explanation. In the kinetic model, some of the ions have the liberty to exit the flux tube as they are scattered by Coulomb collisions, or as they simply flow out. On the other hand, in the hydrodynamic model the plasma entering the flux tube can leave the system only through the opposite boundary, where the flow velocity becomes exceedingly small after the shock phase ( $t > 2$  hours). This implies that in the hydrodynamic model there is no provision for the plasma to leave the system. The slight tendency toward the saturation in the hydrodynamic model is due to the changing plasma condition near the boundary where the flow originates. As the plasma density near this boundary increases, the influx into the flux tends to decrease.

Figures 10 and 11 also show the equatorial density and the total plasma content from the hydrodynamic model for  $V_0 = 0.1V_i$ .

and  $V_o = 0$ . It is seen that even for  $V_o = 0$ , the equatorial density and the total content are increasing with time and, in about 48 hours, they tend to approach the corresponding results from the kinetic model. It may sound strange how refilling can occur with a boundary condition of  $V_o = 0$ ! The refilling of a flux tube with zero flow velocity as boundary conditions in a hydrodynamic model was previously described by Singh *et al.*, [1986].

The ion flux developing near the boundaries from the kinetic model and the hydrodynamic model for  $V_o = 0.39V_i$  during the early times ( $t < 12$  hours) is  $1.8 \times 10^8$  ions  $cm^{-2}s^{-1}$ . In the kinetic model, this flux continuously decreases because some of the ions entering the flux tube eventually leave. However, in the hydrodynamic model the plasma entering the flux tube remains in it, causing the overrefilling for  $t > 12$  hours when  $V_o = 0.39V_i$ . When  $V_o = 0$ , the hydrodynamic model yields a flux of  $\leq 10^8$  ions  $cm^{-2}s^{-1}$ , and it continuously decreases as the forces (determined by density and temperature gradients) on the ions accelerating them into the flux tube from the boundary cells diminishes with the refilling. It is worth mentioning that the comparison carried out above is based on the simplified boundary conditions in the kinetic and fluid treatments and a heuristic treatment of the heat flow. A comparison of the plasma treatments without these simplifications will be worthwhile.

A comparison of plasma distributions in the flux tube at a relatively late time ( $t = 48$  hours), as obtained from the two models, is shown in Figures 12a to 12d. For the hydrodynamic model,  $\eta = 0.3$ , and the distributions are given for three values of the boundary velocity:  $V_o = 0.39V_i$ ,  $0.1V_i$ , and 0. Density profiles in Figure 12a show the overrefilling for  $V_o = 0.39V_i$ , but when  $V_o$  is reduced below  $0.1V_i$ , the density profiles from the two models disagree near the boundary  $\lambda = \lambda_o$ , but away from it the agreement considerably improves. The disagreement near the boundary is also reflected in the velocity profiles in Figure 12b. Despite the above disagreement in the density and velocity profiles near the boundary, the temperature structures obtained from the two models are nearly identical. Temperature is nearly isotropic ( $T_{\parallel} \approx T_{\perp}$ ); it rises to about 0.4 eV in the equatorial region from the boundary value of 0.3 eV. In the late stage of the refilling, the similarity between the temperature profiles, despite the differences in the density and velocity profiles from the two models, can be understood by examining the temperature equations (3) and (4) and the flow properties. Since the flow velocity is small, the velocity profile has little effect on the temperature profiles. The maximum flow velocity in a localized region near the boundary is  $2.5 km s^{-1}$ , compared to the thermal velocity of  $5.5 km s^{-1}$  and ion-acoustic speed of  $10 km s^{-1}$ . The density distribution affects the temperature distribution through the heat flow terms in equations (3) and (4). In the late stage of the flow when the gradients have smoothed out and the densities are relatively large, the density distribution also has insignificant effects on the heat flow.

#### 4. Conclusion and discussion

We have carried out a comparison between semikinetic and hydrodynamic models for plasma flow along closed magnetic field lines. The comparison has direct relevance to the problem of plasmaspheric refilling. It is found that the comparison does

not depend only on the plasma physics afforded by the models, but it also strongly depends on the boundary condition on the flow velocity. In a kinetic model, an appropriate boundary condition is to prescribe the velocity distributions of the inflowing ions to be half-Maxwellian for  $V \geq 0$  at  $\lambda = \lambda_0$  and for  $V \leq 0$  at  $\lambda = -\lambda_0$ . In the hydrodynamic model this boundary condition corresponds to the drift velocity  $V_0 = (kT_0 / 2\pi m)^{1/2}$ . A comparison of results from the two models with such boundary conditions revealed the following important features of the flows.

1. When supersonic flows develop in response to a sudden depletion in a flux tube, the hydrodynamic and kinetic models yield distribution of density, flow velocity, and temperatures in generally good agreement. The temperature distributions in the region of supersonic flows are found to be remarkably similar, showing small effect of the heat flow. It is worth pointing out that *Demars and Shunk* [1991] compared the behavior of a highly supersonic plasma flow from a hydrodynamic model based on a more complete (16-moment) set of equations with that from a semikinetic model, demonstrating a good agreement. We have demonstrated here that, for a highly supersonic flow, even a much simpler set of hydrodynamic equations are adequate. It is physically explained by the fact that the transport of heat in a supersonic flow is dominated by the large drift velocity and not by the heat flow process. Mathematically speaking, it implies that the heat flow terms are negligibly small compared to the convective terms in the temperature equations.

2. Both models show reflection of the supersonic flow when it penetrates deep into the opposite hemisphere. Since even a two-stream hydrodynamic model cannot handle the counterstreaming for a given flow, the reflection automatically leads to a shock formation [*Rasmussen and Schunk*, 1988; *Singh*, 1991]. The shock first moves upward toward the equator and then downward to the ionospheric boundary. An examination of the plasma conditions for shock formation shows that the shock seen in the hydrodynamic model is an artifact of the model; the ion beams are found to be too warm to excite the ion-ion instability which can subsequently produce a shock. The semikinetic model shows the development of counterstreaming for the flow; the counterstreaming advances to the equator and downward to ionospheric boundary. It turns out that the transit time of the shock all the way to the ionospheric boundary and the time for the counterstreaming to spread to this boundary are nearly the same, about 2 hours. In a previous paper, *Singh* [1991] reported the shock transit time to be about 4 hours, which is in error due to a normalization factor of 2. In view of the short transit time of the shock, the shock formation does not significantly affect the refilling, as evidenced by the comparison of the flows from the hydrodynamic and kinetic models for later times.

Lack of shock formation in the equatorial region, when the ion beams begin to interpenetrate [*Banks et al.*, 1971] is uncertain in view of the spatial and temporal resolutions afforded by a large-scale model and the simplicity in handling the electron dynamics by the Boltzmann Law.

3. After about 2 hours, the flow in each hemisphere becomes subsonic with respect to the ion-acoustic speed. This is seen from both models.

4. A comparison of the total plasma contents and the equatorial densities from the two models indicates a good agreement up to about  $t \approx 12$  hours, after which the hydrodynamic model indicates overrefilling of the flux tube. The overrefilling is traced to the inability of our hydrodynamic model to control the net plasma inflow by the returning particles. The inflow is determined by the imposed boundary conditions and the outflow of plasma is exceedingly small. On the other hand, in the kinetic model the influx gradually decreases due to ions returning from the flux tube, showing a tendency toward saturation in the refilling in about 2 days. It is worth pointing out that it will be useful to perform a study comparing the models based on the kinetic and hydrodynamic treatments by relaxing some of the simplifications in terms of boundary conditions and in handling the heat flow in the latter treatment. The boundary conditions can be relaxed by including the ionospheric plasma generation processes at low altitudes [Guter and Gombosi, 1990].

When the boundary flow velocity in the hydrodynamic model reduces below  $V_0 = (kT_0 / 2\pi m)^{1/2}$ , there is an initial underfilling, but eventually, the refilling from this model catches up to that given by the semikinetic model. For example, when  $V_0 = 0$ , the degree of refilling from the two models, in terms of both the equatorial density and the total plasma content in the flux tube, becomes approximately the same in about 2 days.

In some previous studies [Singh *et al.*, 1986; Rasmussen and Schunk, 1988; Singh, 1991], a boundary condition of zero flow velocity was used. It may appear strange that a refilling occurs with this boundary condition on the flow velocity. The issue is briefly revisited here.

From the comparison of the plasma contents and the equatorial densities given by the models, it is concluded that after about 12 hours, the choice of boundary condition in the hydrodynamic model is quite uncertain. In view of this uncertainty, the choice of zero-velocity boundary could be useful during the late stage of the refilling, it yields underrefilling only near the boundaries, where the density and average flow velocity show a discontinuity in the flow. otherwise, over the rest of the flux tube the density and flow velocity are in quite good agreement with those given by the kinetic model.

The hydrodynamic model described here is a two-stream model and includes equation for the parallel and perpendicular temperatures. Single-stream hydrodynamic models [Singh *et al.*, 1986; Guter and Gombosi, 1990] suffer from the shortcoming that they generate shocks at the equator whether the plasma conditions allow them or not. The single- and two-stream models with assumed temperature isotropy suffer from the shortcoming that the shock transit time is fairly long, and a major part of the refilling occurs through supersonic flows from the ionospheres [Singh *et al.*, 1986; Rasmussen and Schunk, 1988; Singh, 1991]. This is in contrast to the two-stream model with a self-consistent treatment of the temperature anisotropy; this model yields evolution from supersonic to subsonic flows at the same timescale as the kinetic model. In this sense the heuristic treatment of the heat flow described in this paper appears to be adequate. This treatment also appears to be adequate even in the subsonic stage as long as the flow velocity near the boundary is relatively large near the thermal speed, for

example, for  $t < 12$  hours in our present calculations. However, when the flow velocity becomes sufficiently low so that a large fraction of injected ions in the kinetic model begin to return from the immediate vicinity of the boundary, the boundary conditions for the hydrodynamic model diverges from that of the kinetic treatment because this model does not allow for a return flux for a given stream. Can this situation be improved by a more rigorous treatment of the heat flow and/or by properly including the ionospheric plasma supply [Guter and Gombosi, 1990]? In order to answer this question, it will be useful to compare models based on (1) the heuristic heat flow treatment, (2) a more sophisticated treatment of the heat flow using 16-moment set of transport equations, and (3) the semikinetic treatment, and all models properly including the analogous ionospheric boundary conditions. If the model (1) compares well with the latter ones, the computational effort in using transport equations for modeling space plasma will be considerably reduced.

**Acknowledgments.** This work was supported by NASA grants NAGW-2128, NAG8-239, and NSF grant ATM 8911799 made to the University of Alabama in Huntsville.

*The Editor thanks A. R. Barakat and an other referee for their assistance in evaluating this paper.*

## References

- Banks, P. M., A. F. Nagy, and W. I. Axford, Dynamical behavior of thermal protons in the mid-latitude ionosphere and magnetosphere, *Planet. Space Sci.*, **19**, 1053, 1971.
- Barakat, A. R., and R. W. Schunk, Transport Equations for multicomponent anisotropic space plasma: A review, *Plasma Phys.*, **24**, 389, 1982.
- Burgers, S. M., *Flow Equations for Composite Gases*, Academic, San Diego, Calif., 1969.
- Demars, H. G. and R. W. Schunk, Comparison of semikinetic and generalized transport models of the polar wind, *Geophys. Res. Lett.*, **18**, 1841, 1991.
- Forslund D. W., and C. R. Shonk, Formation of electrostatic collisionless shocks, *Phys. Rev. Lett.*, **25**, 1699, 1970.
- Ganguli, S. B., and P. J. Palmadesso, Plasma transport in the auroral current region, *J. Geophys. Res.*, **92**, 8673, 1987.
- Gombosi, T. and C. E. Rasmussen, Transport of gyration-dominated space plasmas of thermal origin, 1. Generalized transport equations, *J. Geophys. Res.*, **96**, 7759, 1991.
- Guter, S. M., and T. Gombosi, The Role of high-speed plasma flows in plasmaspheric refilling, *J. Geophys. Res.*, **95**, 10,427, 1990.
- Ho, W., J. L. Horwitz, N. Singh, and G. R. Wilson, Plasma expansion and evolution of density perturbations in the polar wind: Comparison of semikinetic and transport models, *J. Geophys. Res.*, **98**, 13,581, 1993.
- Ichimaru, S., *Basic Principles of Plasma Physics*, Chap. 10, Benjamin Cummings, Reading, Mass., 1973.
- Khazanov, G. V., M. A. Kuen, Yu. V. Konikov and I. M. Sidorov, Simulation of ionosphere-plasmasphere coupling taking into account ion inertia and temperature anisotropy, *Planet. Space Sci.*, **32**, 585, 1984.
- Korosmezey, A., C. E. Rasmussen, T. I. Gombosi, and G. V. Khazanov, Anisotropic ion heating and parallel  $o^+$  acceleration in regions of rapid  $E \times B$  convection, *Geophys. Res. Lett.*, **19**, 2297, 1992.

- Korosmezey, A., C. E. Rasmussen, T. I. Gombosi, and B. an Leer, Transport of gyration-dominated space plasmas of thermal origin, 2. Numerical solutions, *J. Comp. Phys.*, 109, 16, 1993.
- Manheimer, W. M., M. Lanks, and R. W. Clark, Multistreaming and the viability of fluid codes, *Phys. Fluids*, 19, 1788, 1976.
- Metzler, N., S. Cuperman, M. Dryer, and P. Rosenau, A time-dependent two-fluid model with thermal conduction for the solar wind, *Astrophys. J.*, 231, 960, 1979.
- Mitchell, H. G., and P. J. Palmadesso, A dynamic model for the auroral field line plasma in the presence of field-aligned current, *J. Geophys. Res.*, 88, 2131, 1983.
- Montgomery, D. and G. Joyce, Shock-like solutions of electrostatic Vlasov equation, *J. Plasma Physics*, 3, part 1, 1, 1969.
- Palmadesso, P. J., S. B. Ganguli, and H. G. Mitchell, Jr., Multi-component fluid imulations of transport processes in the auroral zone, in *Modeling Magnetospheric Plasma*, *Geophys. Monogr. Ser.*, vol. 44, edited by T. E. Moore and J. H. Waite, Jr., p. 133, AGU, Washington, D. C., 1988.
- Rasmussen, C. E., and R. W. Schunk, Multistream hydrodynamic modeling of interhemispheric plasma flow, *J. Geophys. Res.*, 91, 14557, 1988.
- Schunk, R. W., Mathematical structure of transport equations for multispecies plasma flow, *Rev. Geophys. Space Phys.*, 15, 429, 1977.
- Singh, N., Refilling of a plasmaspheric flux tube-microscopic plasma processes, in *Magnetospheric Plasma*, *Geophys. Monogr. Ser.*, vol. 44, Edited by T. E. Moore and J. H. Waite, Jr., p. 87, AGU, Washington, D. C., 1988.
- Singh, N., Comment on "Multistream Hydrodynamic Modeling of Interhemispheric Plasma Flow" by C. E. Rasmussen and R. W. Schunk, *J. Geophys. Res.*, 95, 17,273, 1990.
- Singh, N., Role of Ion Temperature anisotropy in multistage refilling of the outer plasmaspheric, *Geo. Res. Lett.*, 18, 817, 1991.
- Singh, N., Plasma perturbations created by transverse ion heating events in the magnetosphere, *J. Geophys. Res.*, 97, 4235, 1992.
- Singh, N. and C. B. Chan, Effects of equatorially trapped ions as refilling of the plasmasphere, *J. Geophys. Res.*, 97, 1167, 1992.
- Singh, N. and C. B. Chan, Numerical simulation of plasma processes driven by transverse ion heating, *J. Geophys. Res.*, 98, 11, 667, 1993.
- Singh, N. and J. L. Horwitz, Plasmasphere refilling: Recent observations and modeling, *J. Geophys. Res.*, 97, 1047, 1992.
- Singh, N., R. W. Schunk, and H. Thiemann, Temporal features of the refilling of a plasmaspheric flux tube, *J. Geophys. Res.*, 91, 13433, 1986.
- Takizuka, T. and H. Abe, A binary collision model for plasma simulation with a particle code, *J. Comp. Phys.*, 25, 205, 1977.
- Tidman, D. A., and N. A. Krall, *Shock Waves in Collisionless Plasmas*, Wiley-Interscience, New York, 1971.
- Wilson, G. R., C. W. Ho, J. L. Horwitz, N. Singh, and T. E. More, A new kinetic model for time-dependent polar plasma outflow: Initial results, *Geophys. Res. Lett.*, 17, 263, 1990.
- Wilson, G. R., J. L. Horwitz, and J. Lin, A semikinetic model for early stage plasmasphere refilling, 1: Effects of coulomb collisions, *J. Geophys. Res.*, 91, 1109, 1992.

J. L. Horwitz and G. R. Wilson, Department of Physics and CSPAR, University of Alabama, Huntsville, AL 35899.

Nagendra Singh, Department of Electrical and Computer Engineering and CSPAR, University of Alabama, Huntsville, AL 35899.

(Received September 21, 1993; revised October 1, 1993; accepted October 6, 1993.)

[illegible]

**Figure 2.** Temporal evolution of the flow originating from the northern hemisphere; phase-space ( $x-V_{||}$ ) plots are shown. The plot at  $t = .003$  hour nearly shows the initial plasma in the flux tube.

**Figure 3.** Comparison of flows from semikinetic and hydrodynamic models at  $t = 30$  minutes. For the latter model flows are given for  $\eta = 0, 0.05$  and  $0.3$ : (a) density, (b) flow velocity, (c) parallel temperature, and (d) perpendicular temperature distributions. For most latitudes the curves are so close together that it is difficult to distinguish them.

Figure 4. Same as Figure 3, but at  $t = 1$  hour. The hydrodynamic curves are distinguished by the presence of a shock which is manifested by sudden jumps in density, flow velocity and parallel temperature near  $\lambda \cong -25$ . Shocks are indicated by the arrows.

Figure 5. Propagation of the shock is shown through the jump in the density profiles at (a)  $t = 1$  hour, (b)  $t = 1.5$  hours, and (c)  $t = 2$  hours. For the purpose of comparison the curve from the kinetic model and three curves for  $\eta = 0, 0.05$ , and  $0.3$  from the hydrodynamic model are shown. Shocks are indicated by arrows.

Figure 6. Distribution of flow parameters from the kinetic model. The average flow velocity  $V_b$ , ion-acoustic speed  $C_i$ , and the temperature ratio  $T_{\parallel}/T_{\perp}$  for ions with  $V_{\parallel} > 0$  are shown for the purpose of instability analysis at  $t = 30$  minutes. The corresponding curves for  $V_{\parallel} < 0$  can be deduced from the symmetry considerations.

Figure 7. Same as Figure 6, but at  $t = 1$  hour.

Figure 8. Same as Figure 4, but at  $t = 4$  hours.

Figure 9. Same as Figure 4, but at  $t = 12$  hours.

Figure 10. Temporal evaluation of the equatorial density from the kinetic model and from the hydrodynamic model for three values of  $V_o$ ,  $0.39 V_i$ ,  $0.1 V_i$ , and  $0 V_i$ .

Figure 11. Temporal evolution of the total plasma content in the flux tube for the kinetic and hydrodynamic models.

Figure 12. Distribution of (a) density, (b) flow velocity, (c) parallel temperatures and (d) perpendicular temperature at  $t = 48$  hours. All vertical scales are linear in this Figure. There are three curves from the hydrodynamic model for  $V_o = 0, 0.1 V_i$ , and  $0.39 V_i$ .

Figure 1. Geometry of a closed magnetic flux tube. The latitudinal angle  $\lambda$  and the geocentric distance  $r$  are shown. The ionospheric boundaries are at  $s = 0 (\lambda = \lambda_o)$ , and  $s = s_{\max} (\lambda = \lambda_o)$ .

Figure 2. Temporal evolution of the flow originating from the northern hemisphere; phase-space ( $s - V_{\parallel}$ ) plots are shown. The plot at  $t = .003$  hour nearly shows the initial plasma in the flux tube.

Figure 3. Comparison of flows from semikinetic and hydrodynamic models at  $t = 30$  minutes. For the latter model flows are given for  $\eta = 0, 0.05$  and  $0.3$ : (a) density, (b) flow velocity, (c) parallel temperature, and (d) perpendicular temperature distributions. For most latitudes the curves are so close together that it is difficult to distinguish them.

Figure 4. Same as Figure 3, but at  $t = 1$  hour. The hydrodynamic curves are distinguished by the presence of a shock which is manifested by sudden jumps in density, flow velocity and parallel temperature near  $\lambda \cong -25$ . Shocks are indicated by the arrows.



Figure 5. Propagation of the shock is shown through the jump in the density profiles at (a)  $t = 1$  hour, (b)  $t = 1.5$  hours, and (c)  $t = 2$  hours. For the purpose of comparison the curve from the kinetic model and three curves for  $\eta = 0, 0.05$ , and  $0.3$  from the hydrodynamic model are shown. Shocks are indicated by arrows.

Figure 6. Distribution of flow parameters from the kinetic model. The average flow velocity  $V_b$ , ion-acoustic speed  $C_s$ , and the temperature ratio  $T_{\parallel}/T_{\perp}$  for ions with  $V_{\parallel} > 0$  are shown for the purpose of instability analysis at  $t = 30$  minutes. The corresponding curves for  $V_{\parallel} < 0$  can be deduced from the symmetry considerations.

Figure 7. Same as Figure 6, but at  $t = 1$  hour.

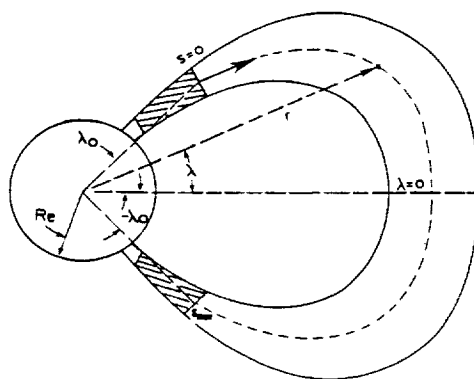
Figure 8. Same as Figure 4, but at  $t = 4$  hours.

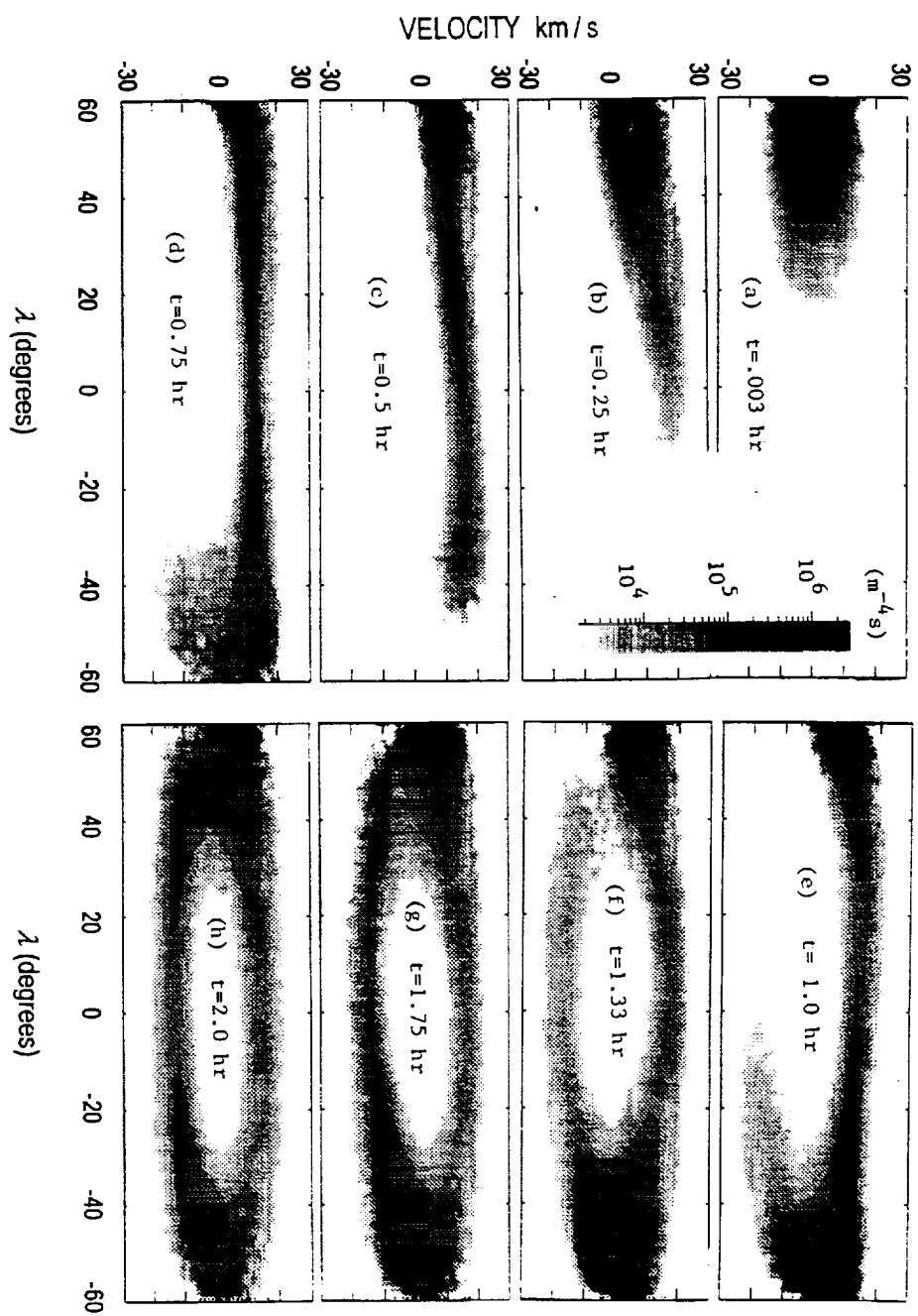
Figure 9. Same as Figure 4, but at  $t = 12$  hours.

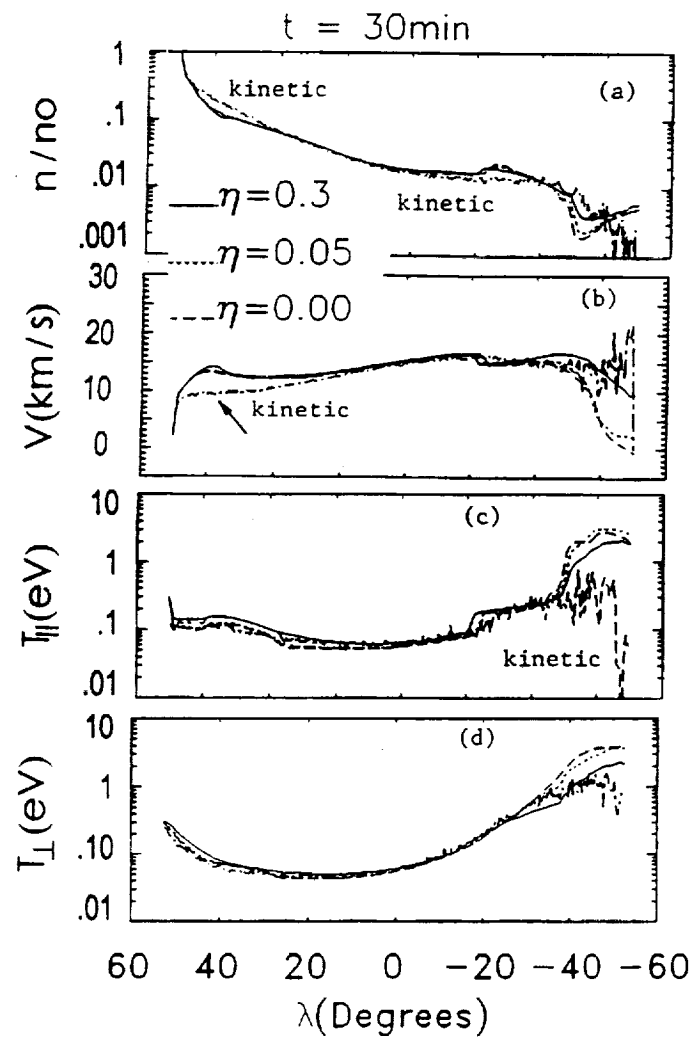
Figure 10. Temporal evaluation of the equatorial density from the kinetic model and from the hydrodynamic model for three values of  $V_o$ ,  $0.39 V_i$ ,  $0.1 V_i$ , and  $0 V_i$ .

Figure 11. Temporal evolution of the total plasma content in the flux tube for the kinetic and hydrodynamic models.

Figure 12. Distribution of (a) density, (b) flow velocity, (c) parallel temperatures and (d) perpendicular temperature at  $t = 48$  hours. All vertical scales are linear in this Figure. There are three curves from the hydrodynamic model for  $V_o = 0, 0.1 V_i$ , and  $0.39 V_i$ .







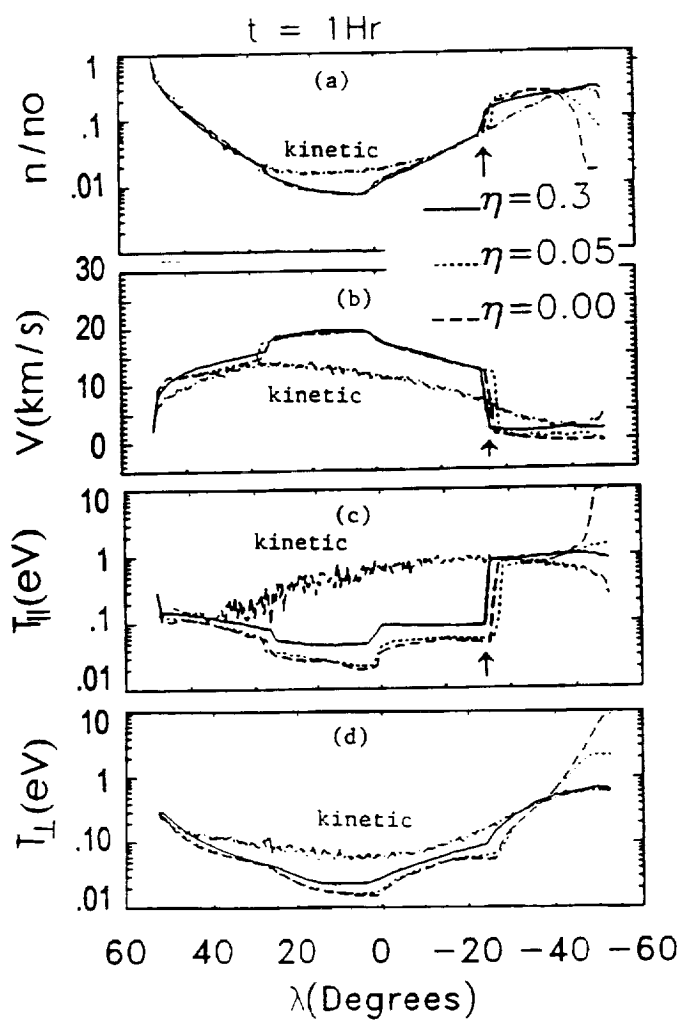
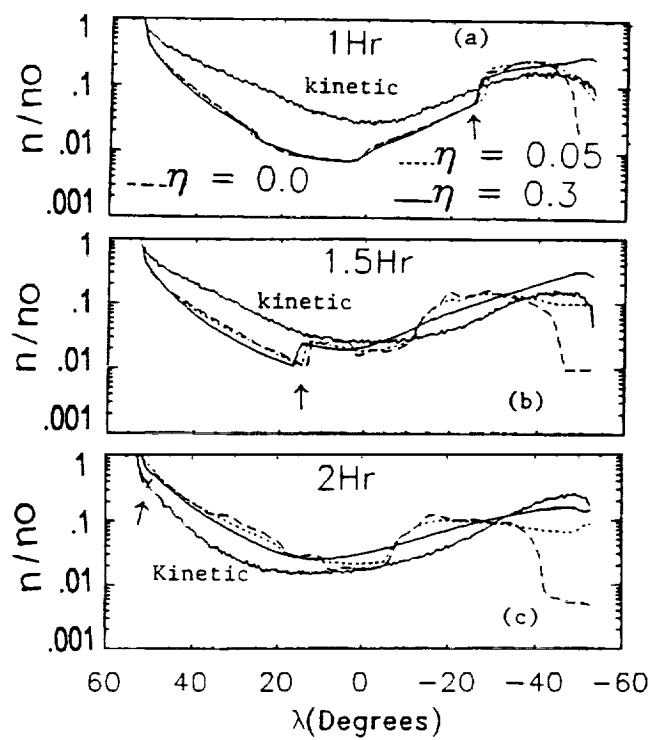
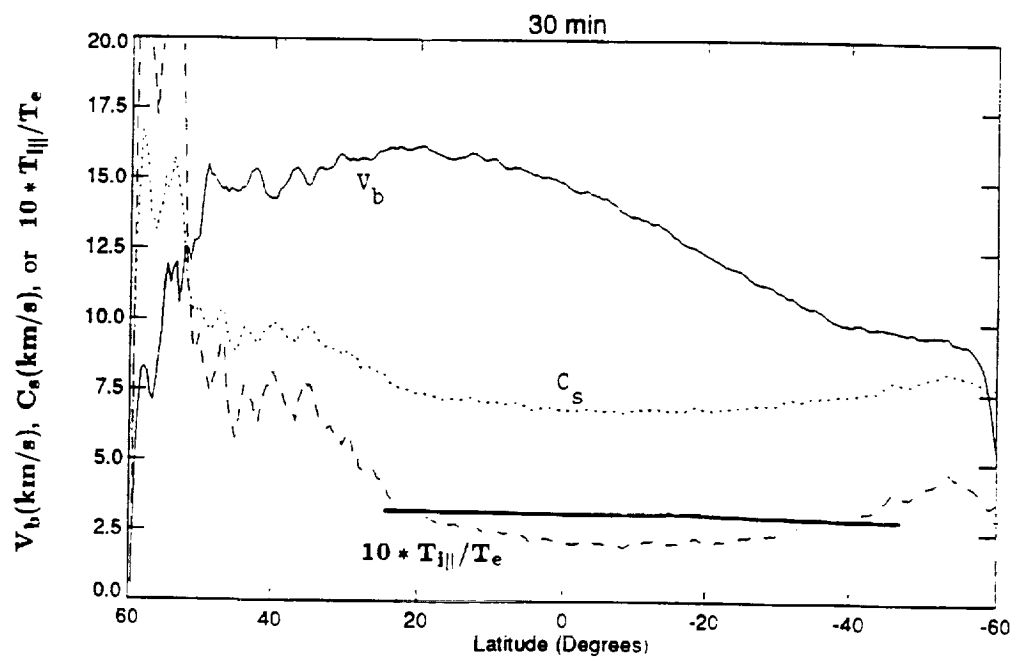
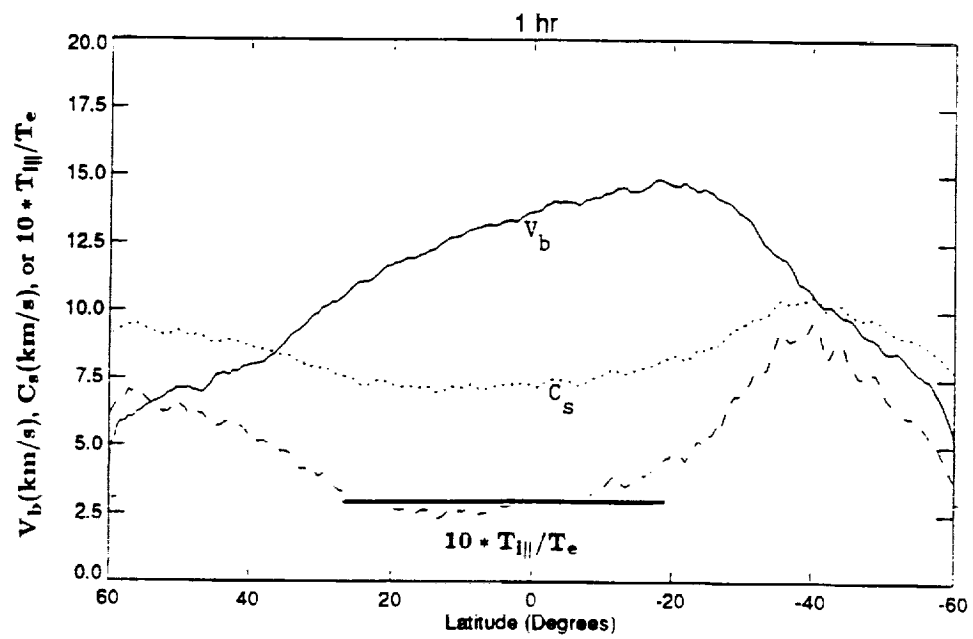


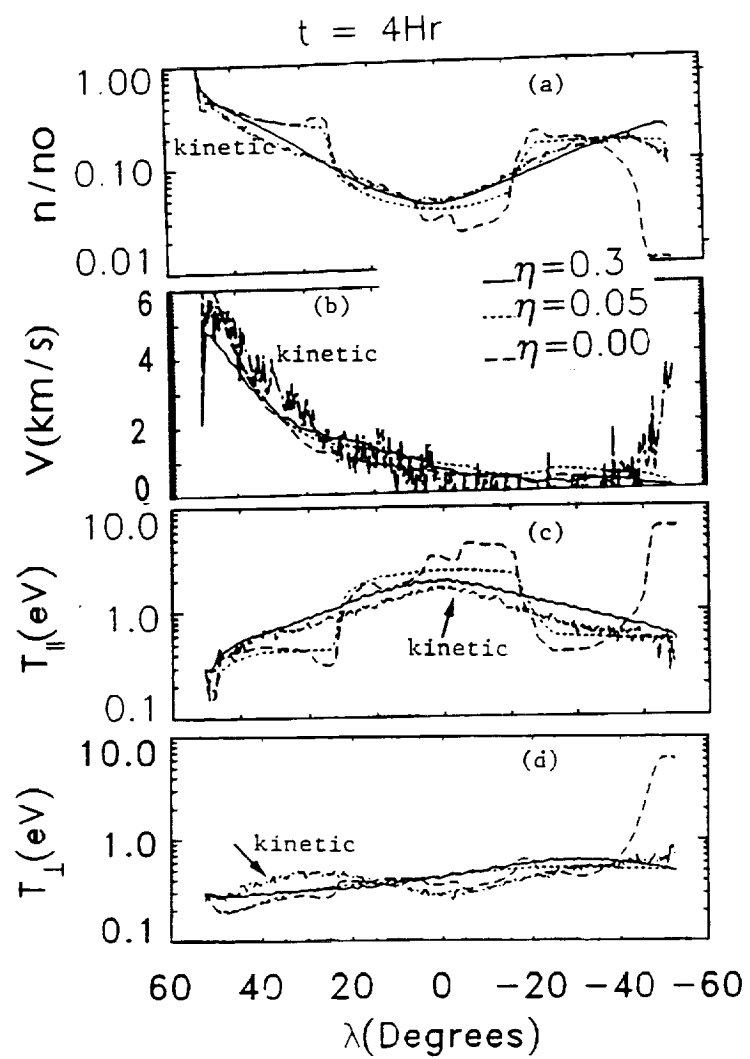
Fig. 4



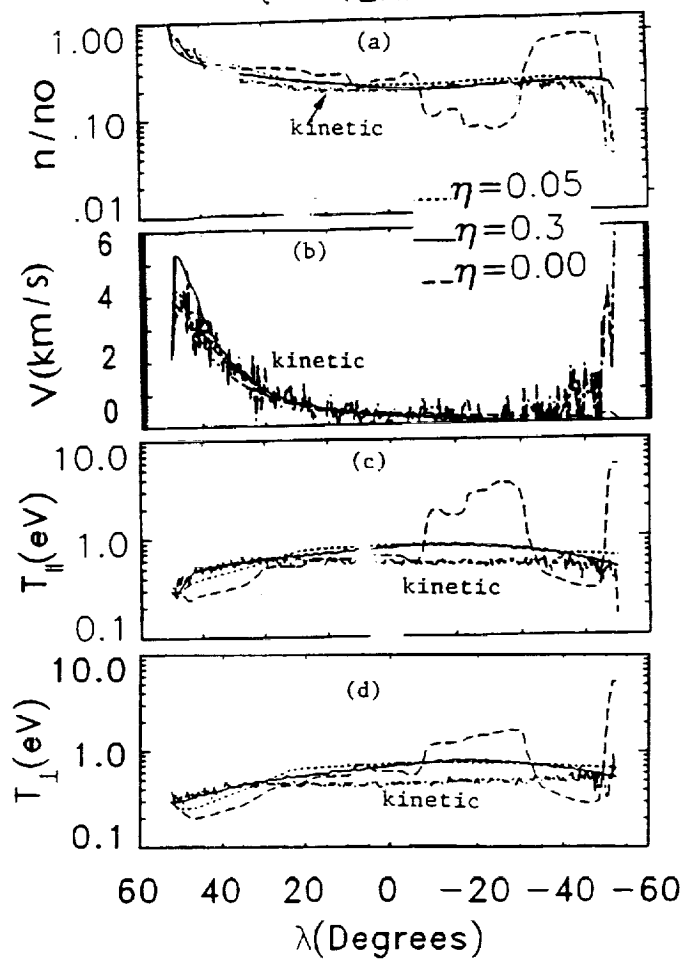


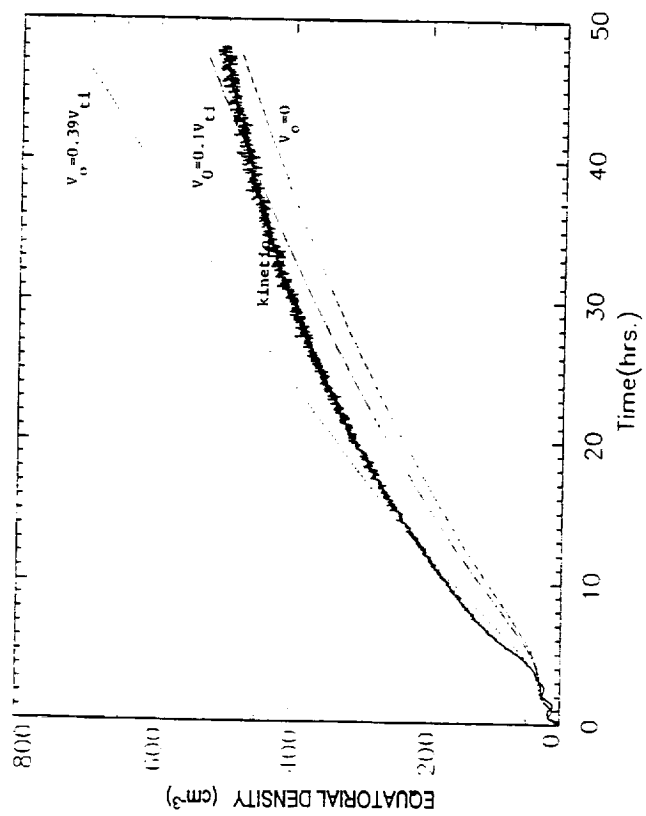


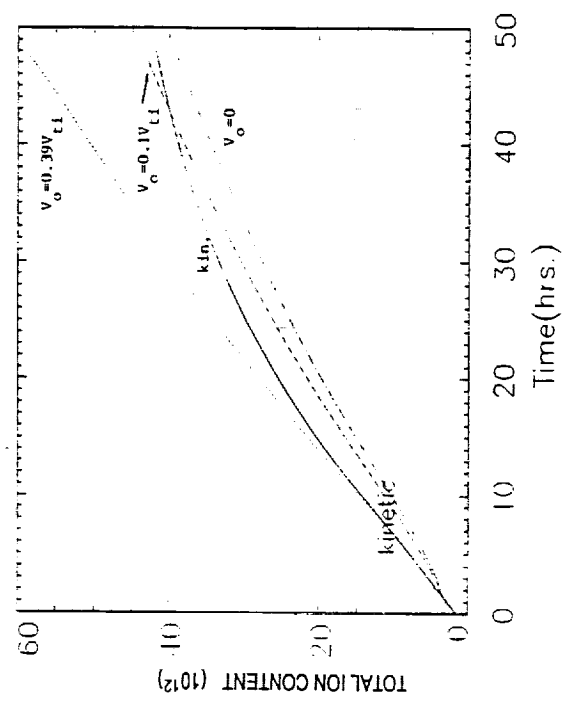




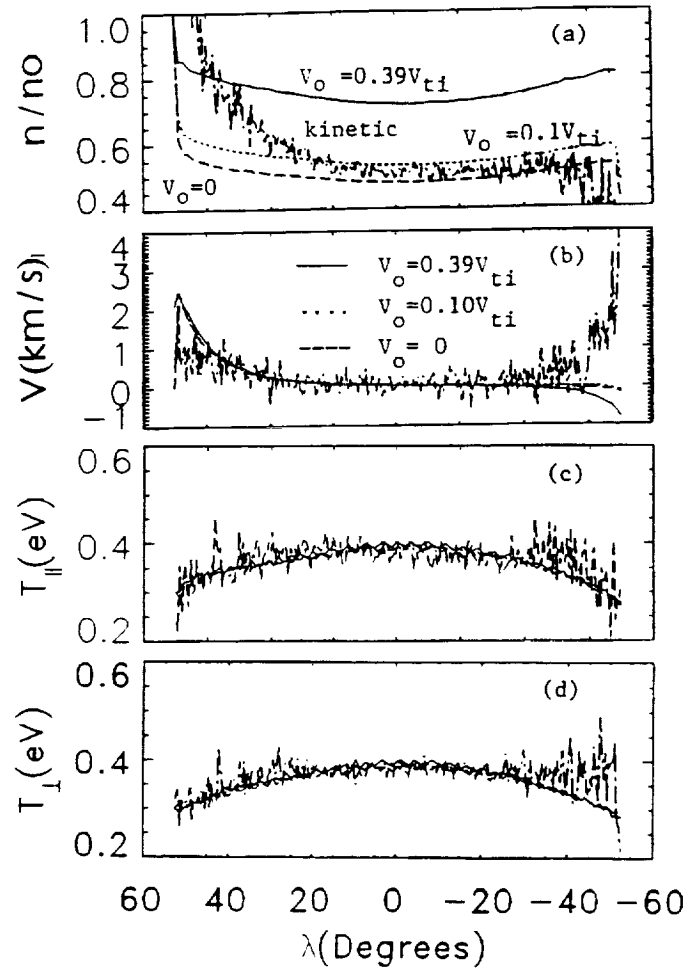
$t = 12\text{Hr}$







$t = 48\text{Hr}$





NIS

**Numerical Simulation of**  
**Filling a Magnetic Flux Tube with a Cold Plasma:**  
**(1) Role of Ion Beam-Driven Instabilities**

**Nagendra Singh and W. C. Leung**

Department of Electrical and Computer Engineering & CSPAR  
University of Alabama, Huntsville, AL 35899

Submitted to *JGR*, April 1994

## Abstract:

Large-scale models of plasmaspheric refilling have revealed that during the early stage of the refilling counterstreaming ion beams are a common feature. However, the instability of such ion beams and its effect on refilling remain unexplored. The difficulty with investigating the effect of ion-beam driven instability on refilling is that the instability and the associated processes are so small-scale that they cannot be resolved in large-scale models; typically the instabilities have scale lengths of a few tens of plasma Debye length, which is a few meters at the most, and the spatial resolution in large-scale models is at least several tens of kilometers. Correspondingly, the temporal scale of the instability is by several orders of magnitude smaller than the temporal resolution afforded by the models. In order to learn the basic effects of ion beam instabilities on refilling, we have performed numerical simulations of the refilling of an artificial magnetic flux tube. The shape and size of the tube are assumed so that the essential features of the refilling problem are kept in the simulation and at the same time the small-scale processes driven by the ion beams are sufficiently resolved. Two types of simulations have been performed; in one type we treat ion kinetically and electrons are assumed to obey the Boltzmann law. In the other type both electrons and ions are treated kinetically. A comparison between the results from such simulations reveal that in the latter type of simulations electron-ion (e-i) and ion-ion (i-i) instabilities occur and significantly modify the evolution of the plasma density distributions in the flux tube along with the total plasma content. When the electron dynamics is simplified by the assumption of the Boltzmann law, both the electron-ion and ion-ion instabilities are inhibited, and only in very late stage of the filling there is a weak scattering of ions due to an enhanced plasma fluctuation level. On the other hand, when electrons are treated kinetically, the e-i instability occurs at an early stage when ion beams are too fast to excite the i-i instability. The former instability heats the electrons so that conditions for the latter instability are eventually met. The i-i instability and its non-linear evolution creates potential structures including several electrostatic shock pairs which significantly modify the filling process. The electrostatic potential structures are highly dynamic, and at times they appear as moving double layers greatly affecting the state of the plasma inside the central region of the flux tube.

## 1. Introduction

An outstanding problem in space plasma transport is the coupling of microscale and mesoscale processes. An interesting example of this problem is the early stage refilling of the outer plasmaspheric flux tubes after geomagnetic storms. The plasma evacuation from the flux tubes for  $L > 3$  during the disturbed times creates pressure gradients between the ionosphere and the equatorial region, driving highly supersonic ion beams in the interhemispheric plasma flow. The counterstreaming ion beams should be able to drive instabilities and affect the plasma flow, and hence the refilling process.

The renewed theoretical effort on plasmaspheric refilling during the last ten years or so have been primarily on large-scale modeling using hydrodynamic [Kazanov *et al.*, 1984; Singh *et al.*, 1986; Rasmussen and Schunk, 1982; Singh, 1988, 1990, 1991a; Singh and Chan, 1992] and semikinetic [Wilson *et al.*, 1992; Lin *et al.*, 1992] treatments. The temporal and spatial resolutions afforded by the model are generally too crude to include the microscopic effects. Driven by the idea that interpenetrating ion beams may generate shocks during refilling [Banks *et al.*, 1971], the physics of shock formation has been studied using small-scale simulations [Singh and Schunk, 1983; Singh *et al.*, 1986; Singh, 1988; Singh and Chan, 1992]. More recently some anomalous effects in terms of transverse ion heating and scattering of ions have been included in the theoretical studies of the refilling problem, but these effects are not directly driven by the ion beams, instead it is hypothesized that the heating and scattering is caused by waves generated by a hot plasma trapped in the equatorial region [Singh *et al.*, 1982; Singh and Hwang, 1987; Singh and Torr, 1989; Singh, 1991b; Singh and Chan, 1992; Lin *et al.*, 1992].

The main purpose of this paper is to study the effect of ion-beam driven waves on the filling of a magnetic flux tube with plasmas flowing into it from its ends, as schematically shown in Figure 1a. Since we wish to resolve the microprocesses associated with the instability caused by the ion beams, we cannot model an entire plasmaspheric flux tube. Therefore, we perform the study by means of numerical simulations of plasma flow in an artificial flux tube, which has the essential feature of magnetic mirrors. Owing to the limited size of the flux tube included in the simulation, results presented here illustrate the basic properties of the ion-beam driven instabilities, their effects on the plasma flow and the accumulation of the plasma in the tube. These results cannot be quantitatively applied to a plasmaspheric flux tube, but the basic ideas found here are applicable and the question is raised as to how to include them in the large-scale refilling models. However, no attempt has been made to answer this question in this paper.



The basic ideas found in this paper are as follows. When the simulation is performed by treating ions kinetically and electrons by simply assuming that they obey the Boltzmann law, the ion-beam driven instabilities are not found because the beams are too fast to excite the waves. On the other hand, when electrons are also treated kinetically the fast ion beams during the early stage of the evolution of the plasma in the flux tube drive electron-ion instability [Fujita *et al.*, 1977; Singh, 1978]. This instability contributes to the heating of electrons in conjunction with the electron energization in the self-consistent potential distributions resulting from counterstreaming plasma expansion. This heating increases the ion-acoustic speed in the plasma and thereby the initially fast ion beams eventually become slow enough relative to the ion-acoustic speed to drive the ion-ion instability, which is found to be very effective in coupling counterstreaming ion beams and in trapping of plasma in the flux tube, especially in its outer regions away from the central minimum magnetic field (Figure 1b). Comparing the results from the simulations with and without the kinetic treatment of the electrons, we found that in the former simulation the filling of the flux tube is enhanced due to the trapping of plasma in the potential structures set up by the ion-ion instability. The instability also drives electrostatic shocks and distributes the plasma in the flux tube quite differently from that in the simulation with the simplified electron dynamics. Furthermore, this instability controls the influx of ions into the central region of the flux tube, and thereby the dynamics of the potential structures including the electrostatic shocks in the central region.

The rest of the paper is planned as follows: In Section 2 we describe the numerical technique. In Section 3 numerical results are described along with their interpretation. The conclusion of the paper is given in Section 4.

## 2. Numerical Model

We perform a one-dimensional particle-in-cell simulation of plasma flow along an artificial flux tube (Figure 1a). The magnetic field  $B(X) = B_0(1 - \alpha \exp[-(X - d/2)^2 / \sigma^2])$  where  $B_0$  is a constant field outside the minimum-field region (Figure 1b),  $d$  is the size of the simulation system and the choice of  $\alpha$  and  $\sigma$  determines the desired field distribution. The cold plasma flows into the flux tube from the two plasma reservoirs at the ends of the simulation system at  $X = 0$  and  $X = d$  (Figure 1a). The simulation technique is described in Singh and Chan [1992]. Plasma dynamics is simulated using a particle-in-cell (PIC) code. We have performed two types of simulations; in one type, called here Run-1, ions are treated kinetically using the PIC code while electrons are assumed to obey the Boltzmann law. This assumption along with the assumed condition of a quasineutral plasma gives the electric field  $E = -(kT_o / en_i) dn_i / dx$  where  $n_i$  is the ion density,  $k$  is the Boltzmann constant, and  $T_o$  is the electron and ion temperatures in the plasma reservoirs. In the other type of simulation, called Run-2 here, both electrons and ions are treated kinetically using the PIC code and we solve the Poisson equation for the electric field with the boundary conditions  $\phi(x=0) = \phi(x=d) = 0$ , where  $\phi(x)$  denotes the potential distribution. As the particles move in the flux tube, their magnetic moments are assumed to be conserved.

The velocity distribution function of the ions and electrons in the plasma reservoir is assumed to be Maxwellian with a temperature  $T_o$ . The reservoirs supply a continuous flux of charged particles into the flux tube through the process of plasma expansion. In the simulations reported here, we have used  $m_i / m_e = 400$ , which adequately separates the electron and ion time scales and, at the same time, allows computationally feasible runs. Numerical parameters of the simulations are as follows: system size  $d = 5 \times 10^3 \lambda_d$ , the magnetic field parameters  $\alpha = 0.9$ , and  $\sigma = 750 \lambda_d$  for which  $B(x)$  is plotted in Figure 1b, cell size  $\Delta x = 20 \lambda_d$ , and time step  $\Delta t = 0.1 \omega_{peo}^{-1}$ , where  $\lambda_d$  and  $\omega_{peo}$  are the Debye length and electron-plasma frequency in the cold plasma reservoirs, respectively. In the following discussion we have used normalized quantities defined as follows: time  $\bar{t} = t \omega_{pio}$ , distance  $\bar{X} = X / \lambda_d$ , velocity  $\bar{V} = V / V_{te}$  and electric potential  $\bar{\Phi} = e\Phi / kT_o$ , where  $V_{te} = (kT_o / m_e)^{1/2}$ ,  $\omega_{pio} = (m_e / m_i)^{1/2} \omega_{peo}$ , and  $\omega_{peo}$  is the electron plasma frequency in the plasma reservoirs and the Debye length  $\lambda_d = V_{te} / \omega_{peo}$ .

### 3. Flux Tube Filling and Ion-Beam Driven Instabilities

In this section we examine the evolution of the plasma and the potential distributions in the flux tube as seen from Run-1 and Run-2. A comparison of results from these runs reveal when and why plasma instabilities are excited and how they affect the plasma and field distributions.

Figure 2 shows the evolution of the ion phase space in  $X - V_{i||}$  plane from Run-1. Note that the velocity on the vertical axis is measured in units of the ion thermal velocity  $V_{ti} = (kT_o / m_i)^{1/2}$ . Figure 2a for  $\bar{t} = 200$  shows the expanding ion beams from the two plasma sources shown in Figure 1a. By the time  $\bar{t} = 10^3$  (Figure 2b) the counterstreaming of ion beams is set up all along the flux tube; the counterstreaming continues without a significant interaction between the beams as seen from Figures 2c and 2d for  $\bar{t} = 2000$  and 4000, respectively. The main feature of the spatial evolution of the ion beams is that they progressively slow down as they approach the opposite end of the flux tube. From the plot at  $\bar{t} = 4000$ , we also note that a few particles in the ion beams approaching the opposite ends slow down upto almost zero velocity; the number of such ions increases with time as seen from the plots at  $\bar{t} = 8000$ . This tends to slowly fill in the velocity space between the two counterstreaming ion beams in the off-central region. We find that such scattering of ions is not caused by antibipolar electric fields, which are given by the ion density gradients.

The evolution of the ion density profile in the flux tube is shown in Figure 3. After the initial stage ( $\bar{t} < 1000$ ), the density profiles are generally smooth having relatively large gradients in the control region ( $1500 < |X| < 2500$ ), and in the off-central region ( $100 < X < 1500$  and  $3500 < X < 4900$ ) the gradients are weak giving weak electric fields. The scattered particles in Figures 2d and 2e occur in the latter regions. In view of the weak antibipolar electric fields, incapable of slowing down or reflecting the beams, we suggest that the scattering occurs via some anomalous effects involving fluctuations in the plasma. Later we discuss this issue further after we have considered the flow in Run-2.

The evolution of ion phase space in  $X - V_{i||}$  plane for Run-2 is shown in Figures 4a to 4f. Note that in this figure the velocity is normalized with respect to  $V_{te}$ , in contrast to  $V_{ti}$  in Figure 2 for Run-1. A comparison of the phase-space plots in Figure 2b and Figure 4b, which are for the same time  $\bar{t} = 10^3$ , shows a significant difference in the topology of the distribution of the average flow velocity of ions in the two runs; in Run-1 with the Boltzmann electrons, the ions have relatively large velocities near  $X = X_{mid}$  creating a "bulge" in the plots. The bulge is not seen in Run-2. The bulge in Figure 2 is simply a manifestation of the magnetic field distribution  $B(X)$  (Figure 1b), which controls the density distribution and hence the potential distribution according to the Boltzmann law. The relatively sharp density gradients in the density distribution on either side of the midpoint yield relatively large electric fields, which accelerate ions coming into the central region and then decelerates them while leaving. On the other hand, in Run-2 the Poisson equation including a self-consistent treatment of the space charges does not yield a potential distribution controlled by  $B(X)$ . The potential distributions for Run-2 are shown in Figures 4g to 4l.

In Run-1 we saw only a weak scattering of the beam ions at late times ( $\bar{t} \geq 4000$ ) into the velocity region between the two counterstreaming beams outside the central region of the simulation region. In contrast, in Run-2 we find that wave-particle interactions plays a significant role in coupling and mixing the counterstreaming ion beams. This can be seen from the phase-space plots for  $\bar{t} \geq 1400$  in Figures 4c to 4f. The plot at  $\bar{t} = 1400$  shows that ion-ion instability has occurred outside the central region and it is sufficiently strong to locally couple the ion beams. The instability is more clearly manifested in the potential plots given in Figures 4g to 4l. The corresponding electron phase space plots are shown in Figures 4m to 4r. Both electron and ion phase space show formation of vortices, which evolve from the ion-ion instability driven by the counterstreaming ions. We now examine in detail why this instability is so prominent in Run-2, but not in Run-1.

**Ion-Ion Instability:** The conditions for the ion-ion instability in a plasma having counterstreaming ion beams depends on a number of parameters of the beam-plasma system: these parameters are the relative beam velocity  $V_{br}$  between the two beams, the ratios of the beam temperatures  $T_{b1}$  and  $T_{b2}$  to the electron temperature  $T_e$ , and the relative densities of the ion beams  $n_{b1}/n_{b2}$  [Fried and Wong, 1986]. The relative velocity and the temperature ratios  $T_{b1}/T_e$  and  $T_{b2}/T_e$  play crucial roles in determining whether the instability occurs or not.

For two symmetric counterstreaming ion beams, i.e.,  $V_{br} = 2V_b$ , where  $\pm V_b$  are the two beam velocities, and  $T_{b1} = T_{b2} = T_i$ , the instability occurs when [McKee, 1970]

$$1.3V_{ti} \leq V_b \leq C_s \quad \text{and} \quad T_e > 3T_i \quad (1)$$

where  $C_s$  is the ion-acoustic speed given by  $C_s = (k(T_e + 3T_i)/m_i)^{1/2}$  and  $V_{ti} = (kT_i/m_i)^{1/2}$ .

For non-symmetric beams it is not possible to give analytical conditions as above for the symmetric ones. However, some qualitative assessments can be made; if one of the beams is warmer than the other, say  $T_{b1} > T_{b2}$ , instability occurs as long as the velocity condition in equation (1) is met and  $T_e/T_{b1} > 3$  [Baker, 1973; Gresillon and Doveil, 1975; Singh, 1978]. However, Fried and Wong [1966] have shown that when one of the beams is sufficiently cold depending on the relative beam density, the instability can occur even if the warm beam satisfies the condition  $T_{b1}/T_e = 1$ .

Now we examine if the instability conditions described above are met in our simulations. Figure 5 shows examples of ion velocity distribution function from Run-1; the distributions shown here are from the off-central region  $4000 \leq \bar{X} \leq 4500$ , where relatively slow ion beams are more likely to meet the condition for the ion-ion instability. Note that in this figure the horizontal scale is the ion velocity normalized with respect to the thermal velocity  $V_{ti} = (kT_o/m_i)^{1/2}$ . The distributions shown in Figure 5 are for (a)  $\bar{t} = 4000$ , (b)  $\bar{t} = 6000$ , and (c)  $\bar{t} = 8000$ ; we noticed earlier from Figure 2 that at such late times the beam ions weakly scatter to fill in the velocity space between the two ion beams in the off-central region.

The instability conditions discussed above are for a Maxwellian velocity distribution, but we note from Figure 5 that the distributions are not Maxwellian. However, effective beam velocities and temperatures as first and second order moments of the individual ion beams can be calculated, and they are given in Table 1. Note that the velocities given in this table are normalized with respect to  $V_{ti}$ . The ion beams for  $V_{||} < 0$  and  $V_{||} > 0$  are called beam-1 and beam-2, respectively. The relative beam velocity  $V_{br} = V_{b2} - V_{b1}$  and the ion-acoustic speed are also tabulated. We find from Table 1 that the beam temperatures do satisfy the condition for the instability given by equation (1). However, the relative beam velocity is too large to excite the instability, that is,  $V_{br} > 2C_s$ ; thus the ion-ion instability, as predicted from the linear instability analysis for Maxwellian ion beams, should not occur. However, as noted earlier, the beams are not Maxwellian; the fall of the distribution functions at velocities below their respective peak velocities is quite sharp and the peak separation in velocity progressively decreases from  $\Delta\bar{V} = 3.1$  at  $\bar{t} = 4000$  to  $\Delta\bar{V} = 2.6$  at  $\bar{t} = 8000$ . Taking  $\Delta\bar{V}$  as  $V_{br}$  we find that the instability condition on velocity is marginally satisfied at  $\bar{t} = 8000$ . The approach towards the marginal instability causes an enhanced fluctuation in the plasma (e.g., see Ichimaru [1973]) and the consequent scattering of ions in velocity space as mentioned earlier. Figure 6 shows evolution of the density fluctuations at  $\bar{X} = 1500, 1000$ , and  $500$ ; we note from this figure that with the decreasing distance from the end of the flux tube, the amplitude of the density fluctuation increases and therefore the fluctuations in the electric field also increases. The fluctuation in the electric field scatters the ions, populating the velocity region between the ion beams. The scattered ions appear as a "tail" to the velocity distribution function near  $V = 0$  as seen from Figure 5c. In the central region of the flux tube, where the ion beams are quite fast and far from the marginal instability condition, the fluctuations in the density and the electric fields are weak and scattering of ions is not seen (see Figure 2e).

Table 1. Ion beam parameters from Run-1.

$\bar{t}$	$\bar{n}_{b1}$	$\bar{n}_{b2}$	$\bar{V}_{b1}$	$\bar{V}_{b2}$	$\bar{V}_{br}$	$\bar{T}_{b1}$	$\bar{T}_{b2}$	$T_e$	$C_s$
4000	0.55	0.45	-1.60	1.85	3.45	0.16	0.18	1	1.22
6000	0.52	0.48	-1.58	1.60	3.18	0.2	0.23	1	1.30
8000	0.51	0.49	-1.51	1.51	3.00	0.21	0.27	1	1.31

The evolution of the ion and electron velocity distribution functions from Run-2 are shown in Figure 7; Figures 7a, 7b and 7c show the ion distribution functions at  $\bar{t} = 1000, 1200$  and  $1400$ , respectively, and the corresponding electron distribution functions are shown in Figures 7d, 7e and 7f. The distributions shown in these figures are for the plasma in the region  $4000 < \bar{X} \leq 4500$  and for times just before the onset of the ion-ion instability leading to the formation of vortices in Figure 4. Table 2 shows the ion beam and plasma parameters relevant for the linear instability analysis. The ion beams denoted by subscripts "1" and "2" are for  $V_{\parallel} < 0$  and  $V_{\parallel} > 0$ , respectively. All velocities given in this table are normalized with respect to  $V_{te}$ . Comparing  $V_{br}$  and  $C_s$  in the table, we find that by the time  $\bar{t} = 1400$ , the velocity condition on the instability is met, i.e.,  $V_{br} \leq 2C_s$ . We note that the temperature condition for the i-i instability is also satisfied because  $T_{b1}/T_e = 0.13$  and  $T_{b2}/T_e = 0.3$ . Thus, the instability occurs as manifested by the ion and electron phase-space plots, and the potential distribution in Figure 4 for times  $t \geq 1400$ .

**Table 2. Ion beam and plasma parameters from Run-2.**

$\bar{t}$	$\bar{n}_{b1}$	$\bar{n}_{b2}$	$\bar{V}_{b1}$	$\bar{V}_{b2}$	$\bar{V}_{br}$	$\bar{T}_{b1}$	$\bar{T}_{b2}$	$T_e$	$C_s$
1000	0.93	0.07	-0.1	0.22	0.32	0.32	0.58	2.6	0.1
1200	0.87	0.13	-0.096	0.19	0.28	0.37	0.74	2.8	0.1
1400	0.82	0.18	-0.086	0.16	0.21	0.42	1.00	3.1	0.12

**Electron-Ion Instability:** It is noteworthy that in Run-2 electron heating is the key for fulfilling the instability condition by increasing the ion-acoustic speed; Table 2 shows that the electrons are heated to an effective temperature of  $3.1 T_o$  by  $\bar{t} = 1400$ . How are the electrons heated? We discuss here the mechanism for the electron heating.

In an ion beam-plasma system, e-i instability is yet another mechanism for exciting waves, which heats the electrons [McKee, 1970]. The e-i instability occurs when the ion beams are relatively fast [Fujita *et al.*, 1977; Singh, 1978]. This instability is kinetic and it occurs as the slow (negative energy) wave of an ion beam undergoes Landau damping by the electrons [Hasegawa, 1975; Singh 1978]. Such an instability creates density fluctuation at frequencies less than the ion plasma frequency. In order to demonstrate that this instability does occur in Run-2, we show in Figure 8a and 8b the evolution of the plasma and the potential by plotting  $\bar{n}_e(t)$ ,  $\bar{n}_i(t)$  and  $\bar{\phi}(t)$  at  $\bar{X} = 2500$ . Figure 8a shows the evolution of the electron and ion densities. For  $\bar{t} < 200$ , the central region is nearly unpopulated with a plasma because the expanding plasmas from the sources at the end of the flux tube have not yet reached there. From  $\bar{t} \sim 200$  to  $\bar{t} \sim 400$ , the central region is electron rich, and when  $\bar{t} > 400$  the central region acquires a quasineutral plasma with  $n_e \cong n_i$ . The plasma density builds up to  $\sim 10^{-2} n_o$  by  $\bar{t} = 1000$ .

The electric potential shown in Figure 8b is expected to slowly evolve with the plasma build up in response to the counterstreaming plasma expansion into the flux tube. This slow evolution is shown by a dotted-line curve, which is the potential averaged over a time interval  $\Delta \bar{t} = 100$ . The fluctuations superimposed on this curve, as shown by the solid-line curve, are relevant to our discussion here. The frequency spectrum of the potential variation in Figure 8b is shown in Figure 8c. We notice that there is a broad peak in the frequency range  $0.01 \leq f/f_{pio} \leq 0.1$ , where  $f_{pio}$  is the ion plasma frequency in the source plasmas. For the time period of simulation shown in Figure 8, the local plasma density at  $\bar{X} = 2500$  is  $\bar{n} < 10^{-2} n_o$ , and hence the local ion plasma frequency  $f_{pi} < 0.1 f_{pio}$ . Thus the low frequency oscillations are bounded by this local plasma

frequency. These low frequency fluctuations which have amplitudes upto  $4 kT_o / e$ , heat the electrons to a temperature of upto  $3 T_o$  as shown in Table 2.

Another mechanism which contributes to the electron energization deals with the spatial distribution of the slowly time-varying potential as shown in Figure 4g. When the electrons expanding from the plasma sources cross the midpoint of the simulation region, they see an accelerating potential. A signature of such acceleration is the elongated tail of the electron velocity distribution function for  $V_{||} > 0$  at  $\bar{t} = 1000$  shown in Figure 7d.

**Consequences of the Ion-Ion Instability:** The plasma flow and the potential distribution in the flux tube are significantly affected by the ion-ion instability as seen from Figures 4a to 4r. The instability occurs in the off-central region and in the central region the ion beams continue to counterstream (Figures 4d to 4f). At an early stage, the instability occurs at relatively small scale lengths as seen from the potential distribution in Figure 4i. The subsequent nonlinear evolution of the instability forms vortices, which grow in size as clearly seen from the potential distributions for  $\bar{t} \geq 1600$  in Figures 4j, 4k and 4l. The amplitudes of the potential associated with the vortices are as large as  $5 kT_o / e$ , which approximately corresponds to the ion beam energy at  $\bar{t} = 1400$  when the instability sets in, that is,

$$\frac{1}{2} m_i V_{b2}^2 \cong q \Delta\phi$$

where  $\Delta\phi$  is the amplitude of a vortex and  $V_{b2}$  is the beam velocity of the faster ion beam. The above relationship between  $V_{b2}$  and  $\Delta\phi$  suggests the possibility of trapping the ions in the vortices. This trapping is evident from Figure 4. The cells with relatively high positive potentials have ions almost completely mixed in velocity space and their velocity spread is reduced in contrast to the relatively large velocity spread in the neighboring negative potential cells. As a matter of fact in the latter cells ions have a "hole" in their velocity distribution function, which is a signature of an ion hole. The electrons' behavior is directly opposite to that of the ions; electrons have large velocity spreads in the positive potential cells and a relatively small spread in the negative potential cells (see Figures 4p, 4q and 4r). This alternate trapping of electrons and ions affects the flow of plasma and density distribution in the flux tube. Before we discuss the density distribution and the filling of the flux tube, we point out that another consequence of the ion-ion instability is the formation of electrostatic shock-like structures.

**Electrostatic Shocks:** The electrostatic shock-like structures evolve from the ion-ion instability; the vortices having positive potential cells begin to grow in size with increasing time and their edges steepen into shock pairs. The potential distribution plots for  $\bar{t} > 1400$  show examples of the formation of some shock pairs as indicated by arrows in Figures 4j, 4k and 4l. Inside a shock pair the potential is positive; ions are mixed and electrons are trapped showing their acceleration above the background electrons. The growing size of a positive potential cell is equivalent to the motions of the shocks bounding the cell. This can be seen by comparing the innermost shock pairs on the right-hand side of the center of the simulation region in Figures 4k and 4l. The motion of shocks enables the positive potential cells to merge together. This elevates the potential of the outer region of the flux tube with respect to its ends, as well as with respect to the central region where the potential is negative in a relatively extended region.

We see from Figures 4d to 4f and 4j to 4l that as the innermost shocks bordering the central counterstreaming move inward, the size of the central counterstreaming region decreases. However, this does not continue indefinitely. The evolutions of the ion and electron phase space and that of the potential distribution, for times later than that shown in Figure 4, are given in Figure 9. Figures 9a to 9c for the ion phase space and the corresponding potential distribution in Figures 9g to 9i show that for  $\bar{t} \geq 2200$ , the central region of ion counterstreaming expands again as the innermost shocks move outward. The corresponding electron phase space plots in Figures 9m to 9r show that in the central negative potential region the electrons' velocity spread shrinks. Why do the innermost shocks move outward again? The answer to this question lies in the change in the plasma influx into the tube caused by the elevation of the positive potential in its outer regions due to the merging of the positive potential cells as shown in Figures 4k and 4l. The elevated potential chokes the plasma flow into the flux tube. When the ion flux is reduced, the inner shocks begin to move outward to maintain the continuity of the ion flux through the shocks. This phenomenon of shock motion is quite similar to the motion of double layers seen in numerical simulations [Singh and Schunk, 1982] and laboratory experiments [Iizuka et al, 1983]; in these studies

it was found that when ion flux to an existing double layer is reduced, the double layer remains stable in its shape, but it moves toward the ion source to keep the ion flux through the double layer at a constant value. The shock and the double layer are both electrostatic structures and it appears that the shock also remains stable in response to the changes in the ion flux by moving in an appropriate direction. For the outward shock motion of the shock in Figure 9g to 9j, the shock velocity is found to be  $V_{sh} \cong V_{ti}$  from  $\bar{t} = 2200$  to 2800. At later times the i-i instability again inflicts the counterstreaming ion beam as seen from the plots for  $\bar{t} > 2800$  in Figure 9. This mixes the ion beams in the outer region of the counterstreaming, but leaving the ions counterstreaming in the central region. It appears that the above process of i-i instability in the outer region, formation of positive potential cells and their merging, shock formations and their motion may repeat a few times before the flux tube fills with a thermalized plasma.

The formation of shocks in the off-equatorial region is predicted by two-stream hydrodynamic models [Rasmussen and Schunk, 1988; Singh, 1990]. But these shocks form due to the slowing down of the ion beams by polarization electric fields and/or Coulomb collisions. A semikinetic model of interhemispheric plasma flow does not show shock formation [Wilson *et al.*, 1992]. Recently Singh *et al.*, [1994] found that in a semikinetic model, which treats electrons by assuming a Boltzmann distribution, the condition on the electron to ion temperature for the ion-ion instability is not met. Our small-scale simulation discussed here show that temperature conditions can be satisfied by the electron heating due to the electron-ion instability which is driven by relatively fast ion beams and occurs during the early stage of the refilling. When electron dynamics is simplified by assuming the Boltzmann law, this instability is lost along with the associated consequences of electron heating, ion-ion instability and shock formation.

It is important to point out that dynamics of the shocks seen in two-stream hydrodynamic models is quite different from that seen in Run-2. In the former case a shock forms in each stream in the off-equatorial region and subsequently it moves upward to the equator and then downward to the ionospheric boundary. Such shock motions affect the transition from supersonic to subsonic flow for each plasma stream [Singh, 1991a]. The resulting subsonic flows continue to counterstream indefinitely. On the other hand, Run-2 shows that the counterstreaming in the off-equatorial region is rather quickly thermalized by the ion-ion instability and it persists over a longer time only in the central region. However, as seen from Figures 4 and 9 the spatial extent of the central counterstreaming is quite dynamic. Furthermore, we find that the i-i instability should lead to the formation of several shock pairs evolving from the positive potential cells created by the instability. The evolution and merging of such shock pairs has a profound effect on the state of the plasma in the central (equatorial) region.

**Flux Tube Filling:** The ion-ion instability and its nonlinear evolution affect the filling of the flux tube in several ways, which we discuss here. Figures 10a and 10b show the comparison of the ion density distributions from Run-1 and Run-2 at  $\bar{t} = 2000$  and 3600, respectively. Figure 10a shows that compared to Run-1, in Run-2 the filling is depressed in the central region while it is enhanced in the off-central region at  $\bar{t} = 2000$ . The explanation for this feature of the filling lies in the potential distribution as shown in Figures 4j to 4l. The elevated potentials in the off-central region inhibit the flow of plasma into the central region; this keeps the ion density depressed there and therefore the plasma entering the flux tube accumulates in the outer regions of the flux tube. We find that until about  $\bar{t} = 2000$  the net plasma contents of the flux tube in Run-1 and Run-2 are approximately the same. This is seen from Figure 11, in which the total number of computer ions accumulated in the flux tube is plotted as a function of time for the two runs.

Figure 10b shows that eventually the ion densities in the central region of the flux tube in the two runs become nearly equal. This is due to the fact that the potential barriers for the ions in the outer region of the flux tube reduces as seen by comparing the potential distributions in Figures 4j, 4k and 4l for  $\bar{t} < 2000$  with those in Figures 9g to 9l for  $\bar{t} > 2000$ . However, the densities in the off-central region in Run-2 remains generally larger than that in Run-1. This yields a larger plasma content in the former run than that in the latter. Figure 11 clearly shows this for  $\bar{t} > 2000$ . The enhanced refilling in Run-2 is attributed to the trapping of ions and electrons in the vortices set up by the ion-ion instability.

#### 4. Conclusions and Discussion

The main conclusions of this paper are the following:

1. As the magnetic flux tube fills with a plasma expanding from plasma sources located at its end, the ion-beams driven instabilities significantly affect (a) the distribution and dynamics of the plasma in the tube, and (b) the accumulation of plasma in it.
2. Two types of instabilities are found to occur: the instability caused by electron-ion interaction is kinetic in nature and occurs when the ion beams are relatively fast, and electron dynamics is not simplified by the assumption of the Boltzmann law. The ion-ion instability occurs for comparatively slower ion beams.
3. In the simulation with the Boltzmann electron, the electron-ion instability is suppressed and the ion beams remain too fast with respect to the ion-acoustic speed to excite ion-ion waves. However, as the beams slow down by the filling of the flux tube, they tend toward the marginal instability, especially in the outer region of the flux tube, where the plasma fluctuation is enhanced. This causes an anomalous scattering of the beam ions in the outer region.
4. In simulation with the kinetic treatment of the electrons, e-i instability occurs when the beams are relatively fast and it heats the electrons. In addition, some electron energization occurs when they are accelerated by the inward pointing electric fields set up by the counterstreaming plasma expansion. When electrons are sufficiently heated, increasing the ion-acoustic speed so that  $V_{br} \leq 2C_s$ , the ion-ion instability occurs.
5. The ion-ion instability is effective in coupling the counterstreaming ion beams in the region where instability conditions are met. This sets up potential structures including electrostatic shocks. The central counterstreaming is seen to spatially shrink and expand as the ion-ion instability and its nonlinear features affecting the plasma evolve.
6. The trapping of plasma in the potential structures enhances the flux tube refilling and affects the distribution of the plasma in it.
7. In the central region of the flux tube where the magnetic field is minimum, the fast ion beams continue to counterstream over a relatively long time.

Following the work of *Banks et al* [1971], now there are several studies on shock formation including large-scale hydrodynamic [*Singh et al*, 1986; *Guter and Gombosi*, 1991; *Rasmussen and Schunk*, 1988] and kinetic models [*Wilson et al*, 19992; *Singh et al*, 1994] and small-scale simulations [*Singh et al*, 1986; *Singh*, 1988]. The usual picture emerging from such studies is the formation of a pair of shocks in the equatorial region or in the off-equatorial region, one in each hemisphere. The simulation presented here suggests that when i-i instability occurs, it may create numerous shock pairs in the off-equatorial region. Their merging and dynamics may introduce both spatial structures in the plasma distribution and temporal features in the evolution of the plasma state, both in the equatorial and off-equatorial regions.

In view of the above results, a pertinent question is whether they are relevant to the refilling of plasmaspheric flux tube. Since the ion beams are inherent to the early stage refilling, the answer to this question is solidly yes. In view of the crudeness in the temporal and spatial resolution of the large-scale refilling models, the most pertinent question is how to include the effects of the instability in such models. At this juncture the answer to this question is not very clear, but we know that it must be done by calculating anomalous plasma transport coefficients which can be included in the large-scale treatments. The heating of electrons and ions by the instability can be included through an anomalous collision frequency like that for ion-cyclotron instability in the auroral plasma [*Ganguli and Palmadesso*, 1987], but how to include the effect of ion and electron trapping in potential structures set up by the ion-ion instability remains a challenge.

**Acknowledgment:** This work was supported by NASA grant NAGW-2128 made to the University of Alabama in Huntsville.

## References

- Banks, P. M., A. F. Nagy, and W. I. Axford, Dynamical behavior of thermal protons in the mid-latitude ionosphere and magnetosphere, *Planet. Space Sci.*, 19, 1053, 1971.
- Baker, D. R., Nonlinear development of the two ion beam instability, *Phys. Fluids*, 1730, 1973.
- Forslund, D. W., and C. R. Shonk, Formation of electrostatic collisionless shocks, *Phys. Rev. Lett.*, 25, 1699, 1970.
- Fried, B. D., and A. Y. Wong, Stability limits for longitudinal waves in ion-beam-plasma interactions, *Phys. Fluids*, 9, 1084, 1966.
- Fujita, T., T. Ohnuma and S. Adachi, Self-oscillations excited by two stream ion-ion instability, *Plasma Phys.*, 19, 875, 1977.
- Ganguli, S. B., and P. J. Palmadesso, Plasma transport in the auroral return current region, *J. Geophys. Res.*, 92, 8673, 1987.
- Gresillon, D., and F. Doveil, Normal modes in the ion-beam-plasma system, *Phys. Rev. Lett.*, 34, 77, 1975.
- Guiter, S. M., and T. I. Gombosi, The role of high-speed plasma flows in plasmaspheric refilling, *J. Geophys. Res.*, 95, 10,427, 1990.
- Hasegawa, A., *Plasma Instability and Nonlinear Effects*, Springer-Verlag, Berlin, Chapter 4, p. 160, 1975.
- Ichimaru, S., *Basics of Plasma Physics*, The Benjamin-Cummings Publishing Company, Inc, Reading, MA, Chapt. 11, 1973.
- Iizuka, S., P. Michelsen, J. J. Rasmussen, R. Schritwieser, R. Hatakeyama, K. Saeki, and N. Sato, Double layer dynamics in a collisionless magnetoplasma, *RISO -M-2414*, 1983.
- Khazanov, G. V., M. A. Kuen, Yu V. Konikov, and I. M. Sidorov, Simulation of ionosphere-plasmasphere coupling taking into account ion inertia and temperature anisotropy, *Planet. Space Sci.*, 32, 585, 1984.
- Lin, J., J. L. Horwitz, G. R. Wilson, C. W. Ho, and D. G. Brown, A semikinetic model for early stage refilling: 2. Effects of wave-particle interactions, *J. Geophys. Res.*, 97, 1121, 1992.
- McKee, C. F., Simulation of counterstreaming plasmas with application to collisionless electrostatic shocks, *Phys. Rev. Lett.*, 18, 990, 1970.
- Rasmussen, C. E., and R. W. Schunk, Multistream hydrodynamic modeling of interhemispheric plasma flow, *J. Geophys. Res.*, 93, 14,557, 1988.
- Singh, N., Comment on "Multistream hydrodynamic modeling of interhemispheric plasma flow, by C. E. Rasmussen and R. W. Schunk, *J. Geophys. Res.*, 95, 17, 272, 1990.
- Singh, N., Ion-Electron instability of ion-beam-plasma systems, *Physics Letters*, 67A, p. 372, 1978.
- Singh, N., Role of ion temperature anisotropy in multistage refilling of the outer plasmasphere, *Geophys. Res. Lett.*, 18, 817-820, 1991a.
- Singh, N., Role of electromagnetic noise in the interhemispheric plasma exchange along closed field lines, *Advances in Space Res.*, 11, 9 pp. (9)51-(9)54, 1991b.



- Singh, N., Refilling of a plasmaspheric flux tube: Microscopic plasma processes, in modeling magnetospheric plasma, ed. T. E. Moore and H. H. Waite, *Geophys. Monograph*, 44, Amer. Geophys. Union, Washington, DC., 87, 1988..
- Singh, N., and C. B. Chan, Effects of equatorially trapped ions on refilling of the plasmasphere, *J. Geophys. Res.*, 97, 1167, 1992.
- Singh, N., and K.S. Hwang, Perpendicular ion heating effects on the refilling of the outer plasmasphere, *J. Geophys. Res.*, 92, 13513, 1987.
- Singh, N., W. J. Raitt and F. Yasuhara, Low energy ion distribution functions on a magnetically quiet day at geostationary altitude ( $L=7$ ), *J. Geophys. Res.*, 87, 681, 1982.
- Singh, N., and R. W. Schunk, Dynamical features of moving double layers, *J. Geophys. Res.*, 87, 3561, 1982.
- Singh, N., and R. W. Schunk, Numerical simulations of counterstreaming plasmas and their relevance to interhemispheric flow, *J. Geophys. Res.*, 88, 7867, 1983.
- Singh, N., R. W. Schunk, and H. Thiemann, Temporal features of the refilling of a plasmaspheric flux tube, *J. Geophys. Res.*, 91, 13433, 1986.
- Singh, N., and D. G. Torr, Effects of ion temperature anisotropy on the interhemispheric plasma transport during plasmaspheric refilling, *Geophys. Res. Lett.*, 17, 925, 1990.
- Singh, N., G. R. Wilson, J. L. Horwitz, Comparison of hydrodynamic and semikinetic treatments for a plasma flow along closed field lines, *J. Geophys. Res.*, in press, 1994.
- Wilson, G. R., J. L. Horwitz, and J. Lin, A semikinetic model for early stage plasmasphere refilling, 1, Effects of Coulomb collisions, *J. Geophys. Res.*, 97, 1189, 1992.

## FIGURE CAPTIONS

**Figure 1.** (a) Geometry of the simulation; the magnetic flux tube and the two plasma reservoirs at the ends of the tube are shown. The flux tube fills with plasma when the plasmas from the reservoirs expand into it. (b) Magnetic field distribution in the flux tube; the mirror ratio is 10.

**Figure 2.** Evolution of ion phase-space in  $X - V_{||}$  plane from Run-1.

**Figure 3.** Plasma density distributions at some selected times from Run-1.

**Figure 4.** (a) to (f) Evolution of ion phase-space in the  $X - V_{||}$  plane from Run-2. Note the coupling between the ion beams due to ion-ion instability for  $\bar{t} \geq 1400$ . (g) to (l) Potential distribution corresponding to the phase-space evolution in Figures 4a to 4f. The arrows in panels j, k and l show the evolution of the shock pairs from the positive potential cells created by the ion-ion instability. (m) to (r) Evolution of electron phase-space in the  $X - V_{||}$  plane.

**Figure 5.** Ion parallel velocity distribution functions from Run-1 at some selected times in the region  $4000 \leq \bar{X} \leq 4500$ , where scattered ions were seen for  $\bar{t} \geq 4000$ .

**Figure 6.** Temporal evolution of density fluctuations at (a)  $\bar{X} = 500$ , (b)  $\bar{X} = 1000$  and (c)  $\bar{X} = 1500$ . Note the increase in the fluctuation amplitude with decreasing  $\bar{X}$ .

**Figure 7.** Ion parallel velocity distribution functions at times (a)  $\bar{t} = 1000$ , (b)  $\bar{t} = 1200$  and (c)  $\bar{t} = 1400$ . The distributions are for the ions in the region  $4000 \leq \bar{X} \leq 4500$ . The corresponding electron distributions are shown in (d)  $\bar{t} = 1000$ , (e)  $\bar{t} = 1200$  and (f)  $\bar{t} = 1400$ .

**Figure 8.** Temporal evolution of (a) Electron and ion densities. (b) Electric potential  $\bar{\phi}$ , all at  $\bar{X} = 2500$ . (c) Frequency spectrum of the potential shown in (b). The dotted curve in (b) shows the average potential when the fluctuations are averaged out.

**Figure 9.** Same as Figure 4, but the plots are for  $\bar{t} > 2000$ . Note the temporal variation in the spatial extent of the central counterstreaming and the associated charges in the potential distribution.

**Figure 10.** Comparison of the density distributions in the flux tube from Run-1 and Run-2 at (a)  $\bar{t} = 2000$  and (b)  $\bar{t} = 3600$ .

**Figure 11.** Comparison of the flux tube contents from Run-1 and Run-2. Note the enhanced filling in Run-2.

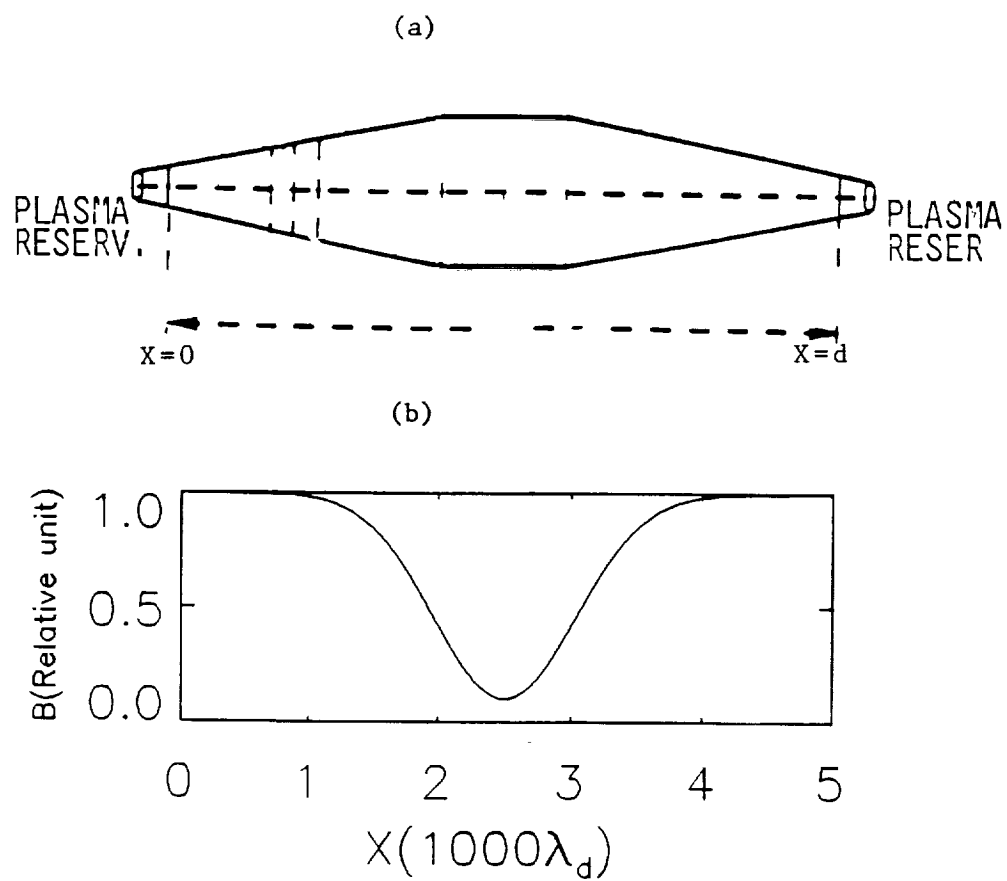


Fig. 1

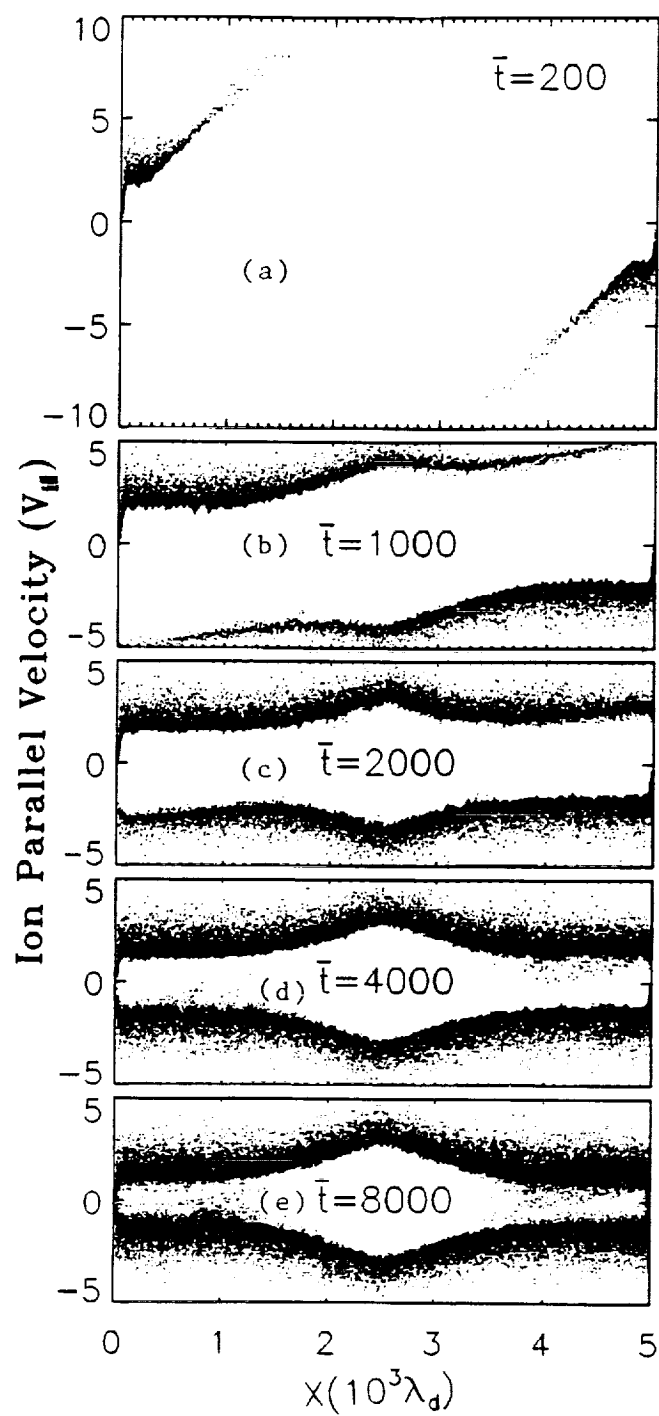


Fig. 2

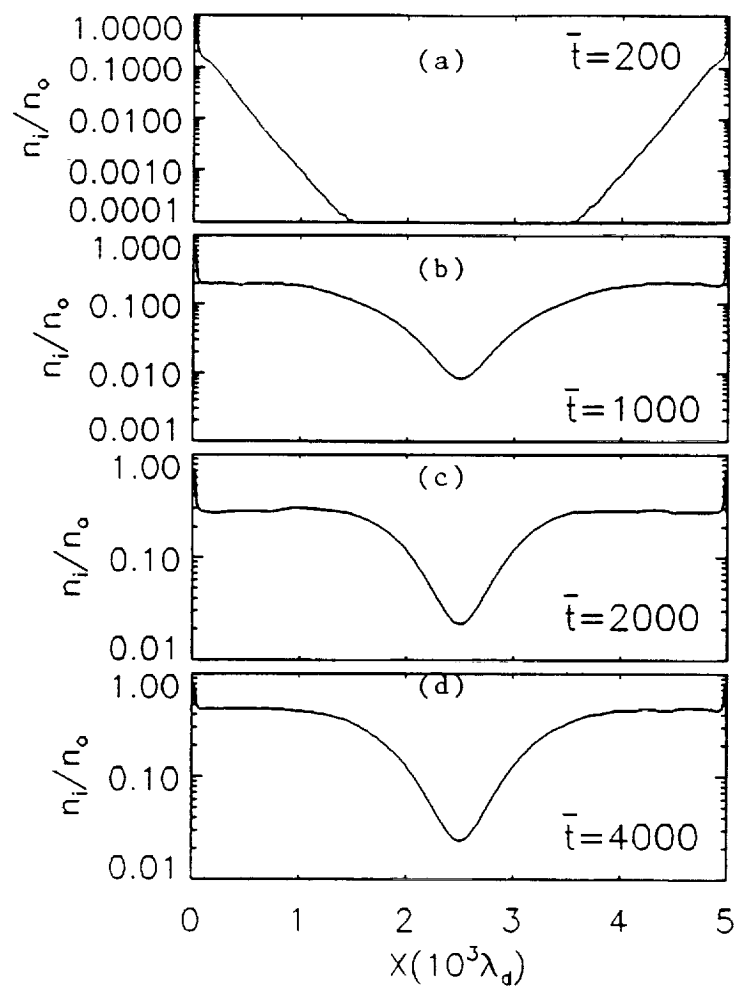


Fig. 3

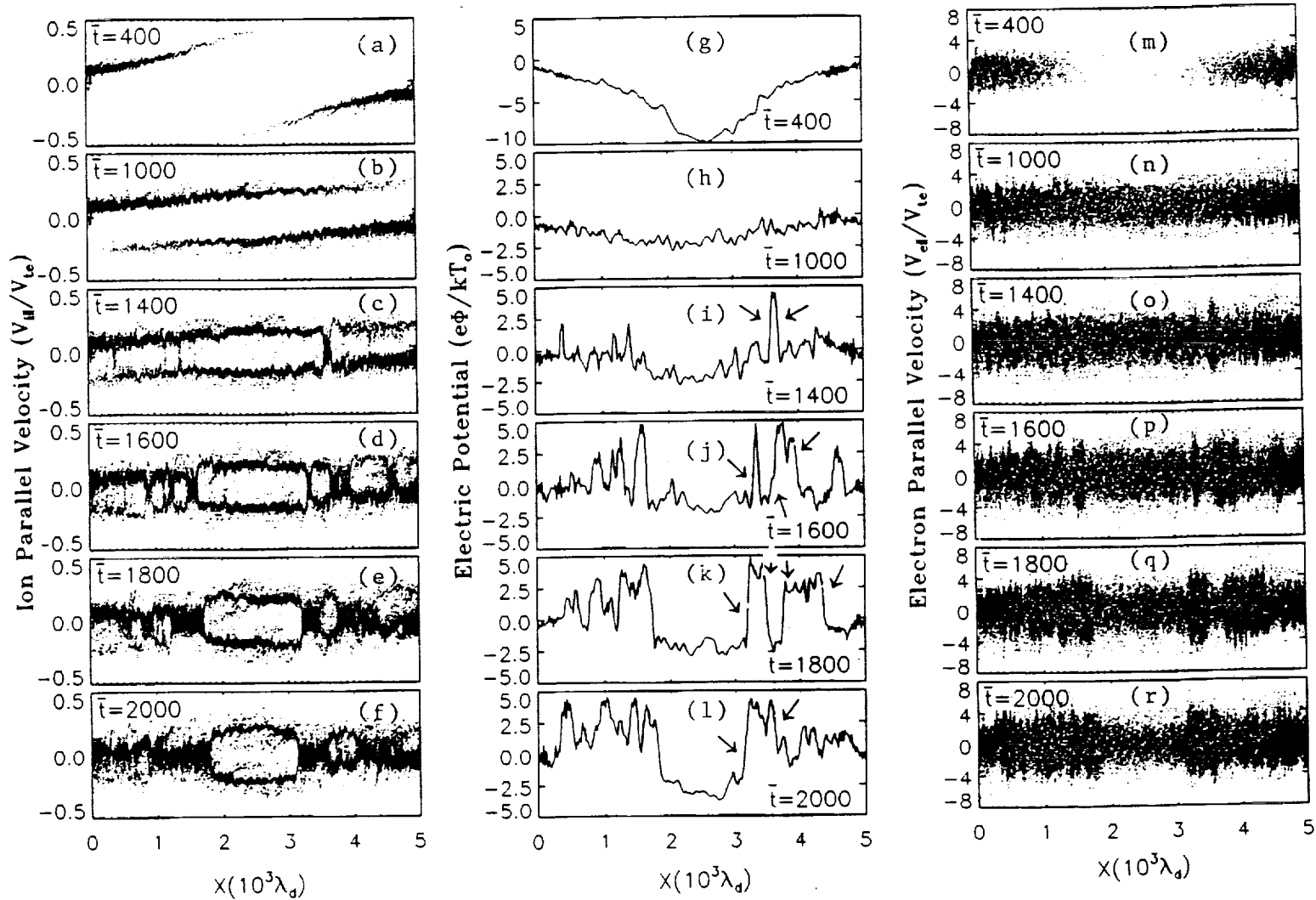


Fig. 4

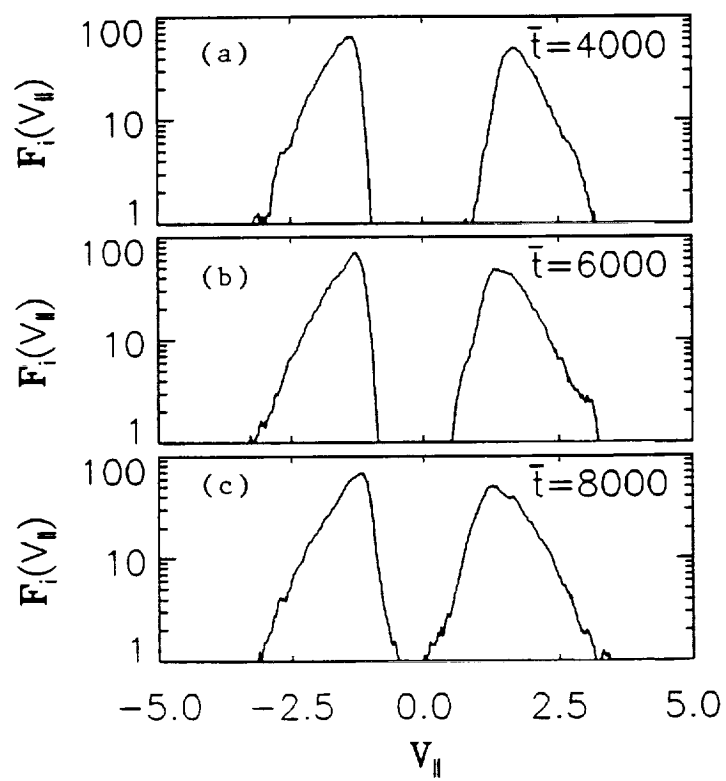


Fig. 5

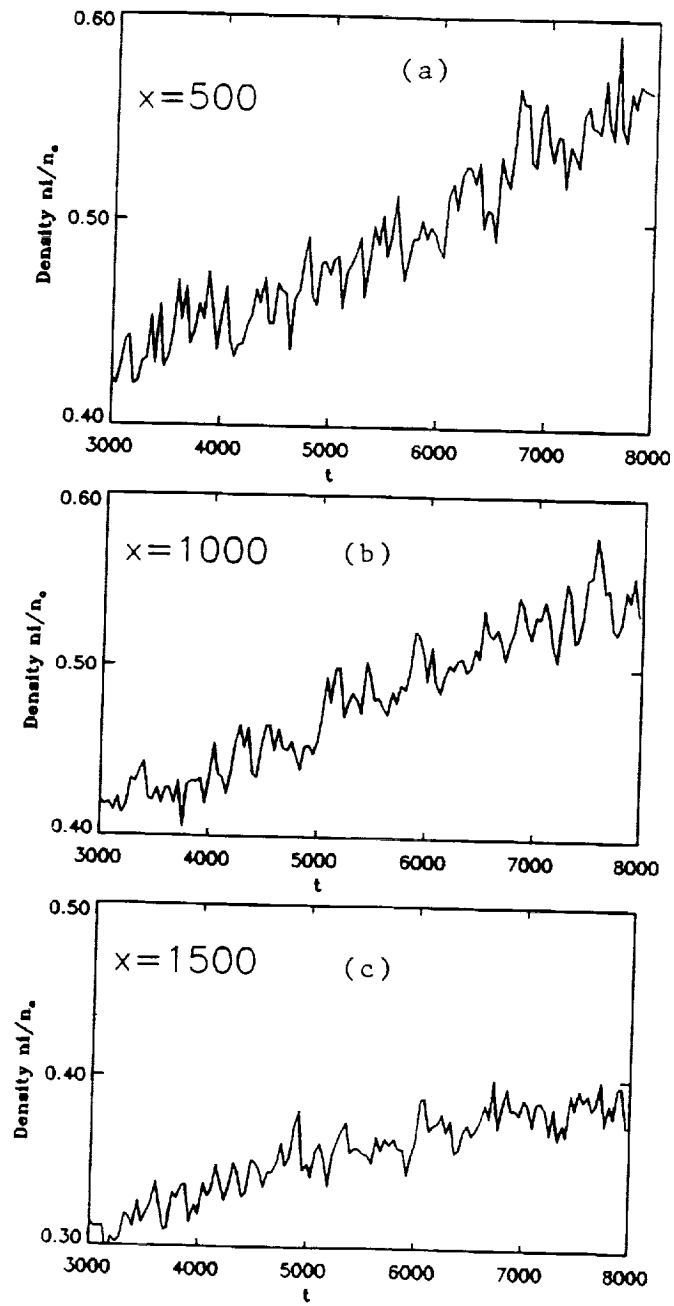


Fig. 6



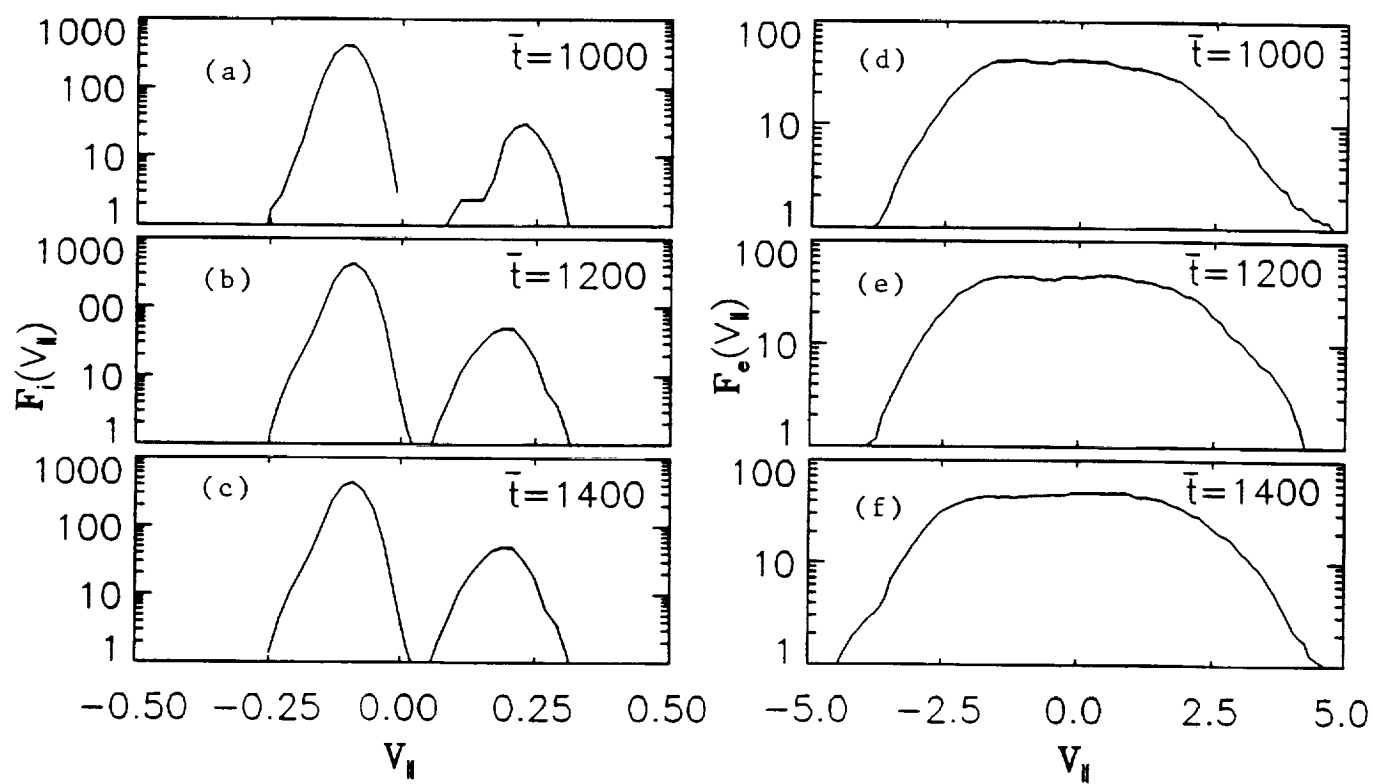


Fig. 7

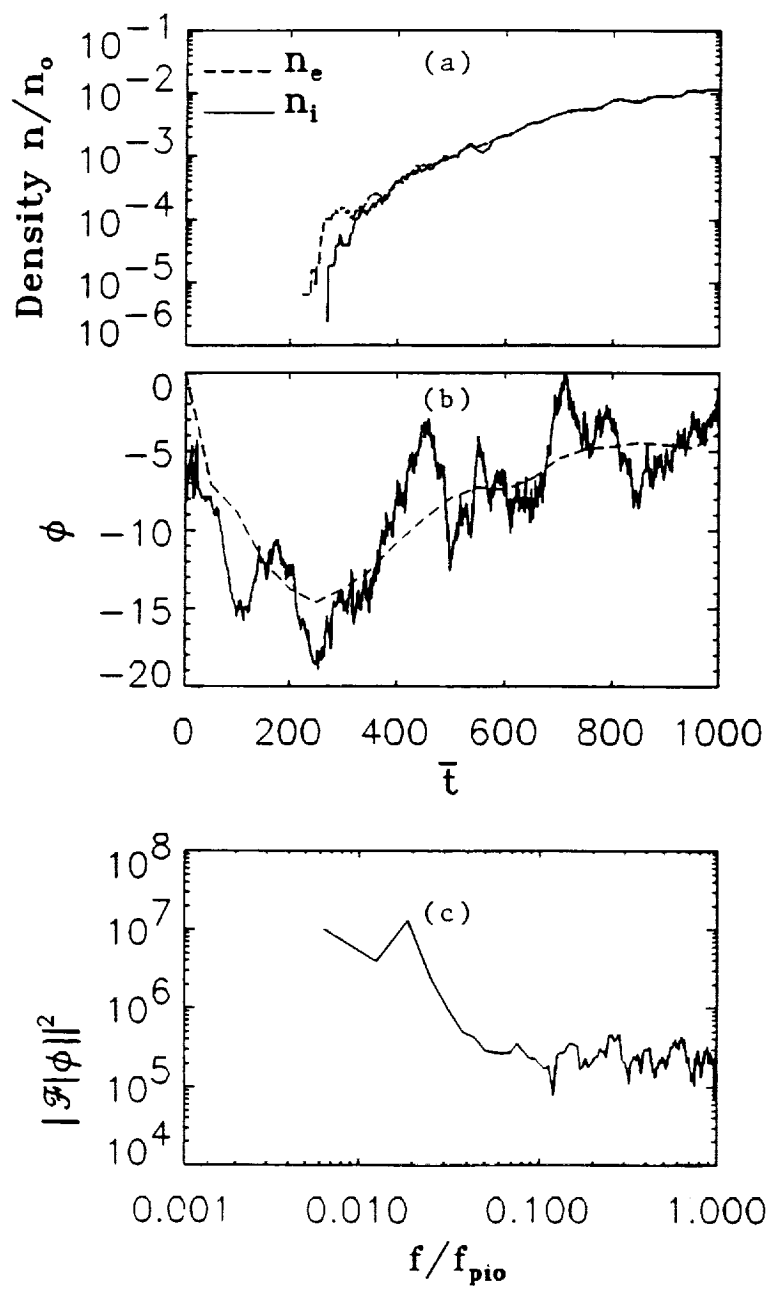


Fig.8

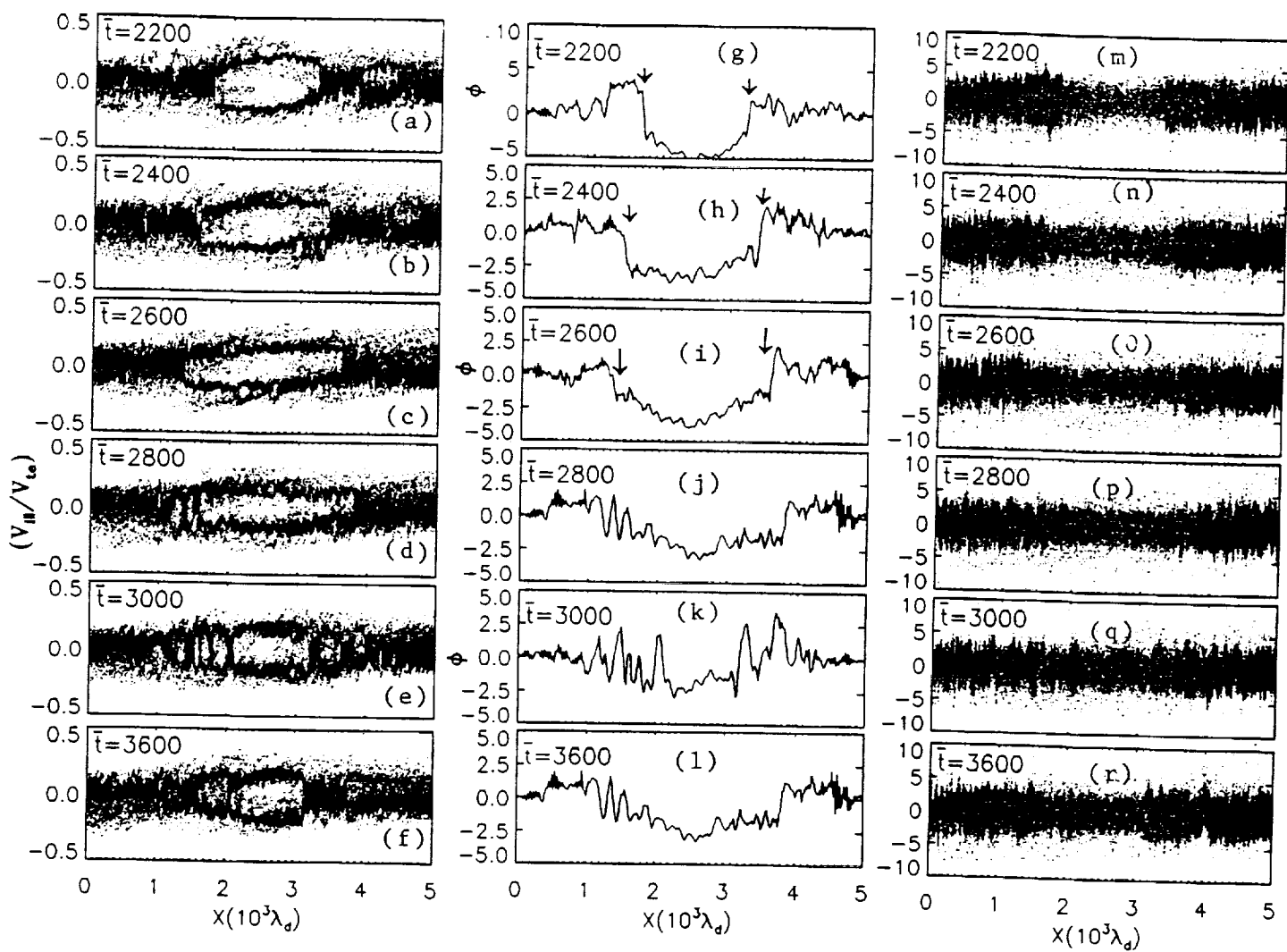


Fig. 9

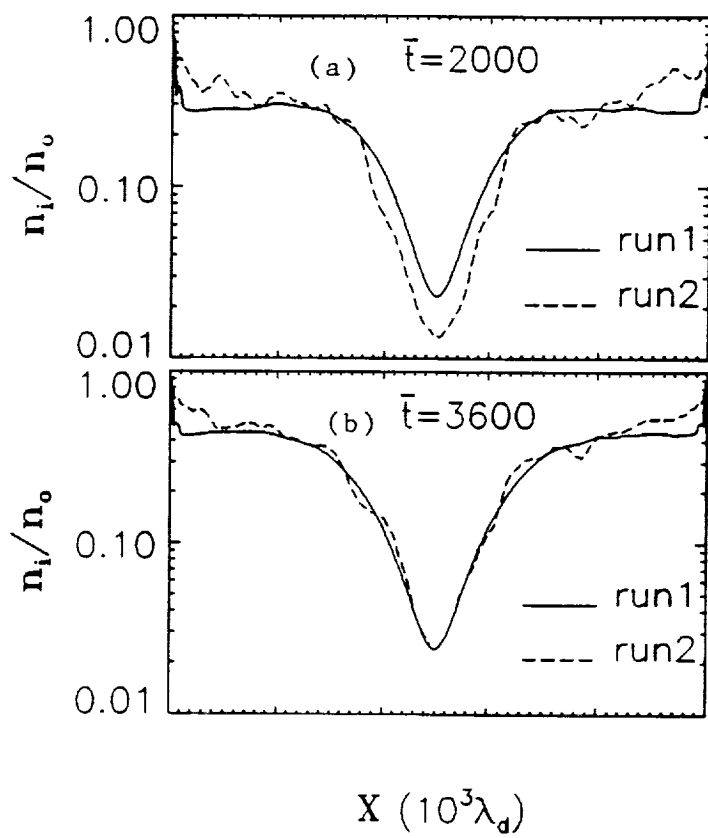


Fig. 10

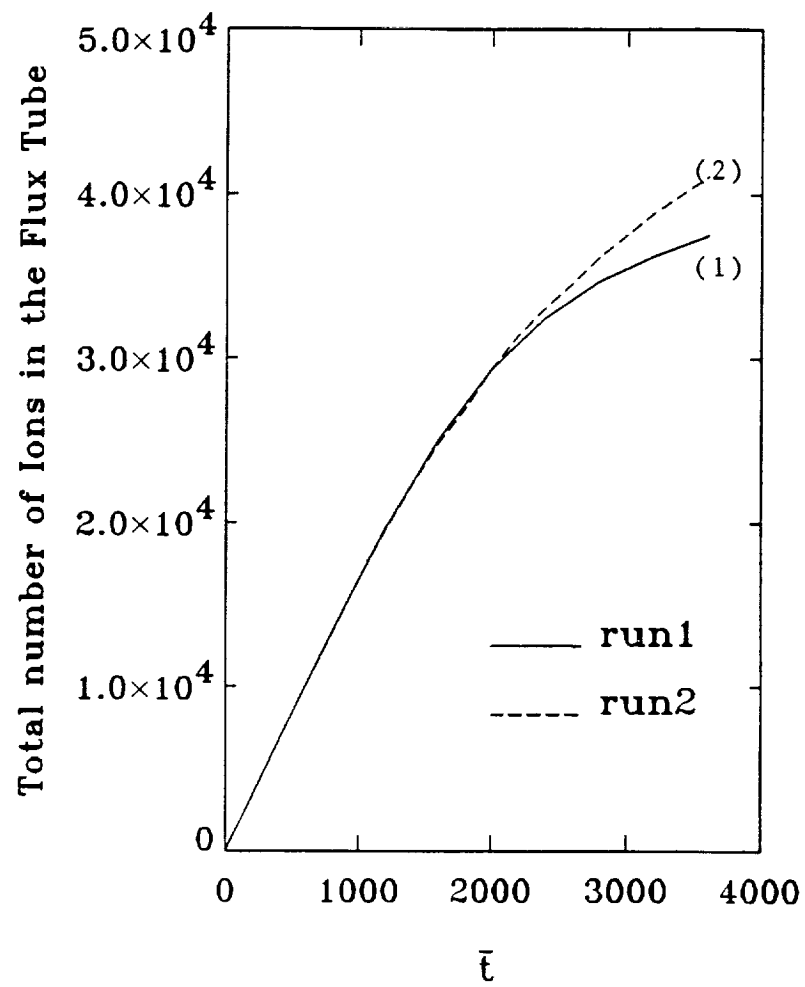


Fig. 11



NIS

**Numerical Simulation of**  
**Filling a Magnetic Flux Tube with a Cold Plasma:**  
**(2) Effects of Magnetically Trapped Hot Plasma**

**Nagendra Singh and W. C. Leung**

Department of Electrical and Computer Engineering & CSPAR  
University of Alabama, Huntsville, AL 35899

Submitted to *JGR*, April 1994

## Abstract:

Equatorially trapped hot plasmas are a common feature of the outer plasmasphere, where flux tube refilling with cold ionospheric plasma occurs after magnetic storms. The role of the hot plasma consisting of hot anisotropic ions and isotropic warm electrons in the refilling process is examined by means of numerical simulations using a one-dimensional particle-in-cell code. Simulations are performed on the filling of an artificial flux tube having a minimum magnetic field at its center. We have performed two types of simulations; in one type, called here Run-A, we allowed cold plasmas to flow into a centrally trapped hot plasma consisting of warm isotropic electrons and hot anisotropic ions with perpendicular temperature  $T_{\perp} > T_{\parallel}$ , the parallel temperature. Run-A reveals a variety of plasma processes relevant to the plasmaspheric refilling affected by the presence of a hot plasma, including formation of propagating electrostatic shocks, intrinsically unstable plasma distribution functions produced by the mixing of hot and cold plasmas, weak downward electric fields supported by an extended potential distribution in the relatively late stage of the evolution of plasma in the flux tube, and an enhanced flux tube filling. In the other type of simulation first a cold plasma flow was allowed to set up in the flow, then a hot plasma consisting of the isotropic electrons and anisotropic ions ( $T_{\perp} > T_{\parallel}$ ) was suddenly injected into the central region of the flux tube. In this case the main distinguishing feature was the formation of relatively stable shocks near the mirror points of the centrally trapped hot plasma. The shocks were found to be standing, unlike in the previous type of simulation. Since the standing shocks form near the effective mirror points of the centrally trapped hot ions, they are called mirror shocks to contrast them from the moving electrostatic shocks seen in Run-A. The stability of the standing shocks was found to increase with the decreasing temperature of the warm electrons injected with the hot plasma. Wherever possible, similarities between the results from the simulations and those from observational data are pointed.

## 1. Introduction

In a companion paper [Singh and Leung, 1994], hereafter referred to as Paper 1, we have studied the role of ion-beam driven plasma instability in filling a magnetic flux tube with a cold plasma. In this paper, we extend that study by including a hot plasma population trapped in the central region of the flux tube where the magnetic field is minimum as shown in Figures 1a and 1b. This study is motivated by the fact that the outer region of the plasmasphere is always populated by a hot plasma of plasmasheet and the ring current origins [Roux *et al*, 1982; Deforest *et al*, 1971]. Furthermore, at times a warm plasma population is created when cold ions in the equatorial region are transversely heated by waves generated by the hot plasma population [Olsen *et al*, 1987]. How do these warm and/or hot plasma populations affect the flow of cold plasma and the refilling of the plasmasphere? The purpose of this simulation study is to develop an understanding of the plasma processes driven by hot-cold plasma interactions, which are relevant to the plasmasphere.

The simulations show that a hot and/or warm plasma consisting of warm electrons and hot anisotropic ions with  $T_{\perp} > T_{\parallel}$  where  $T_{\perp}$  and  $T_{\parallel}$  are the perpendicular and parallel ion temperatures, respectively, have a profound effect on the flow of cold plasma and its accumulation in the flux tube. The hot plasma injection creates a potential barrier for the ions in the cold plasma flow. When the cold plasma flow comes into contact with the equatorially trapped hot plasma and the associated potential barrier, electrostatic shocks form near the contact points. The shocks propagate away from the hot plasma thermalizing the plasma behind it and leaving behind an extended potential distribution which is effective in trapping the cold ions and in enhancing the filling of the flux tube. On the other hand, when the hot plasma is injected into the cold plasma flow with persistent counterstreaming ion beams in the central region of the flux tube [Singh and Leung, 1994], standing shocks form with a relatively stable potential structure localized in the minimum magnetic field region. The stability of the standing shocks increases with decreasing temperatures of the warm isotropic electrons injected with the hot anisotropic ions.

When the hot and cold plasma spatially mix together, unstable plasma distribution functions are created; the salient feature of the ion perpendicular velocity distribution is that a ring distribution forms around the core of cold ions. The minimum energy of the ring distribution approximately corresponds to the potential barrier set up by the hot anisotropic ions. Such low energy rings can drive lower-hybrid and/or magnetosonic waves below and near the lower-hybrid frequency [Lee and Birdsall, 1979], which can heat the cold ions. This is in contrast to the energetic ( $> 5$  keV) ion rings produced by the injection and transport of ions [Roux *et al*, 1982; Deforest and McIlwain, 1971]; such energetic rings create waves which are too fast to resonate with the cold ions and, therefore, are ineffective in heating them.



The simulation model used in this paper is the same as discussed in section 2 of Paper 1. However, in the simulations described here we include a hot plasma in the central region  $2300 \leq \bar{X} \leq 2700$  (Figure 1a). The properties of the hot plasma and the timing of their injection are described later at appropriate places. Some initial results from the present study were reported earlier [Singh, 1993].

The rest of the paper is organized as follows. In section 2 we describe the results from the simulation in which hot plasma is injected initially at time  $t = 0$ . In section 3 we describe the results from the simulation in which hot plasma is injected at a later time when the cold plasma flow is already set up in the flux tube. The properties of the velocity distribution functions of electrons and ions as seen from the runs are described in section 4. Section 5 deals with the filling of the flux tube with cold plasma. The conclusions of the paper are given in section 6.

## 2. Cold Plasma Flowing into a Hot Plasma

We first discuss the results from a simulation in which cold plasmas expanding from the plasma reservoirs in Figure 1a come into contact with the hot plasma trapped in the central region of the flux tube where the magnetic field minimizes (Figure 1b). Hereafter we refer to this simulation as Run-A. The situation considered in this simulation corresponds to that of the fast ion streams flowing into the equatorially trapped hot plasma during the early stage of the plasmaspheric refilling. Some preliminary results from this run were presented in a previous paper [Singh, 1993]. The hot plasma has the following properties;  $T_{i\perp}^H = 2 T_{i\parallel}^H = 1800 T_o$  and  $T_{e\perp}^H = T_{e\parallel}^H = T_e = 10 T_o$ , where  $T_o$  is the cold plasma temperature in the plasma reservoirs. When the hot plasma is the only plasma in the flux tube, the difference between the temperature anisotropy of electrons and ions sets up electric fields pointing away from the central region and the corresponding potential distribution is given by [Whipple, 1977]

$$\phi(x) = (kT_{i\parallel}^H / e) [1 + T_{i\parallel}^H / T_e]^{-1} \ln \Gamma \quad (1)$$

where  $\Gamma = (T_{i\perp}^H / T_{i\parallel}^H)(1 - B_m / B(x)) + B_m / B(x)$ ,  $B_m$  is the minimum magnetic field, and  $B(x)$  is the magnetic field at the point where the potential is  $\phi(x)$ .

When  $B_m / B \ll 1$  and  $T_e \ll T_{i\parallel}^H$ , equation (1) is simplified to  $\phi(x) \cong (kT_e / e) \ln(T_{i\perp}^H / T_{i\parallel}^H)$ . For  $T_e = 10 T_o$ , and  $T_{i\perp}^H / T_{i\parallel}^H \cong 2$ , the potential difference between the point of minimum magnetic field and the point where the magnetic field is  $B(x)$  is about  $7 kT_o / e$ . This maximum potential drop is expected without any cold plasma in the flux tube.

Large-scale refilling models [Singh et al, 1986; Wilson et al, 1992] indicate ion flow velocities upto 30 km/s during the early refilling stage, the corresponding kinetic energy of  $H^+$  ion beam is  $< 5$  eV, which is smaller than the maximum potential energy of the ions estimated above for  $T_o = 1$  eV. Thus, the hot plasma is expected to have a significant effect on the flow of cold plasma, and hence on the refilling processes.

We performed several simulations in which hot plasma properties were varied. We found that as long as hot ions are anisotropic with  $T_{i\perp}^H > T_{i\parallel}^H$  and the warm electrons are isotropic or anisotropic with the reverse anisotropy, that is,  $T_{e\perp}^H > T_{e\parallel}^H$ , the basic effects of the hot plasma on the cold plasma flows are the same. Therefore, we describe here only the results from the simulation run with the hot plasma properties as mentioned above.

Figures 2a to 2e shows the evolution of the ion phase-space in the  $\bar{X} - \bar{V}_{i\parallel}$  plane. Figure 2a for  $\bar{t} = 200$  shows the expanding ion beams from the plasma reservoirs at  $\bar{X} = 0$  and  $\bar{X} = d$ . For showing some details of the cold ion phase space, the vertical scale in Figure 2 is expanded and it does not fully show the velocity space of the hot ions. At  $\bar{t} = 400$  (Figure 2b), the ion beams begin to come into contact with the hot plasma. The plot at  $\bar{t} = 600$  (Figure 2c) shows that the incoming ion beams are being reflected. This reflection is expected because the potentials set up by the hot plasma provide sufficiently large barriers for the approaching ion beams. The evolution of the potential distribution corresponding to that of the phase space (in Figure 2) is shown in Figure 3a to 3p. An important feature of the potential distribution is the occurrence of a potential pulse coinciding with the central hot plasma for  $\bar{t} \leq 1000$ . The peak potential at  $\bar{t} = 200$  is  $15 kT_o / e$ , which is nearly double the potential predicted by equation (1). The development of the large potential is attributed to the

space charges developing in the system. In contrast, equation (1) is based on the assumption of a quasineutral plasma. The expansion of the cold plasma compresses the potential pulse as seen from the plots in Figure 3 for  $200 \leq \bar{t} \leq 800$ , after which the edges of the pulse steepen into shock like structures and the pulse broadens again and slowly diminishes in amplitude reaching an asymptotic value of about  $5kT_o/e$  at  $\bar{t} = 1400$ . The broadening of the potential pulse is associated with the outward propagation of the shocks. The evolution of the potential distribution at later times is affected by the shock propagation and, outside the central region between the two shocks, it is also affected by the ion-ion instabilities as discussed in Paper 1. The ion-ion instability creates vortices in the  $X - V_{||}$  phase space as seen at  $\bar{t} = 1600$  in Figure 2g and the corresponding perturbations in the potential distribution in Figure 3g.

It is useful to discuss the mechanism of the shock formation. When counterstreaming ion beams begin to interpenetrate, a pair of electrostatic shocks form due to the coupling between the ion beams affected by the ion-ion instability [Forslund and Shonk, 1970; Singh, 1990]. As we discussed in Paper 1, in the absence of the central hot plasma, the ion beams continue to counterstream indefinitely because their relative beam velocity  $V_{rb}$  is too fast to satisfy the conditions for the ion-ion instability which are  $V_{rb} < 2C_s$  and  $T_e > 3T_i$  where  $C_s$  is the ion-acoustic speed and  $T_e$  and  $T_i$  are the electron and ion temperatures; the instability in the central region does not occur even though the latter condition on temperature is satisfied due to the electron heating by the electron-ion instability. In the present situation with the central hot plasma, the counterstreaming on both sides of the hot plasma is created by the reflection of the ion beams by the central potential barrier. The relative ion beam velocities between the counterstreaming ion beams on both sides of the potential pulse near the reflection point are  $\bar{V}_{br}$  0.5, 0.4, 0.32, and 0.26 at  $\bar{t} = 600, 800, 1000$  and  $1200$ , respectively. We recall that central hot plasma consists of a warm electron population with temperature  $T_e = 10T_o$ , which yields an ion-acoustic speed  $\bar{C}_s = 0.16$ . Thus the condition for the ion-ion instability near the reflection point is satisfied for  $\bar{t} \geq 1000$ . It is important to point out that the shocks form just outside the region where hot ions are trapped; outside this region the cold ions dominate and satisfy the temperature condition mentioned above. The instability couples and mixes the counterstreaming ion beams forming a "mixed" plasma "tab" developing near the shocks, one on each side of the central hot plasma (Figures 3e and 3f); the plasma tabs appear in the phase space plots as the darkest areas between the hot plasma and the counterstreaming ion beams. The extension of the tabs of mixed plasma along with outward propagation of the shocks is clearly seen by comparing the phase space plots in Figure 2 for  $\bar{t} = 1200$  to  $2400$ . The outward propagation of the electrostatic shocks are indicated by the arrows in Figure 2f to 2i and Figures 3f to 3i. After their formation at about  $\bar{t} = 1200$ , shocks move away from the central region with a velocity  $V_{sh} \cong 0.05V_{te} \cong V_{ti}$ , where  $V_{te}$  and  $V_{ti}$  are the electron and ion thermal speeds in the cold plasma, respectively.

As the shocks propagate out, ion-ion instability occurs in the regions ahead of the shocks as seen at  $\bar{t} = 1600, 2000$  and  $2400$  in Figure 2, the instability creates vortices in the phase space. The combined effects of the shock propagation and the ion-ion instability mix the counterstreaming ion beams nearly all along the flux tube as seen from Figure 2 for  $\bar{t} \geq 2800$ . This mixing of counterstreaming ion beams all along the flux tube is quite different from what we saw in Paper 1 that the counterstreaming persists in the central region (see Figures 4a to 4f and 9a to 9f in Paper 1).

The evolution of the electron phase space, corresponding to those of the ion phase space in Figure 2, and the potential distributions in Figure 3, is shown in Figure 4. The prominent features of the electrons before  $\bar{t} \leq 400$  are the two spatially-separated electron populations; the centrally trapped electrons in the potential well shown in Figure 3 and the electrons expanding into the flux tube from the plasma reservoirs at  $X = 0$  and  $X = d$ . For  $\bar{t} \geq 1200$ , we see the signature of the shock pair in the electron phase space; the centrally trapped electrons develop sharp edges like the potential distribution (Figure 3) and the ion phase space (Figure 2), all marked by arrows. Along with the outward propagating shocks, the centrally trapped electrons expand away from the central region. Even after the shocks have propagated out to the boundaries, the electron phase space shows a gradual "bulging" from the ends to the central region, in agreement with the potential distribution in Figure 3 for  $\bar{t} \geq 2400$  when the potential in the central region remains positive and the potential distribution has gentle gradients giving electric fields pointing towards the ends.

Figures 2 and 4 for  $\bar{t} \leq 800$  show that as the cold plasmas expand to the central hot plasma, ion beams are reflected while the electron gas is accelerated toward the center. Therefore, in the early stage the cold

ion beams are initially excluded from the central region, but eventually the electrons pull them into the hot plasma region. When the cold electrons are accelerated by the central potential pulse, the additional negative charge lowers the peak potential after  $\bar{t} > 600$  as seen from Figure 3. This allows the cold ions to penetrate into the hot plasma region. The penetration is clearly seen from the ion phase plots in the  $X - V_\perp$  plane as shown in Figure 5. As seen from Figure 2, at times prior to  $\bar{t} = 400$  the hot ions trapped in the central region are separated from the cold ions in the configuration space. Figure 5a shows the situation when the cold ion beams come into contact with the centrally trapped hot plasma, having perpendicular velocities upto about  $V_\perp = 9$ . As the cold plasmas expand and the ions reflect from the potential barrier, there are accumulations of plasmas near the reflection points forming fronts which move towards the midpoint of the simulation region as seen from the plots for  $600 \leq \bar{t} \leq 1600$  in Figure 5. By the time  $\bar{t} = 1600$ , the cold ions have punched through the potential barrier, and the further evolution of the  $X - V_x$  phase space does not reveal any new feature. The  $X - V_\perp$  phase space plot at the end of the simulation run is shown in Figure 5d. Later we discuss the perpendicular velocity distribution function of the ions consisting of the cold and hot populations as seen from this figure. The evolution of the electron phase space in  $X - V_\perp$  does not reveal any noteworthy feature, except that, like the ions, electrons have a warm population trapped in the central region along with the cold electrons.

Evolution of the plasma density distribution in the flux tube is shown in Figure 6. The density distribution at  $\bar{t} = 200$  shows that the cold plasma is well separated from the centrally trapped hot plasma. The maximum normalized density of the hot plasma is about 0.05. As the cold plasmas expand, eventually the density maximum at the midplane ( $\bar{x} = 2500$ ) disappears and a density minimum occurs there. In our simulation, this occurs at about  $\bar{t} = 800$ . In a recent paper *Olsen et al* [1994] suggested that the equatorial density distribution of the trapped ions with  $T_\perp > T_\parallel$  depends on the electron temperature anisotropy; specifically they suggested that for isotropic electrons the trapped ion density distribution has a density maximum at the equator. On the other hand, when  $T_{e\parallel} > T_{e\perp}$  the density distribution has minimum at the equator. Our simulation shows that the occurrence of the density maximum or minimum depends on the stage of the mixing of the cold and the hot plasmas. When the hot plasma density dominates, the trapped ion density profile has a density maximum where the magnetic field minimizes. When the cold plasma flow begins to dominate the hot plasma density, the maximum disappears and a density minimum appears in its place.

The shocks seen in the ion phase space (Figure 2) and the potential distribution (Figure 3) are also seen from the density distributions for  $\bar{t} = 2000$  in Figure 6; the shocks are indicated by the arrows. Figure 6 shows the filling of the flux tube with the cold plasma flowing into it from the plasma reservoirs. Later we discuss the filling in more detail.

### 3. Hot Plasma Injected into Cold Plasma Flow

In this section we describe the modification in the cold plasma flow already set up in the flux tube, when a hot plasma, like the one described in the previous section, is suddenly injected into the central region of the simulation system. Hereafter we refer to this simulation as Run-B. The situation considered in this simulation corresponds to the injection of the hot plasma in a relatively late stage of the plasmaspheric refilling. We have already discussed in Paper 1 the evolution of cold plasma flow without a hot plasma. So far as the ion phase space is concerned, we saw in Paper 1 that after  $\bar{t} > 2000$  the main feature of the flow is that the ion instability mixes the ion beams in the outer region of the flux tube while they continue to counterstream in the central region. We also noted that the potential distribution in the central region is negative. The state of the cold plasma just before the injection of the hot plasma ( $\bar{t} = 2000$ ) is shown in Figure 7; Figures 7a and 7b show the ion phase space in  $X - V_\parallel$  and  $X - V_\perp$  planes, respectively; the corresponding electron phase space plots are shown in Figures 7c and 7d; and the potential distribution in Figure 7e. The injection of the hot plasma modifies the cold plasma flow in several ways, which are discussed below.

The evolution of the ion phase space in  $X - V_\parallel$  plane after the injection is shown in Figure 8. The obvious features of the phase space, as seen from Figure 8, are (1) the coupling between the counterstreaming ion beams in the central region where the hot plasma is trapped, and (2) generation of counterstreaming of ion beams progressively increasing in extent on both sides of the hot plasma; the extension of the counterstreaming regions is marked by arrows in Figures 8a to 8d. However, this newly generated counterstreaming does not last too long; the ion-ion instability couples the ion beams and mixes them as seen from the plots in Figures 8d, 8e and 8f.

The coupling of the ion beams in the region of the hot plasma is caused by the electric fields generated by the hot plasma injection. Figure 9 shows the evolution of the potential distribution after the injection. Note that just before the injection the potential distribution has a broad minimum in the central region (Figure 8e). The plot at  $\bar{t} = 2200$  in Figure 9a shows that the hot plasma creates a potential pulse at the center. With increasing time, the potential pulse broadens and its edges steepen somewhat. Furthermore, the negative potential regions on both sides of the potential pulse grow in size from  $\bar{t} = 2200$  to  $\bar{t} = 2800$  as indicated by the arrows. The regions with negative potentials contain the counterstreaming ion beams shown in Figure 8 for the same time interval. We point out here that the growing size of the negative potential region along with the ion counterstreaming in it was seen in Run-2 of Paper 1 without the hot plasma as shown in Figure 9 of that paper. Therefore, the extension in the size of the counterstreaming is not caused by the hot plasma injection, but it is caused by the outward motion of the shock-like structures marked by the arrows in Figure 7e due to the decrease of the ion flux into the central region by the vortices set up in the outer regions of the flux tube (Figures 7a and 7e). This point is discussed in greater detail in Paper 1. The fluctuation in the potential distribution on both sides of the pulse (Figures 9e and 9f) and the associated vortices in the phase space (Figures 8e and 8f) are caused by the ion-ion instability, which is eventually seen to affect the potential pulse at late times  $\bar{t} \geq 3400$ , but the core of the pulse is found to remain stable with an amplitude of about  $2.5kT_o/e$ .

**Injection of Hot Plasma with Colder Electrons:** We repeated the above simulation (Run-B) by injecting a hot plasma with electrons colder than that in Run-B; we chose  $T_e = 3.3 T_o$  in contrast to  $10 T_o$  in Run-B. We refer to this new run as Run-C. As before the hot plasma was injected at  $\bar{t} = 2000$  and the basic features of the evolution of the plasma and potential prior to  $\bar{t} = 3000$  were nearly the same in Run-B and Run-C. However, in Run-C with the colder electrons the central potential pulse remains quite stable without being severely affected by the ion-ion instability. This is shown in Figure 10; Figures 10a, 10b and 10c show the potential distributions at  $\bar{t} = 3200, 3600$  and  $4000$ ; Figures 10d, 10e and 10f show the corresponding ion phase space in  $X - V_{||}$  plane; and similarly Figures 10g, 10h and 10i show the electron phase space. Note that Figure 10 shows the pulse evolution over a longer time than that shown in Figure 9 for Run-B with the warmer electrons having  $T_e = 10 T_o$ . The potential distributions show that the stable potential pulse is flanked by negative potential regions in which counterstreaming ions persist. In the central positive peak region electrons are trapped electrostatically (Figures 10g, 10h and 10i), while ions are magnetically trapped in the same region. In the neighboring negative potential regions ions are trapped. In view of the alternate electrostatic trapping of the electrons and ions in their respective potential wells, the central peak is an "electron hole" and the negative potential wells on both sides of the potential pulse are "ion holes." This combination of the central electron and ion holes is remarkably stable at least over a time period  $\Delta \bar{t} = 20,000$  which is about 160 ion plasma periods. For a local plasma density of  $10 \text{ cm}^{-3}$ , we expect that the pulse should be stable for a time period of at least a few hundreds of milliseconds, and it should be easily observable from satellites. *Olsen et al*, [1987] have reported examples of equatorial plasma showing a sharp transition between counterstreaming field-aligned flows and an equatorially trapped highly anisotropic warm ion population. The central distribution of plasma and the potential, as shown in Figure 10, are qualitatively similar to the situation reported by *Olsen et al* [1987], although at a quite different spatial scale. Our simulations show that the transition between the field-aligned counterstreaming and the trapped ions occur near the effective mirror points of the latter ions. Therefore, we call the transitions mirror shocks to contrast them from the propagating electrostatic shocks seen in Run-A.

#### 4. Plasma Distribution Functions

We discuss here some interesting features of the electron and ion velocity distribution functions produced by the hot plasma injection. We found that the results on the velocity distribution functions from the runs discussed here did not differ significantly after the spatial mixing of the hot and cold plasmas. Therefore, in this section we primarily discuss the distribution functions as seen from Run-A.

We examine the distribution functions from two regions of the flux tube; near the ends of the tube, say for  $20 \leq \bar{x} \leq 240$ , and in the central region covering  $2300 \leq \bar{x} \leq 2700$ . The evolution of the ion distribution functions near the ends of the flux tube is shown in Figure 11. At early times ( $\bar{t} \sim 200$ ) the distribution shows an ion beam flowing into the flux tube. Eventually precipitating ions appear as an ion beam for  $V_{||} < 0$ ; at  $\bar{t} = 1000$  the beam velocity  $V_b \approx 0.24 V_{te} \equiv 5 V_{ti}$ . Later on both the inflowing and the precipitating ion beams

are seen to broaden progressively with increasing time. Eventually the ion beams for  $V_{||} < 0$  and  $V_{||} > 0$  begin to merge together and by the end of the simulation, the beams have completely merged. The above evolution of the ion distribution function is the combined effect of the expansion of the cold plasma into the flux tube, loss of some of the hot ions injected into the magnetic trap, reflection of the expanding ion beams from the electrostatic shocks (see Figure 2) and the ion-ion instability. A noteworthy feature of Figure 11 is that the precipitating ( $V_{||} < 0$ ) ions have energies greater than the inflowing ions. This merely reflects that some of the precipitating ions have undergone acceleration by the potential distribution set up by the hot plasma. In the course of the simulation, the midpoint ( $\bar{X} = 2500$ ) potential varies from about  $18 kT_o/e$  to  $2.5 kT_o/e$  (Figure 2). Thus, the precipitating ions cover a spectrum of energy extending to about  $15 kT_o/e$  which corresponds to a maximum velocity of about  $0.3V_{te}$  as seen in Figure 11 for  $V_{||} < 0$ .

The electron velocity distribution function near the ends of the flux tube is shown in Figure 12. The main feature of the electron distribution function is that at early times  $\bar{t} \approx 200$ , the distribution is symmetric about  $V_{||} = 0$  and it progressively becomes more and more asymmetric with energized electrons appearing for  $V_{||} < 0$ . The energization appears to occur primarily by the ion-ion instability, which transfers part of the ion beam energy to the electrons. The ion-ion instabilities are clearly seen from the vortex formation in the  $X - V_{||}$  phase space shown in Figure 2. Electron-ion instability is also likely to heat the electrons, especially during the early stages when the fast ion beams begin to precipitate near  $X = 0$  as seen from Figure 11 for  $\bar{t} \approx 10^3$ .

The asymmetry of the ion and electron velocity distribution functions in the relatively late stage of the filling of the flux tube, as shown in Figures 11 and 12, suggests that the plasmasphere refilling process in the presence of equatorially trapped hot plasma generates a downward heat flow, which may affect the energy budget of the topside ionosphere.

The evolution of the perpendicular velocity distribution functions of the ions and electrons near the ends of the flux tube do not show any interesting features. Examples of such distributions are shown in figures 13a and 13b, which are approximately the distributions in the cold plasma reservoirs.

The mixing of the hot and cold plasmas in the central region produces distribution functions having a core of cold ions and a halo of hot ions. Such parallel and perpendicular velocity distribution functions are shown in Figures 14a and 14b, respectively. (These distribution functions are for the ions in the central region  $(2300 \leq \bar{X} \leq 2700)$ ). In the parallel velocity distribution the cold core and the relatively hot ion populations are merged, but in the perpendicular velocity distribution, the hot ions are well separated from the cold population and they extend from a low velocity of  $V_{\perp} = 0.2$  to large velocities corresponding to that of the injected hot plasma. The hot ion population in Figure 14b appears as a beam in  $V_{\perp}$ . Since in gyrophase these hot ions are randomly distributed, the beam is a ring distribution in the perpendicular velocity. The ring distributions of energetic ions with energies 5-30 keV have been observed in the equatorial region of the outer plasmasphere and they are known to excite fast magnetosonic waves [Perraut et al, 1982]. However, the ring distribution seen from the simulation is considerably less energetic in the sense that its low energy end begins at an energy determined by the peak potential of the positive potential pulse seen in the simulations (Figures 3, 9 and 10). The production of such a ring distribution function has a simple explanation. The charged particles trapped inside a magnetic mirror have a loss cone distribution extending to zero velocities as long as the pitch angle ( $\alpha$ ) of the ions at the point of minimum magnetic field ( $B_{\min}$ ) satisfies the condition  $\alpha > \sin^{-1}(R^{-1/2})$  where  $R = B_{\max}/B_{\min}$  and  $B_{\max}$  is the maximum magnetic field in the flux tube (Figure 1b). However, the central potential pulse sets up electric fields, which accelerate the ions with relatively low perpendicular energies into the loss cone and they precipitate out.

In view of the amplitude of the potential pulse evolving with time (see Figure 3), the maximum parallel energy gain for the ions occurs during the early stage  $\bar{t} < 1000$ . For the maximum pulse amplitude of  $\bar{\phi}_o = 18$  (Figure 3), the parallel velocity of the ions accelerated by the potential pulse is  $V_{||\min} \approx (2q\phi_o/m_i)^{1/2} \approx 0.3V_{te}$ . If such ions remain trapped inside the magnetic mirror as the potential pulse evolves, the minimum perpendicular velocity at the midplane ( $X = X_{\text{mid}}$ ) is given by

$$V_{\perp\min} \approx (2q\phi_o/m_i)^{1/2} \tan \alpha_o$$

where  $\alpha_o = \sin^{-1}(R^{-1/2})$ . In our simulation  $R = 10$  and we estimate that  $V_{\perp\min} \approx 0.1V_{te}$ . Figures 5 and 14 show that the trapped particles have perpendicular velocities  $V_{\perp} > 0.2V_{te}$ . The discrepancies between this value

of  $V_{\perp}$  and the above estimate for  $V_{\perp \min}$  is attributed to the temporal evolution and the fluctuations of the potentials in the flux tube.

An interesting consequence of the low energy ring distribution is that it can excite a broadband waves over a frequency range from ion cyclotron frequency to the lower hybrid frequency [Lee and Birdsall, 1979]. However, in our one-dimensional simulation the wave generation process is suppressed. If the waves are generated, they can heat the cold ions, merging the cold core with the ring distribution. Composite perpendicular velocity distribution functions having a cold core and a halo of warm ions have been measured from the Dynamic Explorer-1 Satellite [Olsen et al, 1987].

The velocity distribution functions of the electrons in the central region are shown in Figures 15a and 15b. The parallel velocity distribution (Figure 15a) function shows a flat top distribution, indicating the trapping of the electrons in a potential well set up by the positive potential in the central region. The perpendicular distribution in Figure 15b shows a cold core along with a ring of warm electrons, which are trapped inside the magnetic mirror by virtue of their large perpendicular velocities. The ring in the perpendicular velocity of the electrons have the potential of driving electron cyclotron waves [Hasegawa, 1975].

## 5. Flux Tube Refilling

In Paper 1 we saw that the plasma waves enhance the filling of the flux tube by trapping plasma in vortexes set up by the ion-ion instability. We find that the hot plasma injected into the central region of the flux tube has a similar effect, although through a different process. We compare the filling of the flux tube as seen from the simulations reported in this paper (Run-A and Run-B) and those in Paper 1. Figure 16 shows the comparison of the flux tube contents from Run-2 of Paper 1, in which the filling was studied without the hot plasma, and Run-A and Run-B of this paper. Curve 1 is the same as in Figure 12 of Paper 1, but it is translated along the vertical axis by the initial number of the hot ions injected into the flux tube at  $t = 0$  in Run-A. Curves 2 and 3 show the evolution of the plasma content from Run-A and Run-B, respectively. The vertical translation of Curves 1 is done for the purpose of easy comparison of the cold plasma contents of the flux tube as seen from the different runs. We point out that the plasma content is just the total number of ions in the flux tube. Since each particle used in the simulation is equivalent to a large number of the real ions, we call the simulation ions macroions or computer ions. A comparison of Curve 1 with Curve 2 shows that the initially injected hot plasma facilitates the trapping of more cold plasma than that from the run without the hot plasma. In the simulation with the initially injected hot plasma (Run-A) enhanced trapping occurs by two processes: (1) the vortexes set up by the ion-ion instability like that shown by the enhanced filling in Run-2 (Curve 1) over that in Run-1 of Paper 1 (Figure 12, Paper 1); (2) the potential pulse and its evolution in an extended potential distribution (Figure 3) provide an additional mechanism for the trapping of the cold plasma. When cold plasma flows into the flux tube, the electric fields set up by the extended potential distribution slowly retard the flow and increase the ion density in the flux tube. The effect of this additional mechanism on the filling is illustrated in Figure 17, in which we compare the density profiles at the end of the simulations in Run-2 of Paper 1 and Run-A described in this paper. We notice that the enhanced density is confined in the central region from  $\bar{X} \cong 10^3$  to  $4 \times 10^3$ . One can argue that this enhanced density is due to the centrally trapped hot plasma, but the comparison of the total plasma contents from Run-2 and Run-A in Figure 16 clearly points out that the cold plasma content is enhanced. Since in Figure 17 the relative density enhancement in Run-A occurs over an extended region only inside the central portion of the flux tube, it is obvious that an additional amount of cold plasma is also contained in that region. The containment of the additional cold plasma is facilitated by the retardation of the inflowing ions by the relatively weak electric fields associated with the extended potential distribution in Figure 3 for  $\bar{t} > 2400$ .

In Run-B, in which the hot plasma was injected after the cold plasma flow was well set up in the flux tube, an enhanced refilling did not occur. In Figure 16, Curves 2 and 3 show the comparison of the total plasma contents from Run-A and Run-B. Curve 3 (solid line) shows the sudden injection of the hot plasma at  $\bar{t} \cong 2000$ . With the injection the total plasma content suddenly jumps from Curve 3 to Curve 1, but the content given by Curve 3 (Run-B) remains slightly lower than that given by Curve 2 (Run-A) near the injection time and it continues to show a lower value of the plasma content till the end of the simulation. We note that the contents shown by Curve 3 and Curve 1 for  $\bar{t} > 2000$  are quite close and are lower than that given by Curve 2 (Run-A), indicating that the late injection of the hot plasma does not contribute to the enhancement in the filling with the cold plasma. This is understood by noting that in Run-B the potential peak generated by the hot plasma does not

evolve into propagating shocks, creating an extended potential distribution with weak electric fields, which plays a key role in retarding the inflowing ions and in enhancing the cold plasma density in Run-A.

## 6. Conclusion and Discussion

The main aim of this paper is to study how a hot plasma trapped inside the minimum magnetic field region of a flux tube affects the filling of the tube with a cold plasma. We performed two simulations: (1) by injecting hot plasma initially and then allowing the cold plasma to expand into it, and (2) first a cold plasma flow was allowed to establish in the flux tube and then the hot plasma was injected. The simulations presented here, with the initial and delayed injection of the hot plasma, are illustrative examples of how hot and cold plasmas may come into contact. In the case of the outer plasmasphere, the contact may occur in a variety of situations ranging from the initial refilling stage with the cold plasma density  $< 1 \text{ cm}^{-3}$  to that of a nearly filled plasmasphere with densities of  $\sim 10^3 \text{ cm}^{-3}$ . The hot plasma in both cases consisted of hot anisotropic ions with  $T_{\perp} > T_{\parallel}$  and warm isotropic electrons. The simulations reveal new processes driven by the hot-cold plasma interactions. These processes are summarized as follows.

### Flow of Cold Plasmas into a Trapped Hot Plasma:

- 1) Hot plasma creates a potential barrier for the cold plasma flow. The magnitude of the potential differs from that given by theory [Whipple, 1977] which does not account for the presence of the cold plasma. We show that the potential evolves as the hot and cold plasmas interact.
- 2) The main feature of the evolution of the potential distribution is the formation and propagation of the electrostatic shocks. We saw in Paper 1 that in the absence of the hot plasma, the counterstreaming expansion of cold plasma in the flux tube sets up counterstreaming ion beams, which last for a relatively long time in the central region. In contrast to this, the potential barrier set up by the hot plasma reflects the incoming plasma flows on each side of the centrally trapped hot plasma. In the early stage the cold plasmas do not penetrate into the central region of the hot plasma. The reflection of ion beams sets up counterstreaming on each side of the hot plasma. The shock formation begins in the reflection region where beams are relatively slow and the warm electrons give a relatively large ion-acoustic speed. These two effects create the conditions for the ion-ion instability (see Paper 1), and hence the shocks form.
- 3) The propagation of the shock extends the positive potentials created by the hot plasma to large distances from where the hot plasma is trapped.
- 4) As the shocks propagate away from the central region of the flux tube, ion-ion instability occurs in the outer regions, as described in Paper 1. The combined effects of the shocks and the vortexes set up by the instability create an extended potential distribution, in which central region of the flux tube remains generally positive.
- 5) The extended potential distributions help in trapping more cold plasma than that in the run without the hot plasma. The trapping occurs by retarding the inflowing ions in the flux tube. Thus, the filling of the flux tube with the cold plasma is enhanced by the presence of the equatorially trapped hot plasma.
- 6) The plasma distribution functions resulting from the hot-cold plasma interaction show some interesting features. We found that the precipitating ion beams and electrons, which are leaving the simulation system, are energized by the plasma processes occurring in the flux tube. This suggests that the hot-cold plasma interaction may eventually deposit some energy into the topside temperature during the refilling of a plasmaspheric flux tube.
- 7) The ion velocity distribution function in the central region consists of a cold core and a halo of hot ions. In the perpendicular velocity distribution, the hot ions appear as a ring starting at a low perpendicular energy which approximately corresponds to the maximum potential barrier set up by the hot plasma population. Such ring distributions can generate waves in the frequency band from the ion gyrofrequency to the lower-hybrid frequency [Lee and Birdsall, 1979]. However, such waves cannot be studied by the one-dimensional simulations used in the present work.
- 8) Even the electron perpendicular velocity distribution shows a ring, which are known to drive electron cyclotron waves at frequencies  $f \cong (n + \frac{1}{2}) f_{ce}$ , where  $f_{ce}$  is the electron cyclotron frequency and  $n$  is an integer [Hasegawa, 1975].

### Injection of a Hot Plasma into a Cold Plasma Flow:

When a hot plasma is injected into a cold plasma flow already set up in the flux tube, we found the following interesting results:

- 1) The hot plasma with anisotropic ions and warm isotropic electrons generates a positive potential pulse, which is relatively stable as it remains confined to the central region. The stability of the pulse increases with colder electrons in the injected hot plasma. The edges of the pulse appear like a pair of standing shocks with counterstreaming ions on both sides of the potential pulse. This situation is qualitatively similar to that found in the equatorial plasmasphere with sudden transition between counterstreaming ions and the equatorially trapped anisotropic ions with  $T_{\perp} > T_{\parallel}$  [Olsen *et al*, 1987].
- 2) The standing shocks form near the boundaries of the centrally trapped hot ions. Since the ions are trapped by the mirror face, the shocks form near the effective mirror points and, therefore, we call them mirror shocks. This nomenclature distinguishes these shocks from the electrostatic shocks created by the electrostatic processes of ion-ion instability.
- 3) The injection leads to expulsion of cold plasma, reducing the plasma content of the flux tube relative to that in the run with the initial injection of hot plasma.
- 4) The mixing of hot and cold plasma eventually generates plasma distribution functions similar to those shown in Figures 14 and 15 for the run with the initial injection of the hot plasma.

The above results cannot be directly applied to the problem of plasmaspheric refilling. The purpose of this paper is to study the variety of plasma processes driven by hot-cold plasma interactions which occur in the outer plasmasphere. Some of the processes, such as the formation of shocks and the creation of the potential distributions in the flux tube capable of trapping more plasma are well brought out by the one-dimensional simulation. On the other hand, the results presented above indicate the possibility of some processes which need multidimensional simulations. For example, the distributions shown in Figure 14 are inherently unstable and they can excite waves in the frequency band from proton gyrofrequency to the lower hybrid frequency. Such waves have been observed in the equatorial region and have been invoked to explain the heating of the cold ions [Olsen *et al*, 1987]. However, in the past it has been suspected that the waves are driven by energetic (5-20 keV) proton ring distributions. The waves excited by such beams are too fast to resonate with cold ions and therefore they cannot heat them. The low energy rings generated by the hot-cold plasma interactions can excite relatively slower waves, which could heat the cold ions merging the cold plasma with the hot plasma ring in Figure 14. The merging is likely to produce composite distribution functions with two temperatures as reported by Olsen *et al* [1987]. In a recent paper Olsen *et al* [1994] suggested that the density distribution of the trapped ions in the equatorial region depends on the electron temperature anisotropy. We found from our simulations that the nature of the density distribution in the presence of the trapped ions depends on the evolution of the cold plasma density relative to that of the trapped ions. When the latter density dominates a density maximum occurs at the equator, otherwise a density minimum occurs when the cold plasma density dominates. This is found to be true when the electron distribution has both trapped and field-aligned populations.



## References

- Deforest, S. E., and C. E. McIlwain, Plasma clouds in the magnetosphere, *J. Geophys. Res.*, 76, 3587, 1971.
- Hasegawa, A., *Plasma Instabilities and Nonlinear Effects*, Springer-Verlag, Berlin, Chapt. 2, 1975.
- Lee, J. K., and C. K. Birdsall, Velocity space ring-plasma instability, magnetized, Part 1: Theory, *Phys. Fluids*, 22, 1206, 1979.
- Olsen, R. C., C. R. Chappell, D. L. Gallagher, J. L. Green, C. R. Campbell, and R. R. Anderson, Plasma observations at the magnetic equator, *J. Geophys. Res.*, 92, 2385, 1987.
- Olsen, R. C., L. J. Scott, and Boardsen, Comparison between Liouville's theorem and observed latitudinal distributions of trapped ions in the plasmasphere region, *J. Geophys. Res.*, 99, 2191, 1994.
- Perraut, S., A. Roux, P. Robert, and R. Gendrin, A systematic study of VLF waves above  $F_H^+$  from GEOS-1 and -2 measurements and near relationship with proton ring distributions, *J. Geophys. Res.*, 87, 6219, 1982.
- Rasmussen, C. E., and R. W. Schunk, Multistream hydrodynamic modeling of interhemispheric plasma flow, *J. Geophys. Res.*, 93, 14, 557, 1988.
- Roux, A., S. Perraut, J. L. Ranch, C. D. Villedary, C. Kremser, A. Rorths, and D. T. Young, Wave particle interactions near  $\Omega H_e^+$  observed on board GEOS-1 and -2. Generation of ion cyclotron waves and heating of  $H_e^+$  ions, *J. Geophys. Res.*, 87, 8174, 1982.
- Singh, N., Comment on "Multistream hydrodynamic modeling of interhemispheric plasma flow, by C. E. Rasmussen and R. W. Schunk, *J. Geophys. Res.*, 95, 17, 272, 1990.
- Singh, N., Interaction of field-aligned cold plasma flows with an equatorially trapped hot plasma: Electrostatic shock formation, *Geophys. Res. Lett.*, 20, 799, 1993.
- Singh, N., R. W. Schunk, and H. Thiemann, Temporal features of the refilling of a plasmaspheric flux tube, *J. Geophys. Res.*, 91, 13433, 1986.
- Whipple, E. C., The signature of parallel electric fields in a collisionless plasma, *J. Geophys. Res.*, 82, 1525, 1977.
- Wilson, G. R., J. L. Horwitz, and J. Lin, A semikinetic model for early stage plasmasphere refilling. 1, Effects of Coulomb collisions, *J. Geophys. Res.*, 97, A2, 1049, 1992.

## FIGURE CAPTIONS

**Figure 1.** Geometry of the simulation. (a) The flux tube with the cold plasma reservoirs near its ends are shown. The hot plasma is injected in the center of the flux tube where the magnetic field is minimum as shown in (b).

**Figure 2.** Temporal evolution of ion phase space in the  $\bar{X} - \bar{V}_{i\parallel}$  plane (Run-A). Note the central hot ions; the entire distribution of the hot ions is not shown; it is truncated at  $\bar{V}_{i\parallel} = \pm 1$  so that the cold plasma distribution can be adequately resolved. Note the reflection of ions, formation and propagation of electrostatic shocks.

**Figure 3.** The temporal evolution of the potential distribution corresponding to that of the ion phase space in Figure 2. Note the evolution of the shock from the potential pulse set up by the centrally trapped hot plasma.

**Figure 4.** The temporal evolution of the electron phase space in  $\bar{X} - \bar{V}_{e\parallel}$  plane corresponding to that of the ions in Figure 2 and the potential distribution in Figure 3.

**Figure 5.** Evolution of ion phase space in the  $\bar{X} - \bar{V}_{i\perp}$  plane (Run-A). Note the presence of the centrally trapped hot ions. At early times the expanding cold ions create density fronts when they come into contact with the hot plasma as shown by arrows. The fronts eventually punch through the hot plasma mixing the cold and hot plasmas spatially.

**Figure 6.** Temporal evolution of the total ion density in the flux tube (Run-A). At early times the hot plasma creates a density maximum at the center. As the cold plasma fills the tube, the density maximum eventually disappears. The signature of the electrostatic shocks in the density distribution is indicated by the arrows on the density profile for  $\bar{t} = 2000$ .

**Figure 7.** State of the cold plasma in the flux tube at  $\bar{t} = 2000$  just before the delayed injection of the hot plasma (Run-B). (a)  $\bar{X} - \bar{V}_{i\parallel}$  ion phase space, (b)  $\bar{X} - \bar{V}_{i\perp}$  ion phase space, (c)  $\bar{X} - \bar{V}_{e\parallel}$  electron phase space, (d)  $\bar{X} - \bar{V}_{e\perp}$  electron phase space, and (e) potential distribution.

**Figure 8.** Temporal evolution of the ion phase space in  $\bar{X} - \bar{V}_{i\parallel}$  plane (Run-B). Note the central mixing of the counterstreaming ion beams shown in Figure 6a in response to the delayed injection of the hot ions. Also noteworthy, is the extension of the counterstreaming on both sides of the hot plasma and eventual mixing by the ion-ion instability.

**Figure 9.** Evolution of the potential distribution in response to the delayed injection of the hot plasma (Run-B). Note the appearance of the potential pulse in the central region.

**Figure 10.** Stability of the potential pulse and its evolution into standing mirror shocks are shown when the temperature of the warm electrons in the hot plasma is reduced from  $10 T_o$  in Run-B to  $3 T_o$  in Run-C. (a) to (c) Potential distributions. (d) to (f) Ion phase space in  $\bar{X} - \bar{V}_{i\parallel}$  plane. (g) to (i) Electron phase space in  $\bar{X} - \bar{V}_{e\parallel}$  plane from Run-C.

**Figure 11.** Evolution of the ion velocity distribution function  $F_i(V_{\parallel})$  near the end of the flux tube ( $100 \leq \bar{X} \leq 500$ , Run-A). Note the ions reflected ( $V_{\parallel} < 0$ ) from the central potential pulse created by the hot plasma injected at  $t = 0$ . Eventually the inflowing and the reflected ions merge together. Asymmetry of the distribution function suggests heat flux into the topside ionosphere.

**Figure 12.** Same as Figure 11, but for the electrons.

**Figure 13.** Perpendicular velocity distributions (Run-A). (a) Ions and (b) Electrons ( $100 \leq \bar{X} \leq 500$ ) at  $\bar{t} = 3600$ .

**Figure 14.** Ion velocity distribution functions at  $\bar{t} = 3600$  in the central region of the flux tube where hot and cold ions have mixed. (a)  $F_i(V_{\parallel})$  and (b)  $F_i(V_{\perp})$ . Note the presence of the cold core ions and the hot ions appearing as a halo in  $F_i(V_{\parallel})$  and a beam in  $F_i(V_{\perp})$ .

**Figure 15.** Same as Figure 14, but for electrons. (a)  $F_e(V_{\parallel})$ . (b)  $F_e(V_{\perp})$ . Note that the electrons trapped with the ions have a flat top distribution in  $F_e(V_{\parallel})$  and a beam in  $F_e(V_{\perp})$ .

**Figure 16.** Comparison of the flux tube plasma contents from Run-2 of Paper 1 and Run-A and Run-B of this paper. Note that Curve 1 from Run-2 is vertically translated by adding the number of injected hot ions to its plasma content. This easily brings out the additional filling with the cold plasma caused by the processes driven by the hot plasma. After the hot plasma is injected at  $\bar{t} = 2000$  in run-B, the plasma content shown by Curve 3 closely follows Curve 1, and both remain below Curve 2.

**Figure 17.** Comparison of the density distributions from Run-2 in Paper 1 and Run-A with the injection of the hot plasmas at  $\bar{t} = 0$ . The densities shown are for  $\bar{t} = 3600$ .

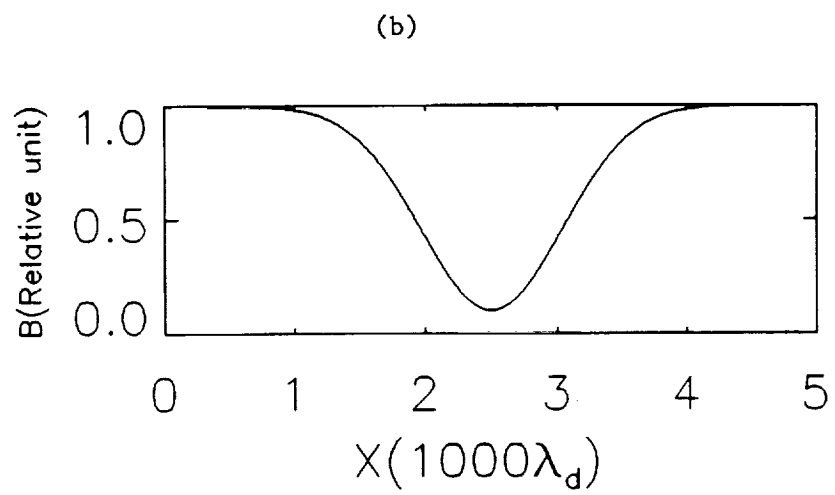
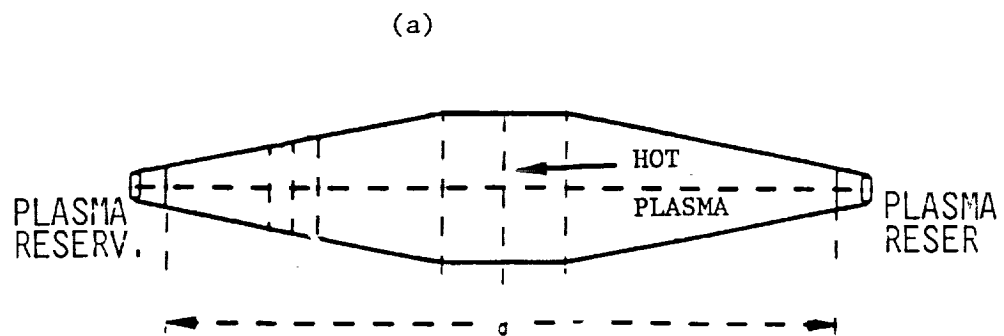


Fig. 1

Ion Parallel Velocity ( $V_{i\parallel}/V_{te}$ )

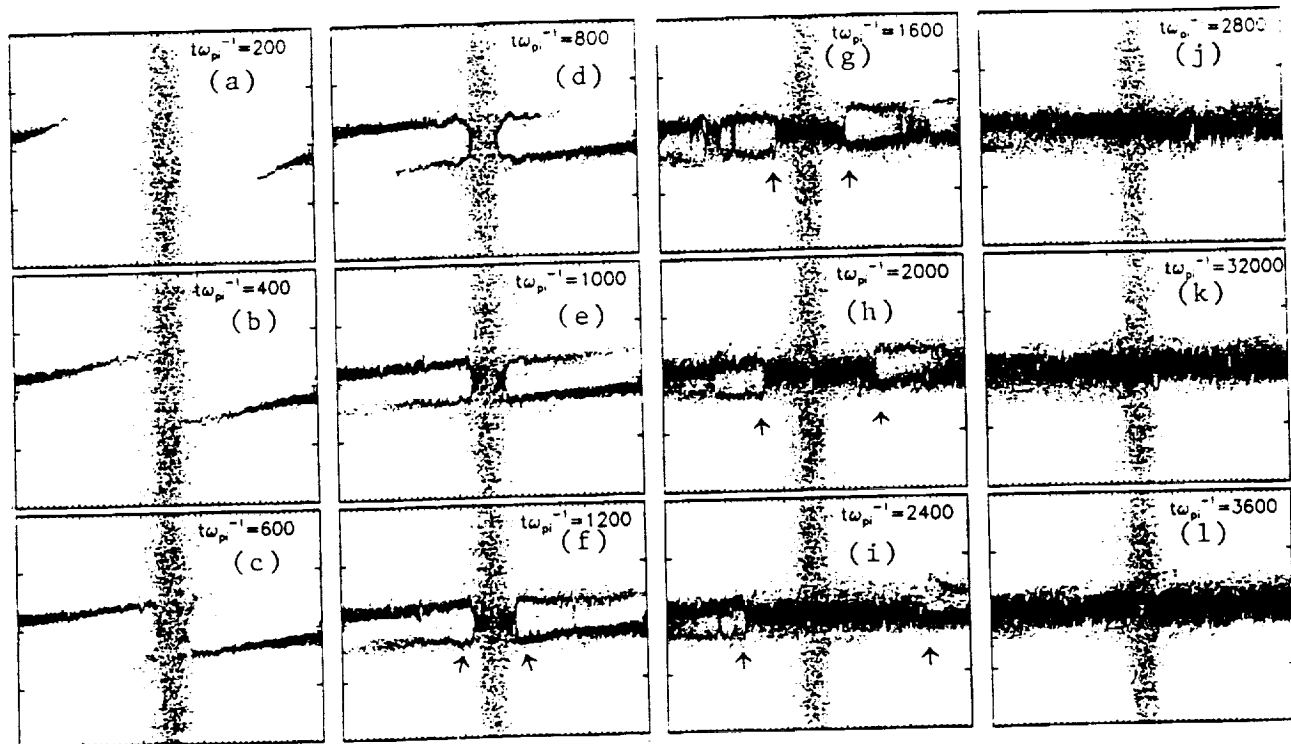


Fig. 2

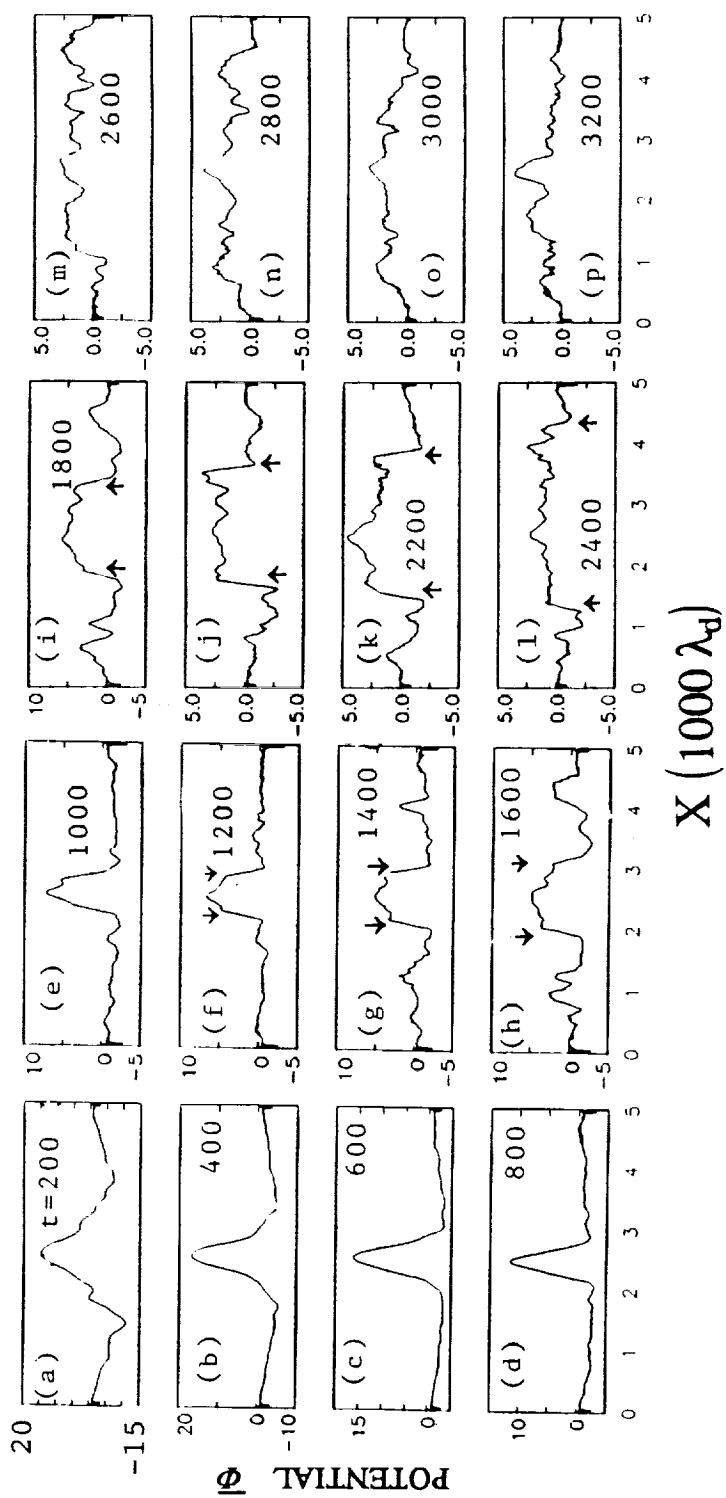


Fig. 3

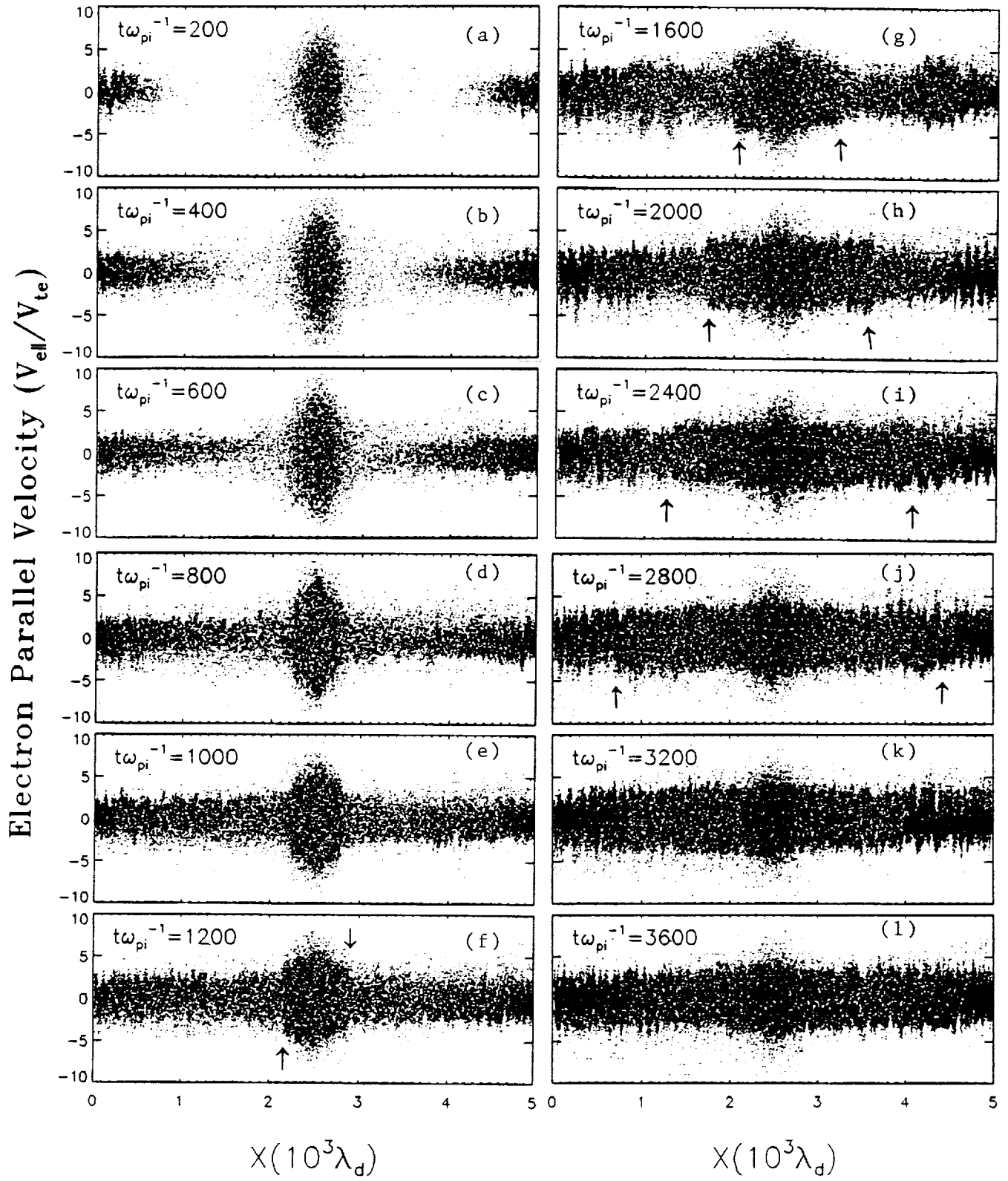


Fig. 4

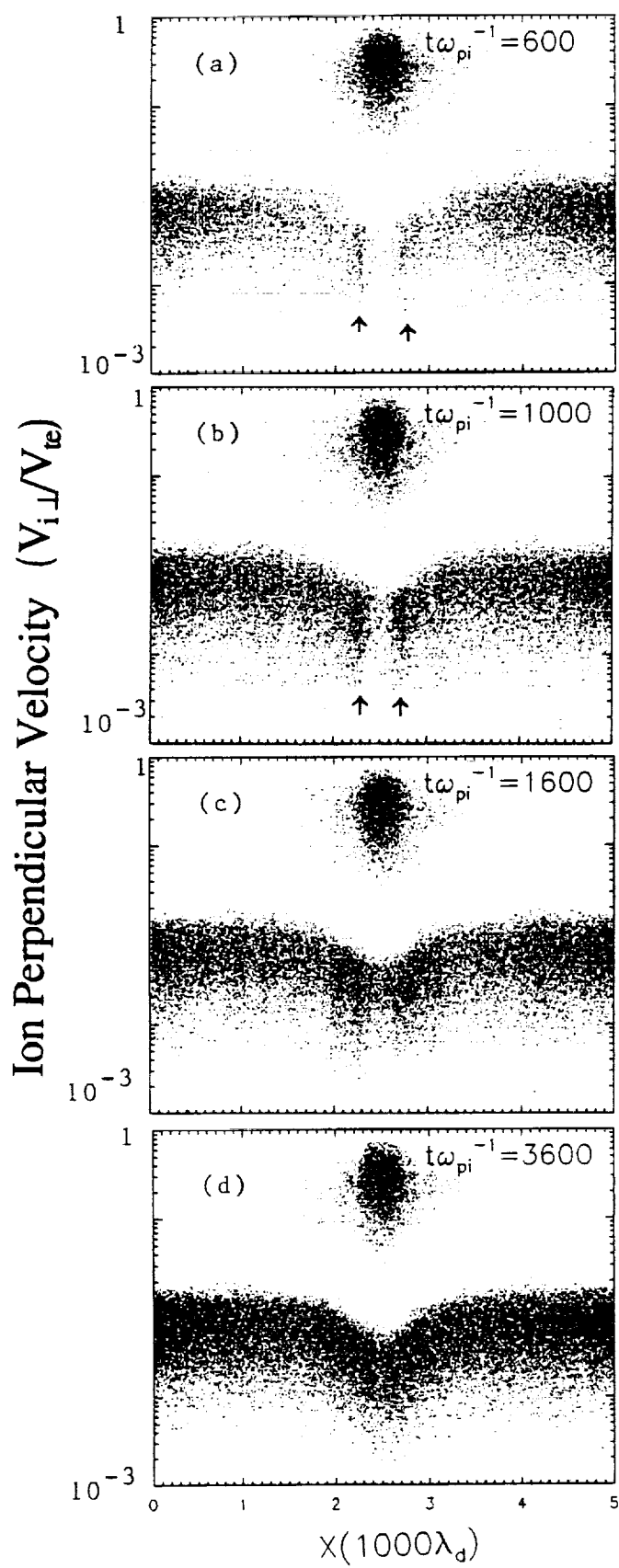


Fig. 5



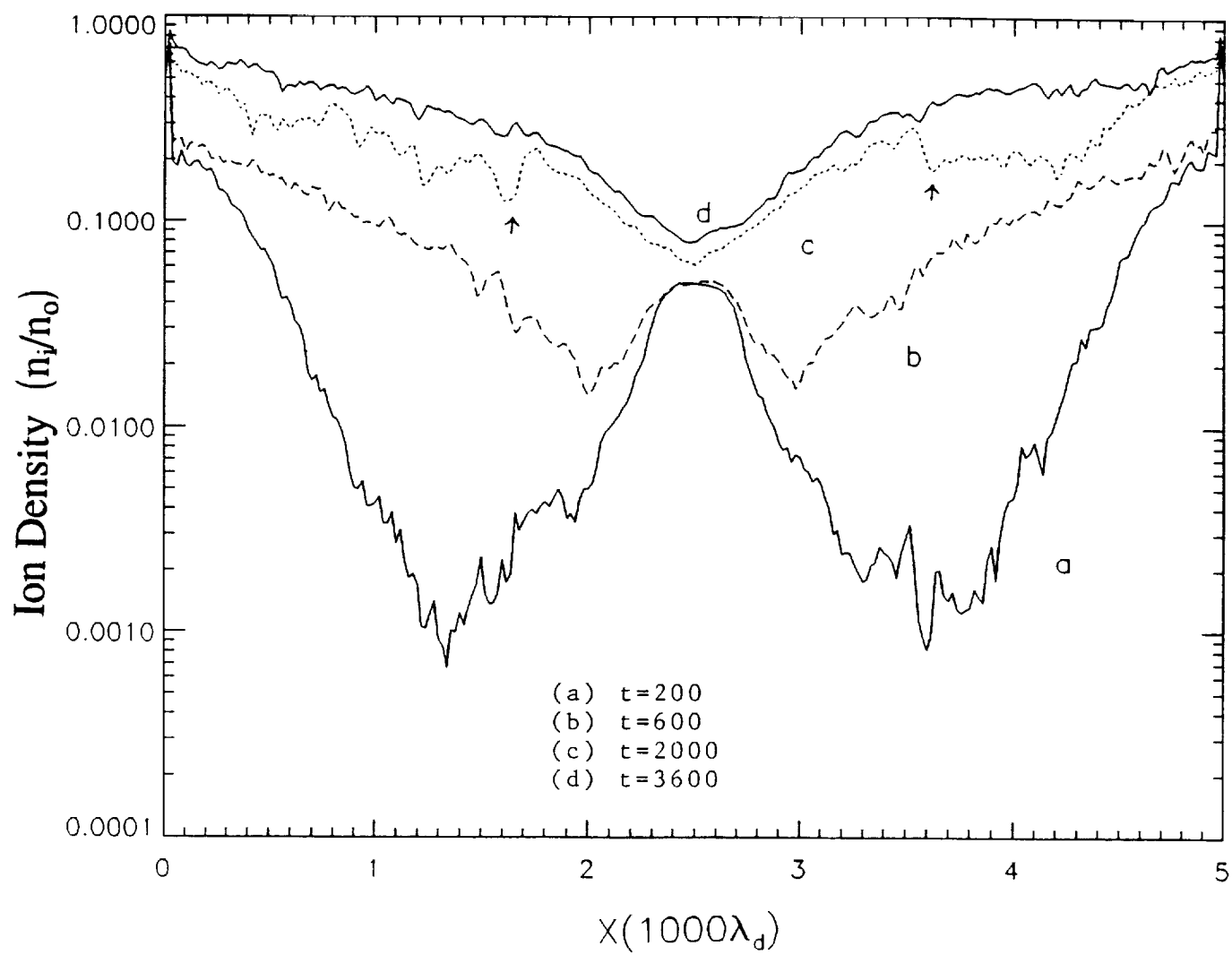


Fig. 6

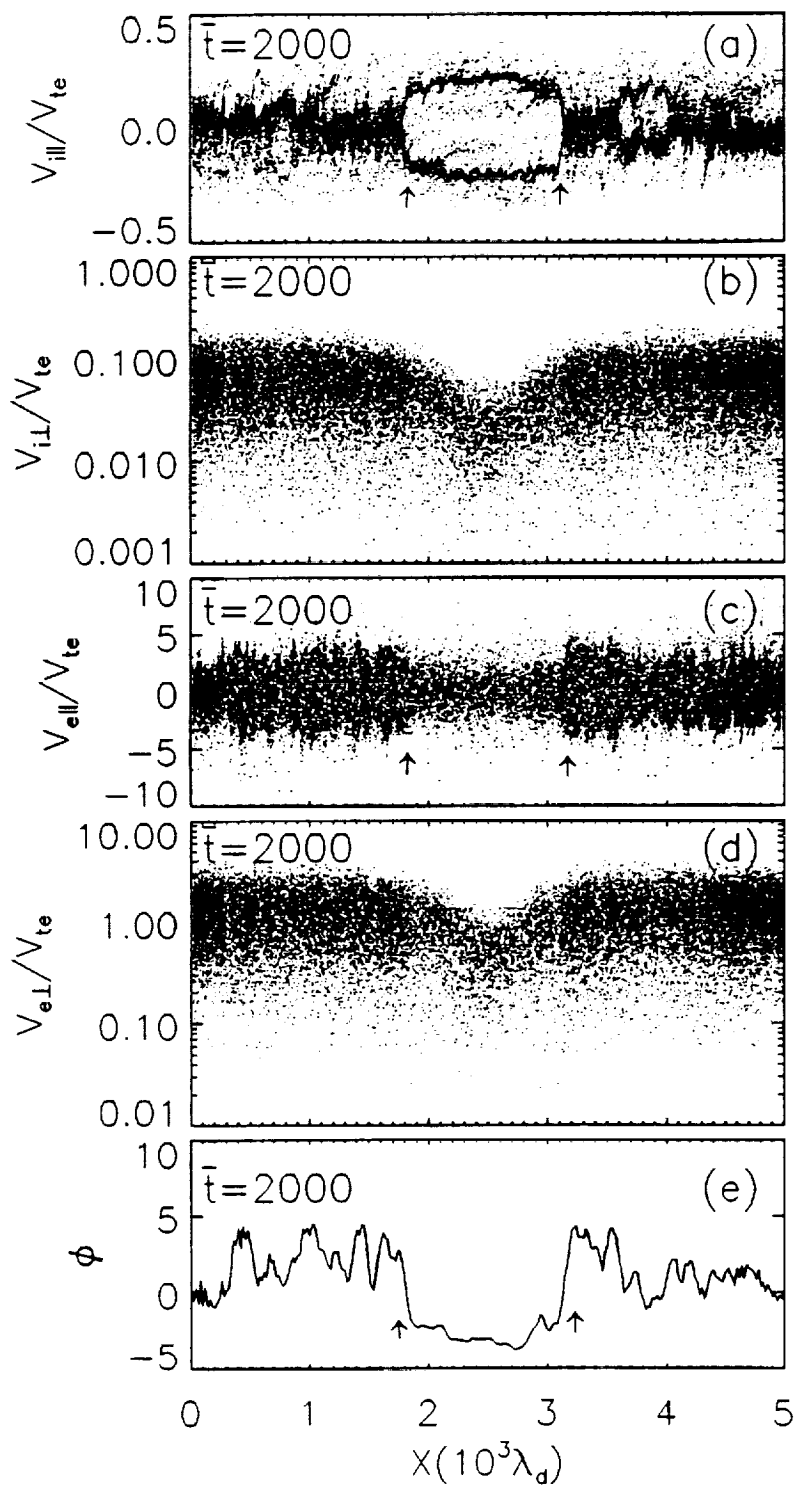


Fig. 7

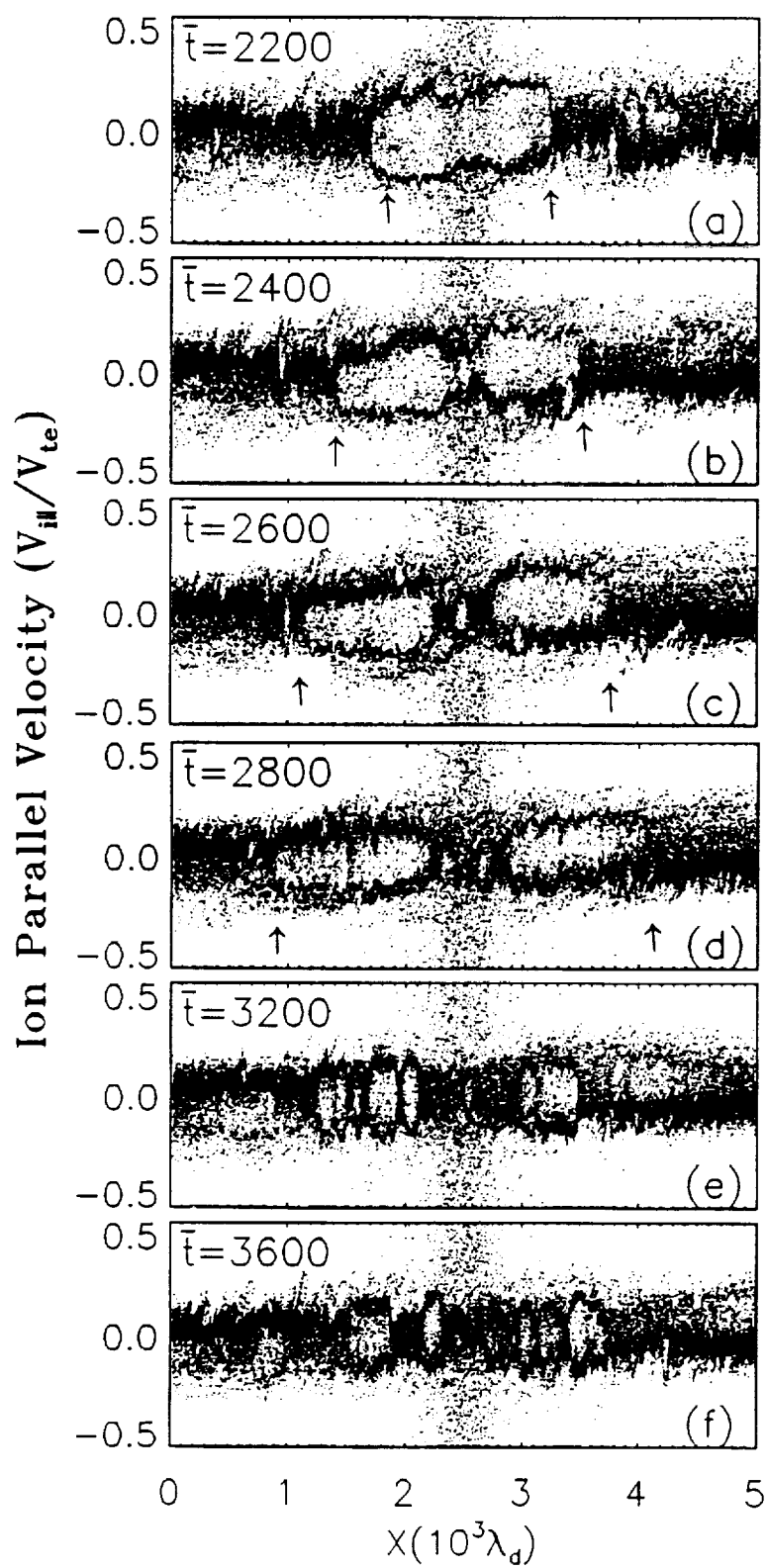


Fig. 8

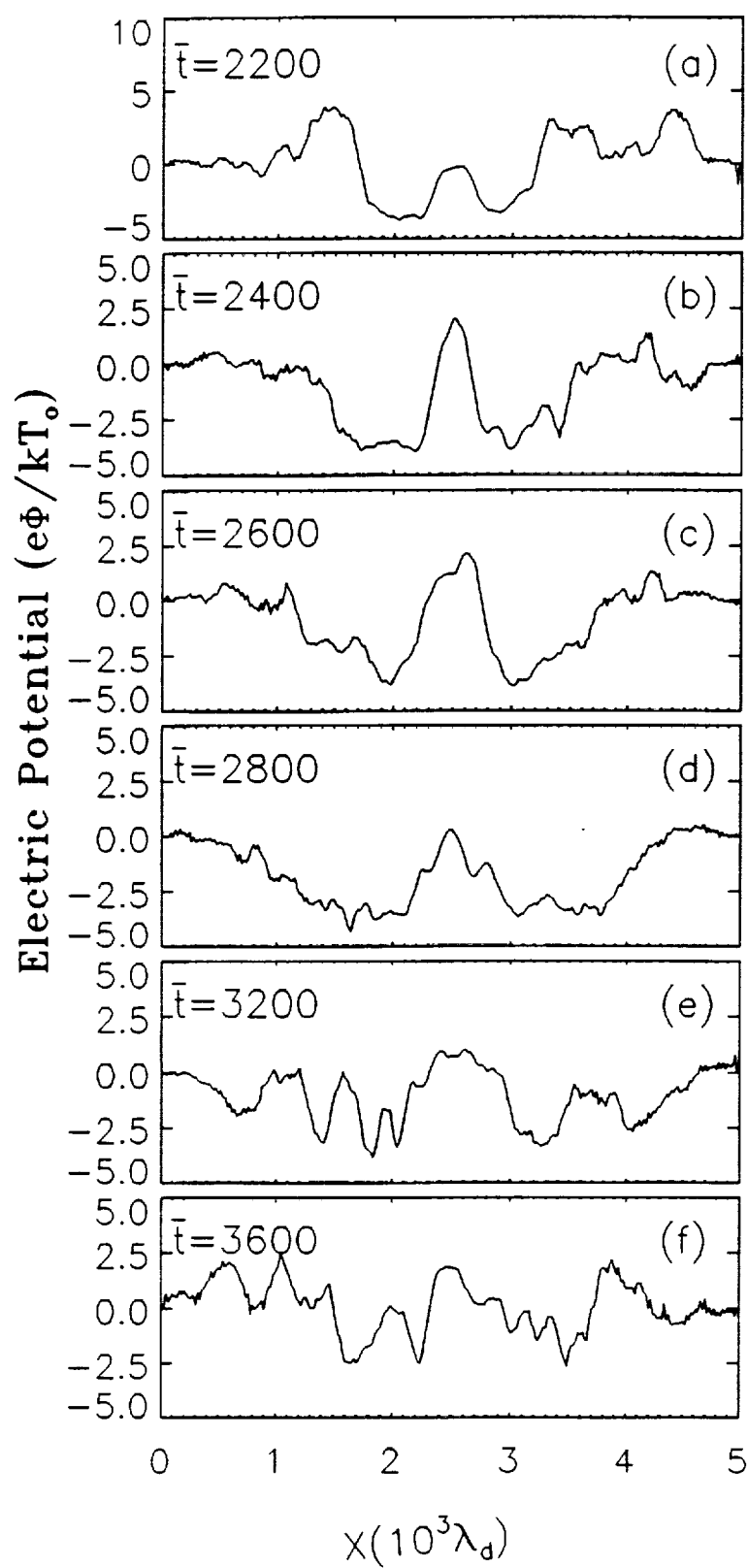


Fig. 9

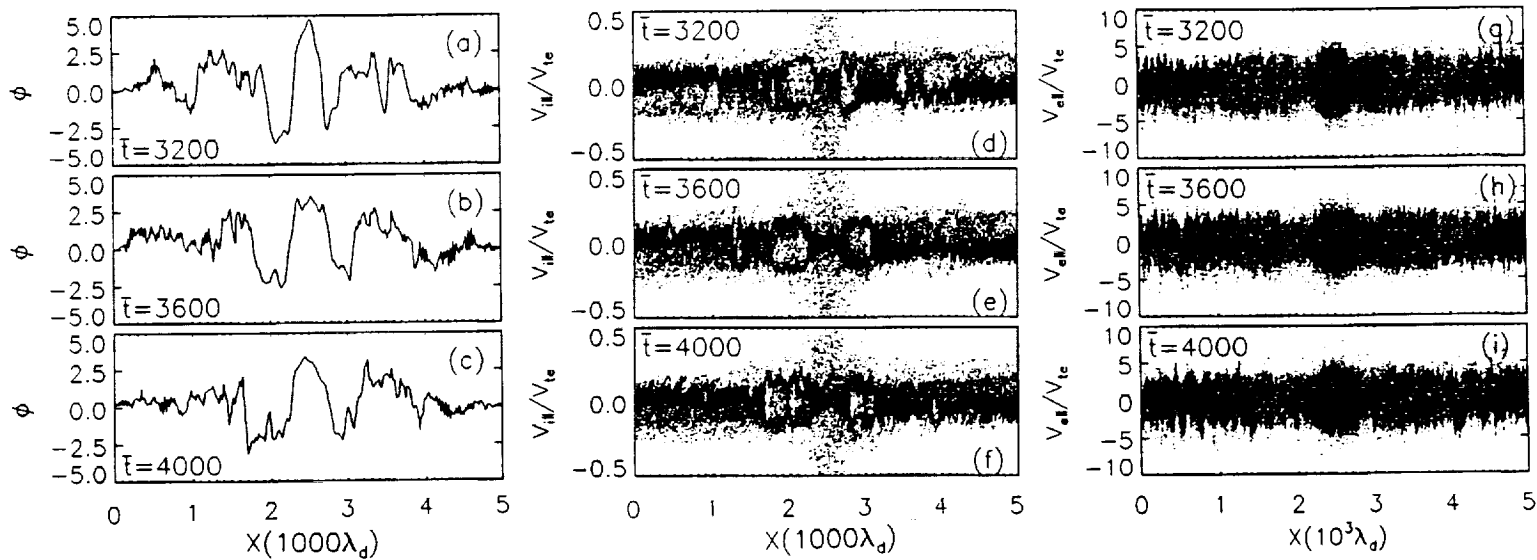


Fig. 10

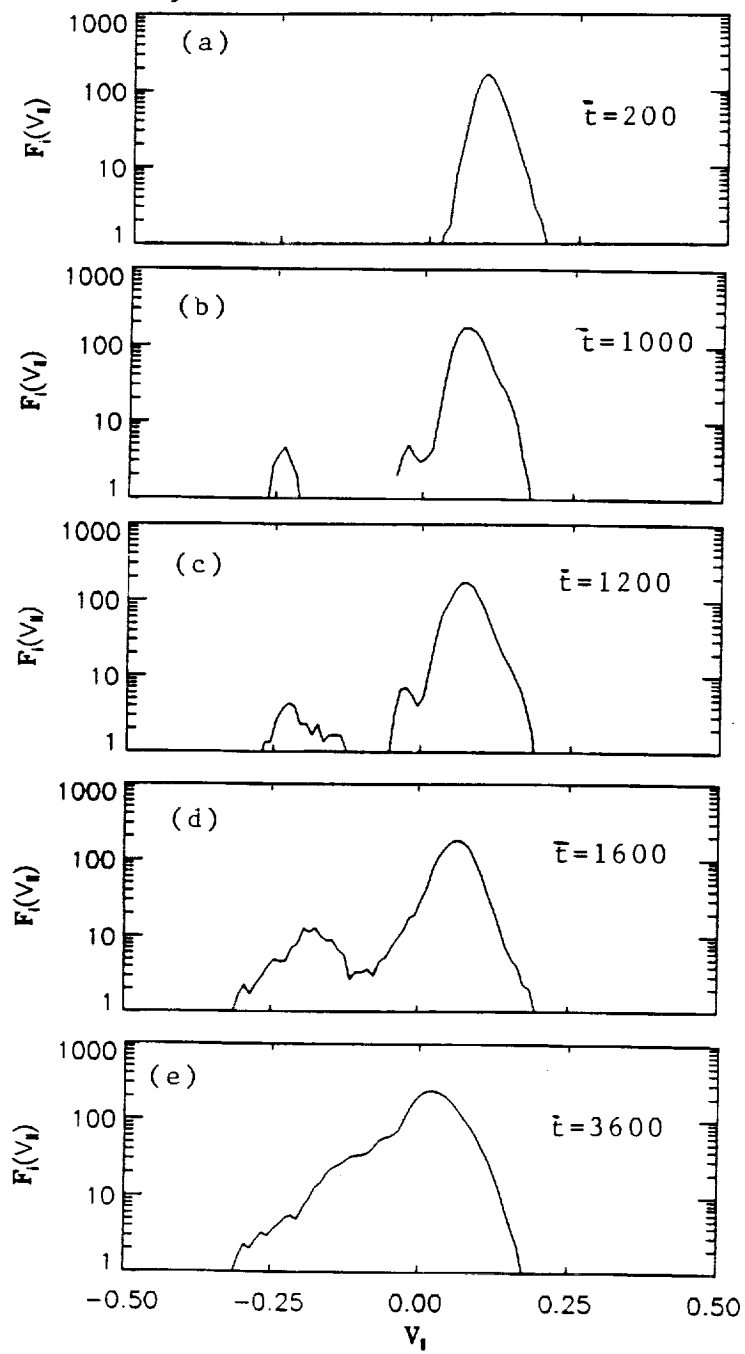


Fig. 11

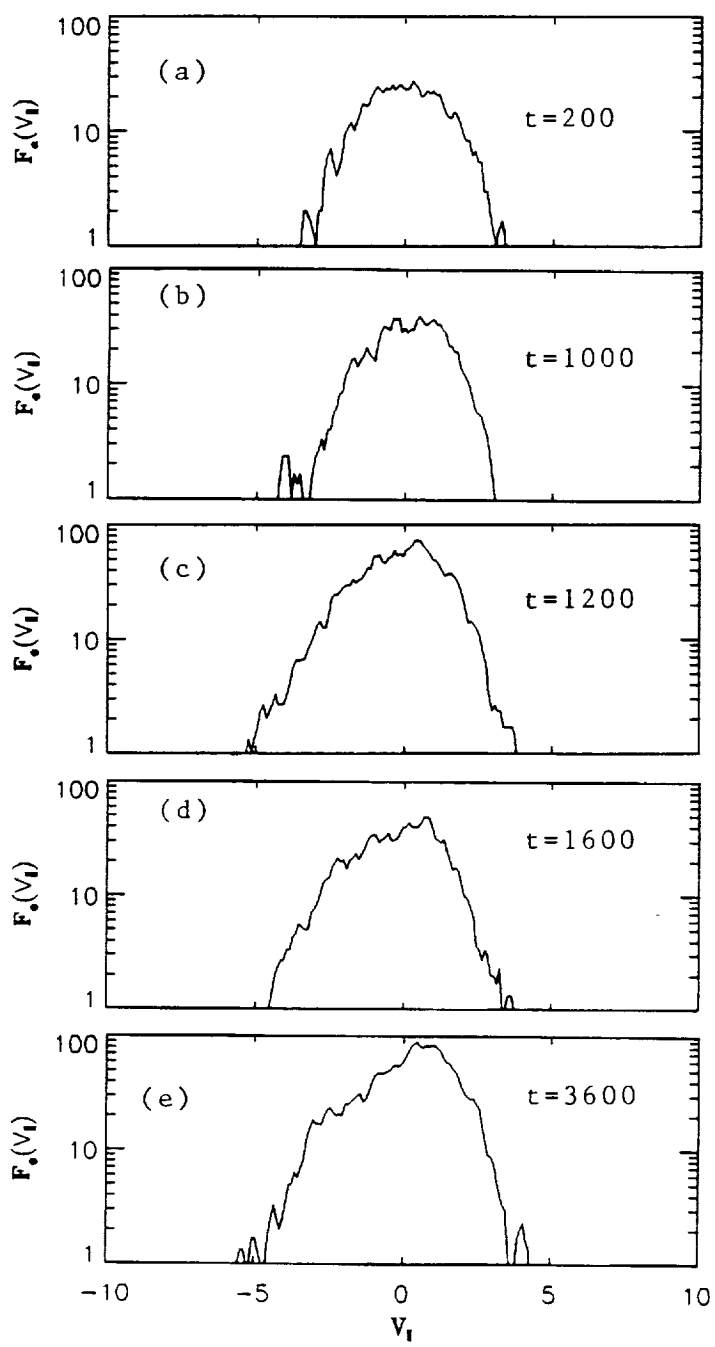


Fig. 12

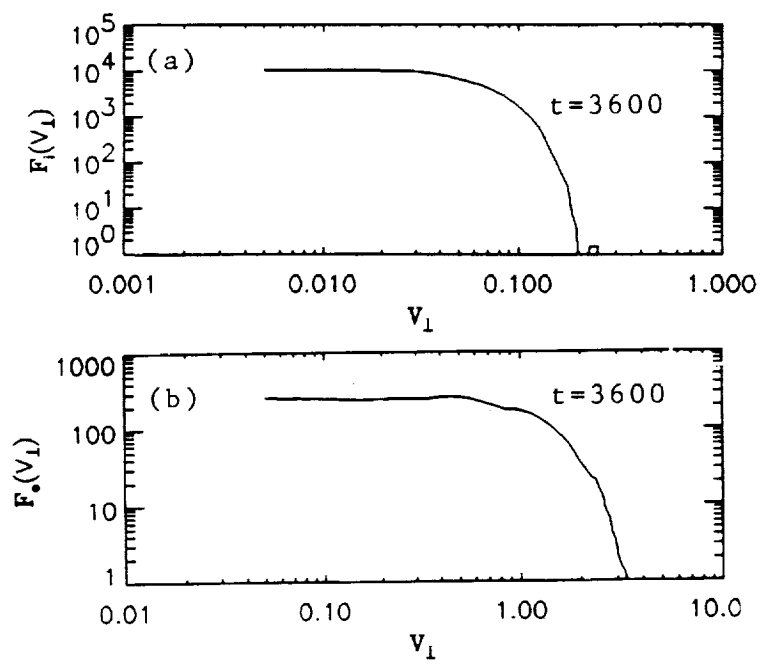


Fig. 13



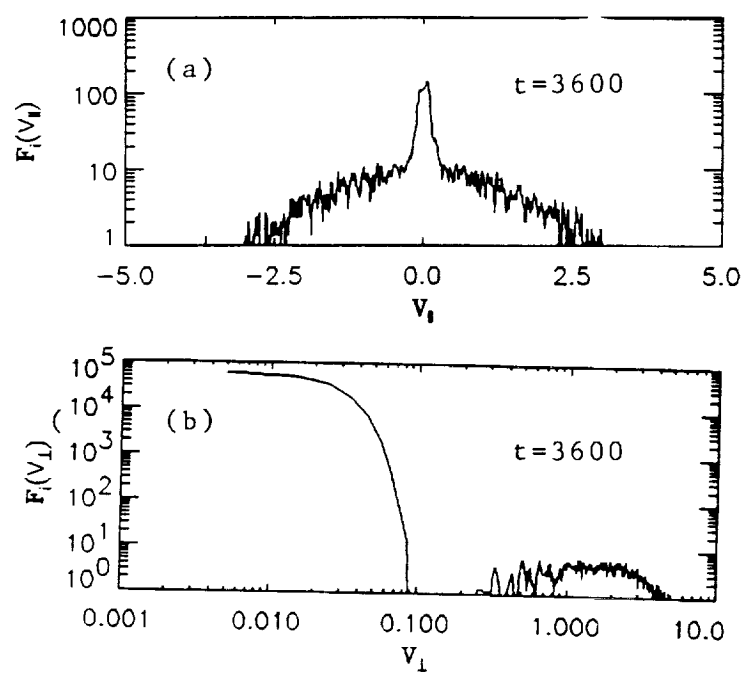


Fig. 14

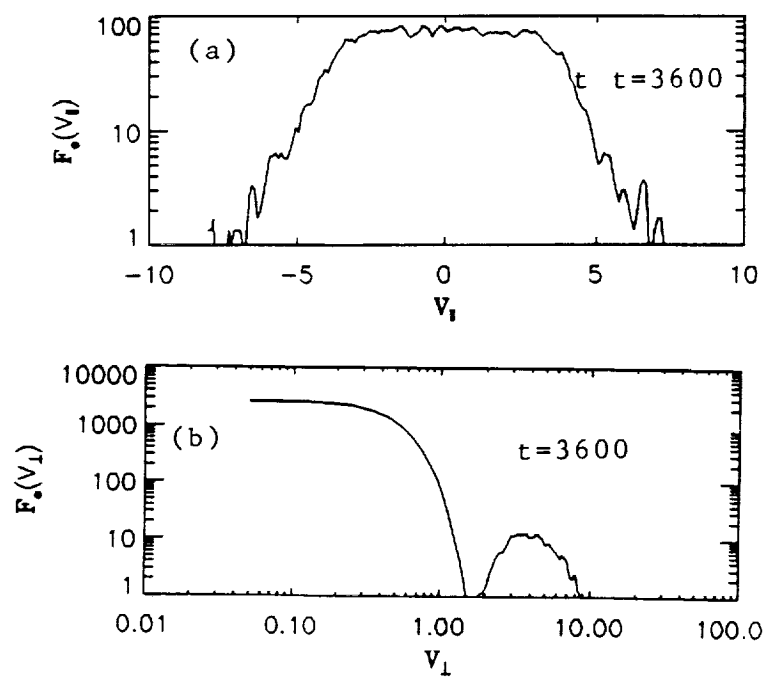


Fig. 15

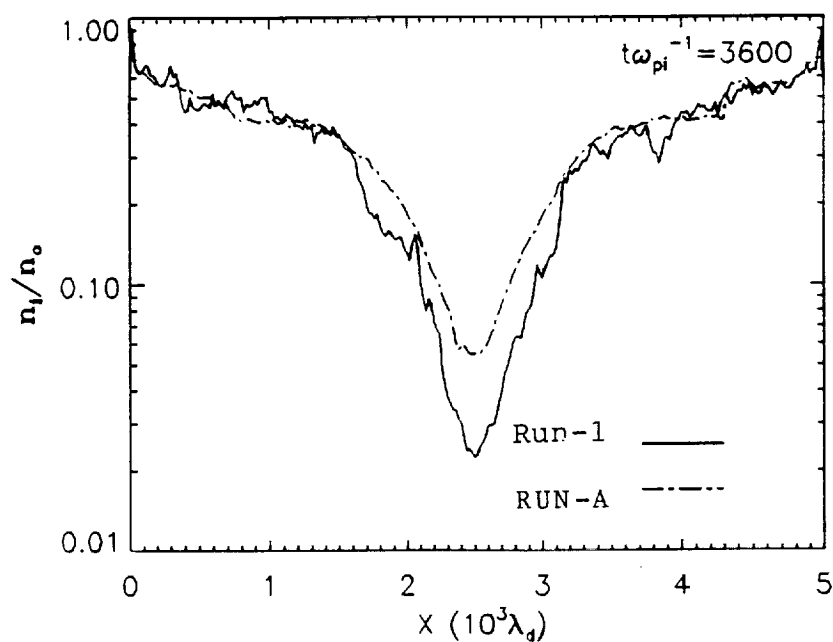


Fig. 17

PRECEDING PAGE BLANK NOT FILMED

End date July 29, 1994.

